Fakultät für Medizin
Technische Universität München

Rapid Optoacoustic Imaging for
Neurology, Cardiology and Vascular Biology

Johannes Jörg Rebling

Vollständiger Abdruck der von der Fakultät für Medizin der Technischen Universität München

zur Erlangung des akademischen Grades eines

Doktors der Naturwissenschaften (Dr. rer. nat.)

genehmigten Dissertation.

Vorsitzender:	Prof. Dr. Lars Maegdefessel
Prüfer der Dissertation:	1. Prof. Dr. Daniel Razansky
	2. Prof. Dr. Bjoern Menze

Die Dissertation wurde am 04.02.2019 bei der Technischen Universität München eingereicht
und durch die Fakultät für Medizin am 07.10.2019 angenommen.

Abstract

Optoacoustic imaging offers minimally invasive, fast, and volumetric visualization of cells, organs and organisms on various spatio-temporal scales based on the acoustic detection of light-induced ultrasound waves. The combination of unharmful optical excitation, endogenous optical contrast, and ultrasound depth penetration enables imaging of morphology, function and pathology in both pre-clinical and clinical settings. Numerous experimental and pre-clinical imaging systems have been developed and optoacoustic imaging systems are starting to be used in university clinics throughout the world. While optoacoustics has become a well-established and well-accepted imaging modality over the last decade, there are still numerous technical challenges which hinder the optimal utilization of this powerful imaging approach. The aim of this work is to present three distinct attempts at overcoming these challenges for both optoacoustic tomography and microscopy.

High resolution optoacoustic tomography requires sensor arrays with a large number of highly sensitive, high-frequency and high-bandwidth detector elements. Manufacturing ultrasound arrays that meet these requirements is very challenging and costly, hindering widespread application of optoacoustic tomography. In this work, we investigate the application of capacitive micromachined ultrasonic transducers (cMUTs) as an alternative to conventional piezoelectric sensor arrays for use in optoacoustic tomography. While the piezoelectric sensor showcased a superior sensitivity at normal incidence, the cMUT maintained reasonable sensitivity levels and broadband response at over a much wider range of incidence angles, resulting in a reduction of image artifact and thus superior optoacoustic imaging performance.

The second attempt at overcoming a challenge faced by optoacoustic imaging was the design, manufacturing and characterization of an ablation catheter prototype for simultaneous optoacoustic imaging and radiofrequency ablation. Catheter ablation is commonly used to eliminate dysfunctional heart tissue, but clinical outcomes rely heavily on the expertise of the surgeon due to the lack of real-time monitoring approaches. In this thesis we present an integrated catheter based on copper-coated multimode light-guides capable of delivering both ablation current and near-infrared pulsed-laser illumination to the target tissue. The generated optoacoustic signals were used to visualize the ablation lesion formation in heart tissue in 3D. Our catheter enables the monitoring of ablation lesions with high spatiotemporal resolution while the overall therapy-monitoring approach remains compatible with commercially available catheter designs.

The third attempt to overcome current challenges in optoacoustic imaging is the development of a novel, hybrid ultrasound and optoacoustic microscopy system. Research on the physiological structure of the brain as well as the investigation of neurological disorders depends on the accurate and volumetric representation of the whole brain. Optoacoustic microscopy has shown great potential to fulfill these requirements for small model animals such as mice, providing real-time, high-resolution volumetric images of the brain vascula-

ture, but existing solutions lack the required field-of-view to visualize the large and intricate vascular networks spanning the murine brain and skull. This work presents a microscopy system capable of rapid visualization of large-scale cerebral vascular networks through the intact skull. The system creates volumetric images of the morphology and oxygenation status of the cerebral vasculature with single capillary resolution and a field of view exceeding 6x8 mm^2, thus covering the entire cortical vasculature in mice. Complementary pulse-echo ultrasound recordings furthermore visualize the morphology of the skull and enable precise localization of the vascular network within and below the bone. The flexible hybrid design in combination with fast high-resolution imaging in 3D holds promise for generating better insights into the architecture and function of the neurovascular system.

Zusammenfassung

Optoakustische Bildgebung, basierend auf der der akustischen Erfassung lichtinduzierter Ultraschallwellen, ermöglicht die minimal-invasive, schnelle und räumliche Darstellung von Zellen, Organen und Organismen. Die Kombination aus unschädlicher optischer Anregung, optischem Kontrast und der hohen Ultraschalleindringtiefe ermöglicht die Visualisierung von Strukturen, Funktionen und Krankheiten sowohl im präklinischen als auch im klinischen Bereich. Zahlreiche experimentelle und präklinische Bildgebungssysteme wurden bereits entwickelt, und optoakustische Bildgebungssysteme werden in Universitätskliniken auf der ganzen Welt eingesetzt. Während sich die Optoakustik im letzten Jahrzehnt zu einer etablierten und akzeptierten Bildgebungsmodalität entwickelt hat, gibt es immer noch zahlreiche technische Herausforderungen, die die optimale Nutzung dieses leistungsstarken Bildgebungsansatzes behindern. Ziel dieser Arbeit ist es, drei dieser Probleme explizite aufzuzeigen und Lösungen zu präsentieren um diese Herausforderungen sowohl für die optoakustische Tomographie als auch für die Mikroskopie zu überwinden.

Die hochauflösende optoakustische Tomographie erfordert Ultraschallsensoren mit einer großen Anzahl hochempfindlicher Detektorelemente mit hoher Frequenz und hoher Bandbreite. Die Herstellung von Ultraschall-Arrays die diese Anforderungen erfüllen ist sehr anspruchsvoll und kostenintensiv und behindert eine breitere Anwendung der optoakustischen Tomographie in Kliniken. In dieser Arbeit wird die Anwendung sogenannter Capacitive Micromachined Ultrasonic Transducers (cMUTs) als Alternative zu herkömmlichen piezoelektrischen Sensorarrays für den Einsatz in der optoakustischen Tomographie untersucht. Unsere Untersuchungen zeigten, dass ein herkömmlicher piezoelektrische Sensor zwar eine bessere absolute Empfindlichkeit zeigte, der untersuchte cMUT sensor jedoch über einen viel breiteren Bereich von Einfallswinkeln eine gute Empfindlichkeit zeigte. Dies führt zu einer Verringerung von Artefakten bei der Bildgebung und somit zu einer überlegenen optoakustischen Abbildungsleistung des cMUT Sensorarrays.

Der zweite Versuch, eine Herausforderung der optoakustischen Bildgebung zu überwinden, war das Design, die Herstellung und die Charakterisierung eines Ablationskatheterprototyps für die simultane optoakustische Bildgebung und die Hochfrequenzablation. Diese Hochfrequenzablation wird im Allgemeinen verwendet, um dysfunktionales Herzgewebe zu entfernen. Die klinischen Ergebnisse hängen jedoch stark vom Fachwissen des Chirurgen ab, da keine Echtzeitüberwachungsansätze vorhanden sind. In dieser Arbeit stellen wir einen integrierten Katheter vor, der auf kupferbeschichteten Multimode-Lichtleitern basiert und in der Lage ist, sowohl Ablationsstrom- als auch Infrarot-Impulslaserbeleuchtung an das Zielgewebe zu liefern. Die erzeugten optoakustischen Signale wurden verwendet, um die Bildung der Ablationsläsion im Herzgewebe räumlich zu visualisieren. Unser Katheter ermöglicht die Überwachung von Ablationsläsionen mit hoher räumlicher und zeitlicher Auflösung, während der Ansatz der Therapieüberwachung insgesamt mit kommerziell erhältlichen Katheterkonstruktionen vereinbar bleibt.

Der dritte Versuch, die aktuellen Herausforderungen in der optoakustischen Bildgebung zu überwinden, ist die Entwicklung eines neuartigen hybriden Ultraschall- und Optoakustischen Mikroskopiesystems. Die Erforschung der physiologischen Strukturen im Hirn sowie die Untersuchung neurologischer Störungen hängen von der genauen und räumlichen Darstellung des gesamten Gehirns ab. Die optoakustische Mikroskopie hat großes Potenzial gezeigt, um diese Anforderungen für kleine Modelltiere wie Mäuse zu erfüllen. Den bestehenden Lösungen fehlt jedoch das erforderliche Sichtfeld, um das weit gefächerte und komplizierte Gefäßnetzwerke in Gehirn Schädel zu visualisieren. In dieser Arbeit wird ein Mikroskopiesystem vorgestellt, das in der Lage ist, großflächige zerebrale Gefäßnetzwerke durch den intakten Schädel schnell sichtbar zu machen. Das System erstellt räumliche Bilder der Struktur und des Sauerstoffgehalts der Hirngefäße mit kapillarer Auflösung und einem Sichtfeld von mehr als 6x8 mm^2. Damit wird das gesamte kortikale Gefäßsystem in Mäusen abgedeckt. Komplementäre Puls-Echo-Ultraschallaufnahmen visualisieren außerdem die Struktur des Schädels und ermöglichen eine präzise Lokalisierung des Gefäßnetzes innerhalb und unterhalb des Knochens. Das flexible design in Kombination mit der schnellen, hochauflösenden und räumlichen Abbildung ermöglicht bessere Einblicke in die Structur und Funktion des neurovaskulären Systems.

Acknowledgments

Publication Record

This publication based dissertation is based on the following, first-author publications which are reproduced in Chapters 2, 3, and 4 respectively († indicates shared author contribution):

1) **Johannes Rebling**, Omri Warshavski, Cyril Meynier, and Daniel Razansky. „Optoacoustic characterization of broadband directivity patterns of capacitive micromachined ultrasonic transducers". In: *Journal of biomedical optics* 22.4 (Nov. 2016), p. 041005.
   DOI: 10.1117/1.jbo.22.4.041005

2) **Johannes Rebling**†, Francisco Javier Oyaga Landa†, Xosé Luís Deán-Ben, Alexandre Douplik, and Daniel Razansky. „Integrated catheter for simultaneous radio frequency ablation and optoacoustic monitoring of lesion progression". In: *Optics letters* 43.8 (Apr. 2018), pp. 1886–1889.
   DOI: 10.1364/ol.43.001886

3) **Johannes Rebling**†, Héctor Estrada†, Sven Gottschalk, Gali Sela, Michael Zwack, Georg Wissmeyer, Vasilis Ntziachristos, and Daniel Razansky. „Dual-wavelength hybrid optoacoustic-ultrasound biomicroscopy for functional imaging of large-scale cerebral vascular networks". In: *Journal of biophotonics* (May 2018), e201800057.
   DOI: 10.1002/jbio.201800057

I furthermore contributed to the following peer-reviewed publications:

1) Sven Gottschalk, Héctor Estrada, Oleksiy Degtyaruk, **Johannes Rebling**, Olena Klymenko, Michael Rosemann, and Daniel Razansky. „Short and long-term phototoxicity in cells expressing genetic reporters under nanosecond laser exposure". In: *Biomaterials* 69 (Nov. 2015), pp. 38–44.
   DOI: 10.1016/j.biomaterials.2015.07.051

2) Moritz Kneipp, Jake Turner, Héctor Estrada, **Johannes Rebling**, Shy Shoham, and Daniel Razansky. „Effects of the murine skull in optoacoustic brain microscopy". In: *Journal of biophotonics* 9.1-2 (Apr. 2016), pp. 117–123.
   DOI: 10.1002/jbio.201400152

3) Héctor Estrada, **Johannes Rebling**, Jake Turner, and Daniel Razansky. „Broadband acoustic properties of a murine skull". In: *Physics in Medicine & Biology* 61.5 (Feb. 2016), p. 1932.
   DOI: 10.1088/0031-9155/61/5/1932

4) Héctor Estrada, **Johannes Rebling**, and Daniel Razansky. „Prediction and near-field observation of skull-guided acoustic waves". In: *Physics in Medicine & Biology* 62.12

(May 2017), p. 4728.
DOI: 10.1088/1361-6560/aa63e3

5) Héctor Estrada, Xiao Huang, **Johannes Rebling**, Michael Zwack, Sven Gottschalk, and Daniel Razansky. „Virtual craniotomy for high-resolution optoacoustic brain microscopy". In: *Scientific reports* 8.1 (Jan. 2018), p. 1459.
DOI: 10.1038/s41598-017-18857-y

6) Ben Mc Larney[†], **Johannes Rebling**[†], Zhenyue Chen, Xosé Luís Deán-Ben, Sven Gottschalk, and Daniel Razansky. „Uniform light delivery in volumetric optoacoustic tomography". In: *Journal of Biophotonics* (2018). in review

7) Héctor Estrada[†], **Johannes Rebling**[†], Wolfgang Sievert, Daniela Hladik, Urs Hofmann, Sven Gottschalk, Soile Tapio, Gabriele Multhoff, and Daniel Razansky. „Intravital optoacoustic microscopy reveals radiation-induced skull vasculopathy". In: (2018). submitted

8) Zhenyue Chen, Ben Mc Larney, **Johannes Rebling**, Xosé Luís Deán-Ben, Sven Gottschalk, and Daniel Razansky. „High speed wide-field structured illumination fluorescence microscopy". In: *Optica* (2018). submitted

9) Sven Gottschalk, Oleksiy Degtyaruk, Benedict Mc Larney, **Johannes Rebling**, Magdalena Anastasia Hutter, Xosé Luís Deán-Ben, Shy Shoham, and Daniel Razansky. „Rapid Volumetric Mapping of Neural Dynamics Across the Mouse Brain by Optoacoustic Calcium Imaging". In: *Nature Biomedical Engineering* (2018). in review

While peer-reviewed publications are an important measure of academic accomplishment, it is equally important to present and discuss ones work with the scientific community. This is best achieved through attendance and presentations at scientific conferences:

1) Héctor Estrada, **Johannes Rebling**, Jake Turner, Moritz Kneipp, Shy Shoham, and Daniel Razansky. „Estimation of the skull insertion loss using an optoacoustic point source". (Conference Presentation and Proceedings Paper). In: *Photons Plus Ultrasound: Imaging and Sensing 2016*. Ed. by Alexander A. Oraevsky and Lihong V. Wang. Vol. 9708. International Society for Optics and Photonics. SPIE, Mar. 2016, p. 97080M.
DOI: 10.1117/12.2211183

2) O. Warshavski, C. Meynier, N. Sénégond, P. Chatain, **Johannes Rebling**, Daniel Razansky, N. Felix, and A. Nguyen-Dinh. „Experimental evaluation of cMUT and PZT transducers in receive only mode for photoacoustic imaging". (Conference Presentation and Proceedings Paper). In: *Photons Plus Ultrasound: Imaging and Sensing 2016*. Ed. by Alexander A. Oraevsky and Lihong V. Wang. Vol. 9708. International Society for Optics and Photonics. SPIE, Mar. 2016, p. 970830.
DOI: 10.1117/12.2211799

3) Héctor Estrada, **Johannes Rebling**, and Daniel Razansky. „Observation of skull-guided acoustic waves in a water-immersed murine skull using optoacoustic excitation". (Conference Presentation and Proceedings Paper). In: *Optical Elastography and Tissue Biomechanics IV*. ed. by Kirill V. Larin and David D. Sampson. Vol. 10067. International Society for Optics and Photonics. SPIE, Feb. 2017, p. 1006710.
DOI: 10.1117/12.2252089

4) **Johannes Rebling**, Héctor Estrada, Michael Zwack, Gali Sela, Sven Gottschalk, and Daniel Razansky. „Hybrid ultrasound and dual-wavelength optoacoustic biomicroscopy for functional neuroimaging". (Conference Poster and Proceedings Paper). In: *Photons Plus Ultrasound: Imaging and Sensing 2017*. Ed. by Alexander A. Oraevsky and Lihong V. Wang. Vol. 10064. International Society for Optics and Photonics. SPIE, Mar. 2017, 100644T.
DOI: 10.1117/12.2250635

5) **Johannes Rebling**, Héctor Estrada, Sven Gottschalk, and Daniel Razansky. „Structural and functional small animal imaging using hybrid-focus optoacoustic biomicroscopy". (Conference Presentation and Proceedings Paper). In: *European Conference on Biomedical Optics*. Ed. by Vasilis Ntziachristos and Roger Zemp. Optical Society of America. SPIE, Aug. 2017, p. 1041505.
DOI: 10.1117/12.2284656

6) **Johannes Rebling**, Omri Warshavski, Cyril Meynier, and Daniel Razansky. „Broadband optoacoustic characterization of cMUT and PZT transducer directivity in receive mode". (Conference Poster and Proceedings Paper). In: *Medical Imaging 2017: Ultrasonic Imaging and Tomography*. Vol. 10139. International Society for Optics and Photonics. International Society for Optics and Photonics, Mar. 2017, 101391K.
DOI: 10.1117/12.2253850

7) **Johannes Rebling**, Francisco Javier Oyaga Landa, Xosé Luís Deán-Ben, and Daniel Razansky. „A new catheter design for combined radiofrequency ablation and optoacoustic treatment monitoring using copper-coated light-guides". In: *Optical Fibers and Sensors for Medical Diagnostics and Treatment Applications XVIII*. ed. by Israel Gannot. Vol. 10488. International Society for Optics and Photonics. SPIE, Feb. 2018, p. 1048805.
DOI: 10.1117/12.2287390

8) Sven Gottschalk, Oleksiy Degtyaruk, **Johannes Rebling**, Benedict McLarney, Xosé Luís Deán-Ben, Shy Shoham, and Daniel Razansky. „Volumetric optoacoustic mapping of fast neuronal activity in an isolated mouse brain model expressing genetically encoded calcium indicator". (Conference Presentation). In: *Neural Imaging and Sensing 2018*. Vol. 10481. International Society for Optics and Photonics. Mar. 2018, p. 104810L.
DOI: 10.1117/12.2289711

9) **Johannes Rebling**, Héctor Estrada, Wolfgang Sievert, Daniela Hladik, Soile Tapio, and Daniel Razansky. „In-vivo assessment of radiation-induced cerebrovascular damage in mice by hybrid optoacoustic-ultrasound bio-microscopy (Conference Presentation)". (Conference Presentation). In: *Photons Plus Ultrasound: Imaging and Sensing 2018*. Ed. by Alexander A. Oraevsky and Lihong V. Wang. Vol. 10494. International Society for Optics and Photonics. SPIE, Mar. 2018, p. 104940I. DOI: 10.1117/12.2290493

Preface

This chapter aims to provide the reader with a better understanding of the overall content of the presented thesis and how the different chapters are linked throughout the course of my work as a graduate student. Therefore, this chapter provides the context of the different publications on which this thesis is based and which cannot be provided within the much narrower scope of the manuscripts themselves.

The publications presented in this thesis share two characteristics, beside the obvious common denominator of all publications utilizing the optoacoustic (OA) effect. Firstly, they all aim at increasing the speed with which the targeted tissue or structures can be visualized. Secondly, they all required either the extensive development of OA imaging systems combining various fields such as mechanical, electrical, optical and software engineering (the exact work carried out for each publication is described in the sections prior to the manuscripts). The later chapters in this thesis are ordered based on the publication date of the peer-reviewed manuscript they represent. In this chapter however, my work will be presented in the order it was carried out to facilitate a better understanding of my PhD progress.

The following description of my engagements at the *"Multi-Scale Functional and Molecular Small Animal Imaging Group"* at the *"Institute of Biological and Medical Imaging"* (IBMI) tries to present a synopsis of the various projects I had the chance to participate in. Our multidisciplinary group consists of scientists and engineers of various fields and thus has ample opportunity to help develop solutions to the various challenges of biomedical imaging. Hence, as an optical engineer, I was involved in the development of a novel optical-resolution optoacoustic microscopy (OR-OAM) system, investigations into characterizing and applying a new ultrasound (US) transducer technology of optoacoustic tomography (OAT) as well as the design, manufacturing and proof-of-concept implementation of a combined OA imaging and ablation catheter.

A novel optoacoustic microscopy (OAM) design with hybrid optical and acoustic resolution was developed and evaluated at our institute [1]. While the hybrid-focus optoacoustic microscope (HFOAM) system already showed a very promising performance, there were several opportunities to fully utilize the systems potential. The investigation and implementation of those possible optimizations and their translation into novel applications was the main focus of my work as a PhD student. While familiarizing myself with the HFOAM system I participated in experimental work leading to two co-authored publications. On the one hand, our group established a cellular model in order to investigate the effect of nanosecond laser exposure on living cells [2]. For this, the HFOAM system was used in both OR-OAM and acoustic-resolution optoacoustic microscopy (AR-OAM) mode to study the extent and major exposure parameters responsible for both photobleaching and phototoxicity. On the other hand, we investigated the deteriorating effects of the murine skull on signal and image

quality in OAM [3]. We performed both phantom and ex-vivo animal studies to provide a quantitative description of the various acoustic and optical distortions introduced by murine skulls and showcase their effects on imaging performance of optoacoustic microscopy.

Once familiar with the system, I started work on extending HFOAMs functionality from simple morphological imaging of the vasculature to functional imaging. This was achieved with a dual-wavelength design by using additional optics, enabling rapid alternation between green (532 nm) and orange (578 nm) laser light during one measurement. The necessary changes to both hardware and software required for this work are described in Chapter 4 on page 85 together with the resulting manuscript describing the system hardware as well as the characterization and application of the system for functional imaging [4]. This work was also presented at two international conferences [5, 6].

The new HFOAM system, now capable of functional imaging holds great potential to provide better insights into cerebrovascular function and facilitate efficient studies into neurological and vascular abnormalities of the brain. However, all OA imaging systems targeting the brain have to overcome the skull as an acoustic barrier, as was shown with the above described study [3]. This initial study led to considerable effort in our group to overcome the skull as an acoustic barrier in OA microscopy. A number of studies, all lead by Dr. Héctor Estrada, further investigated the acoustic properties of the murine skull [7], showed the existence of skull-guided acoustic waves [8] and resulted in a novel method to partially overcome the skull as an acoustic barrier in OR-OAM [9]. As a contributing author in these studies, I assisted in the necessary experiments, data processing and manuscript preparation.

During my last year as a PhD student I initiated a joint study with the *"Institute of Radiation Biology"* (ISB) also located at the Helmholtz Zentrum München. After promising initial results we started an investigation into the effect of ionizing radiation on the murine skull and brain vasculature using the HFOAM system, which is currently in submission for publication [10].

The first three years of my work as a graduate student were funded through the OILTEBIA[1] Marie Curie ITN. Besides financial support, this program also encourages young researchers to gain international hands-on experience during industry secondments. The aim of my OILTEBIA project was to investigate the possible application of capacitive micromachined ultrasonic transducer (cMUT) arrays for OAT . During a secondment at Vermon (a French manufacturer of conventional composite piezoelectric US transducer arrays), I developed an US array characterization setup. This purely US based transmit-receive setup provided first results which were presented at an international conference [11], but the methodology was poorly suited to characterize the broadband, angular sensitivity which is a crucial characteristic for an US transducer used for OAT . Thus, I designed and implemented an improved characterization setup in our laboratory at the IBMI, based on an ultrawideband omnidirectional OA source. This simple yet powerful setup was used to characterize the frequency dependence of the angular response of a conventional lead zirconate titanate ultrasonic trans-

---

[1] *"Optical Imaging and Laser TEchniques for BIomedical Applications"* (OILTEBIA) is an initial training network (ITN) funded by the European Community's Seventh Framework Programme with grant agreement number 317526.

ducers (PZT-UTs) and a cMUTs with similar size and central frequency, both manufactured by Vermon. This project resulted in the peer-reviewed manuscript presented in Chapter 2 on page 44 and was also presented during the "SPIE Medical Imaging" conference in 2017 [12, 13].

The delivery of OA pulsed excitation illumination is a challenge for both OA microscopy and tomography. My efforts to provide customizable solutions for light delivery, with the initial goal of homogenous and efficient light-delivery for acoustic-resolution OA microscopy, resulted in significant in-house fiber manufacturing capabilities established in our group. Knowledge and experience in making simple multi-mode fibers bundles led to optimized illumination systems used in several of our tomographic imaging setups. These custom made light guides are an integral part of a publication in preparation where these fiber-bundles were used in combination with 3D printed mounts in order to provide homogenous illumination for quantitative OAT [14]. My fully customized solution was then applied for volumetric mapping of neural activity in the mouse brain, described in a manuscript currently under review [15]. The experience gained during the manufacturing of multi-mode light guides allowed us to also manufacture more advanced fiber bundles, which directly resulted in the publication of the manuscript presented in chapter 3. By using copper-coated multi-mode fibers (MMFs) light-guides which are capable of delivering both electrical current and pulsed-laser illumination we were able to present a proof-of-concept catheter design for simultaneous radiofrequency ablation and real-time optoacoustic monitoring [16].

The overall structure of the remaining thesis is as follows. The first, introductory chapter lays the foundation for the later presented manuscripts by providing a theoretical and practical introduction into both OAT and OR-OAM. Chapter 2 presents the manuscript on *"Optoacoustic characterization of broadband directivity patterns of capacitive micromachined ultrasonic transducers"* [12]. Chapter 3 then presents my work on an *"Integrated catheter for simultaneous radio frequency ablation and optoacoustic monitoring of lesion progression"* [16]. The final manuscript in Chapter 4 then presents a *"Dual-wavelength hybrid optoacoustic-ultrasound biomicroscopy for functional imaging of large-scale cerebral vascular networks"* [4]. The TU Munich regulations for the award of doctoral degrees require a one page summary of the author contribution prior to ech presented manuscript [17]. In order to easily and orderly identify the contributions I have made for each individual manuscript, the author contributions sections in chapters 2, 3 and 4 follow the Contributor Roles Taxonomy (CRediT) system as proposed in [18]. The CRediT system simplifies and standardizes the *"recognition of the different contributions of researchers, particularly in multi-authored works"*. The Appendix on page A finally presents the publishers letters of approval, as furthermore required by the TU Munich regulations.

References

[1] H. Estrada et al. „Real-time optoacoustic brain microscopy with hybrid optical and acoustic resolution". In: *Laser Physics Letters* 11.4 (2014), p. 45601.
     DOI: `Artn04560110.1088/1612-2011/11/4/045601`.

[2] Sven Gottschalk et al. „Short and long-term phototoxicity in cells expressing genetic reporters under nanosecond laser exposure". In: *Biomaterials* 69 (Nov. 2015), pp. 38–44.
     DOI: `10.1016/j.biomaterials.2015.07.051`.

[3] Moritz Kneipp et al. „Effects of the murine skull in optoacoustic brain microscopy". In: *Journal of biophotonics* 9.1-2 (Apr. 2016), pp. 117–123.
     DOI: `10.1002/jbio.201400152`.

[4] **Johannes Rebling**[†] et al. „Dual-wavelength hybrid optoacoustic-ultrasound biomicroscopy for functional imaging of large-scale cerebral vascular networks". In: *Journal of biophotonics* (May 2018), e201800057.
     DOI: `10.1002/jbio.201800057`.

[5] **Johannes Rebling** et al. „Hybrid ultrasound and dual-wavelength optoacoustic biomicroscopy for functional neuroimaging". (Conference Poster and Proceedings Paper). In: *Photons Plus Ultrasound: Imaging and Sensing 2017*. Ed. by Alexander A. Oraevsky and Lihong V. Wang. Vol. 10064. International Society for Optics and Photonics. SPIE, Mar. 2017, 100644T.
     DOI: `10.1117/12.2250635`.

[6] **Johannes Rebling** et al. „Structural and functional small animal imaging using hybrid-focus optoacoustic biomicroscopy". (Conference Presentation and Proceedings Paper). In: *European Conference on Biomedical Optics*. Ed. by Vasilis Ntziachristos and Roger Zemp. Optical Society of America. SPIE, Aug. 2017, p. 1041505.
     DOI: `10.1117/12.2284656`.

[7] Héctor Estrada et al. „Broadband acoustic properties of a murine skull". In: *Physics in Medicine & Biology* 61.5 (Feb. 2016), p. 1932.
     DOI: `10.1088/0031-9155/61/5/1932`.

[8] Héctor Estrada, **Johannes Rebling**, and Daniel Razansky. „Prediction and near-field observation of skull-guided acoustic waves". In: *Physics in Medicine & Biology* 62.12 (May 2017), p. 4728.
     DOI: `10.1088/1361-6560/aa63e3`.

[9] Héctor Estrada et al. „Virtual craniotomy for high-resolution optoacoustic brain microscopy". In: *Scientific reports* 8.1 (Jan. 2018), p. 1459.
     DOI: `10.1038/s41598-017-18857-y`.

[10] Héctor Estrada[†] et al. „Intravital optoacoustic microscopy reveals radiation-induced skull vasculopathy". In: (2018). submitted.

[11]   O. Warshavski et al. „Experimental evaluation of cMUT and PZT transducers in receive only mode for photoacoustic imaging". (Conference Presentation and Proceedings Paper). In: *Photons Plus Ultrasound: Imaging and Sensing 2016*. Ed. by Alexander A. Oraevsky and Lihong V. Wang. Vol. 9708. International Society for Optics and Photonics. SPIE, Mar. 2016, p. 970830.
DOI: 10.1117/12.2211799.

[12]   **Johannes Rebling** et al. „Optoacoustic characterization of broadband directivity patterns of capacitive micromachined ultrasonic transducers". In: *Journal of biomedical optics* 22.4 (Nov. 2016), p. 041005.
DOI: 10.1117/1.jbo.22.4.041005.

[13]   **Johannes Rebling** et al. „Broadband optoacoustic characterization of cMUT and PZT transducer directivity in receive mode". (Conference Poster and Proceedings Paper). In: *Medical Imaging 2017: Ultrasonic Imaging and Tomography*. Vol. 10139. International Society for Optics and Photonics. International Society for Optics and Photonics, Mar. 2017, 101391K.
DOI: 10.1117/12.2253850.

[14]   Ben Mc Larney† et al. „Uniform light delivery in volumetric optoacoustic tomography". In: *Journal of Biophotonics* (2018). in review.

[15]   Sven Gottschalk et al. „Rapid Volumetric Mapping of Neural Dynamics Across the Mouse Brain by Optoacoustic Calcium Imaging". In: *Nature Biomedical Engineering* (2018). in review.

[16]   **Johannes Rebling**† et al. „Integrated catheter for simultaneous radio frequency ablation and optoacoustic monitoring of lesion progression". In: *Optics letters* 43.8 (Apr. 2018), pp. 1886–1889.
DOI: 10.1364/ol.43.001886.

[17]   Technische Universität München. *TUM Promotionsordnung mit Wirkung vom 1. Januar 2014*. 2018. URL: https://bit.ly/2OIfqv6 (visited on 10/22/2018).

[18]   Liz Allen et al. „Publishing: Credit where credit is due". In: *Nature News* 508.7496 (2014), p. 312.

Contents

List of Figures

List of Tables

Acronyms

Symbols

3D three-dimensional

A

a anterior

ADC analog-to-digital converter

AFE analog front-end

AR-OAM acoustic-resolution optoacoustic microscopy

B

BS beam sampler

C

CLSM confocal laser scanning microscopy

cMUT capacitive micromachined ultrasonic transducer

CO collimating lens

CRediT Contributor Roles Taxonomy

CT x-ray computed tomography

D

DAQ data acquisition system

DC direct current

DM dichroic mirror

DOF depth of focus

DPSS diode-pumped solid-state

E

ENOB effective number of bits

F

fMRI functional magnetic resonance imaging

FOV field-of-view

FWHM full width at half maximum

G

GRIN gradient-index

H

HFOAM hybrid-focus optoacoustic microscope

I

IBMI *"Institute of Biological and Medical Imaging"*

ITN initial training network

IVUS intravascular ultrasound

L

LNA low noise amplifier

LSF line-spread function

LSFM light sheet fluorescence microscopy

M

MAP maximum amplitude projection

MEMS microelectromechanical systems

MFP mean free path

MIP maximum intensity projection

MMF multi-mode fiber

MPF multiphoton fluorescence microscopy

MRI magnetic resonance imaging

MTF modulation transfer function

N

NA numerical aperture

Nd:YAG neodymium-doped yttrium aluminum garnet

NDT non-destructive-testing

NEP noise equivalent pressure

O

OA optoacoustic

OAM optoacoustic microscopy

OAT optoacoustic tomography

OCT optical coherence tomography

OILTEBIA *"Optical Imaging and Laser TEchniques for BIomedical Applications"*

OPO optical parametric oscillator

OR-**OAM** optical-resolution optoacoustic microscopy

OSA Optical Society of America

P

p posterior

PBS polarizing beam splitter

PC Pockels cell

PCF photonic crystal fiber

PD photodiode

PET positron emission tomography

PRF pulse repetition frequency

PSF point-spread function

PVdF polyvinylidene fluoride

PZT lead zirconate titanate

PZT-UT lead zirconate titanate ultrasonic transducer

R

RF radiofrequency

RFCA radiofrequency catheter ablation

ROI region of interest

S

SMF single-mode fiber

SNR signal-to-noise ratio

SOS speed of sound

SPECT single-photon emission computed tomography

SRS stimulated Raman scattering

SSS superior sagittal sinus

T

TMFP transport mean free path

U

US ultrasound

1. Introduction

The goal of this introductory chapter is to provide a brief introduction to the aspects of optoacoustic (OA)[1] imaging which are most relevant for the presented thesis, namely optical-resolution optoacoustic microscopy (OR-OAM) and optoacoustic tomography (OAT). As this PhD thesis is presented as part of a doctorate in experimental medicine, this chapter will also focus primarily on the practical aspects of both OR-OAM and OAT. Many important topics relevant for OA imaging cannot be covered here and the interested reader is referred to the wealth of comprehensive reviews [1–10] and literature [11, 12] on the topic.

1.1. Fundamentals of Optoacoustic Imaging

This chapter provides a brief introduction into the surprisingly long history of OA imaging and provides the fundamental conceptual and theoretical basis underlying all OA-based imaging techniques.

1.1.1. History and Perspective of Optoacoustic Imaging

The OA effect, that will be described in more detail in section 1.1.2, has been known for over one hundred years. German engineer Werner Siemens was one of the many famous scientists who directly or indirectly investigated the OA effect, which ultimately lead to OA imaging as we know it today. In 1875 Siemens published a paper in *Nature* where he describes the interesting effect of light on the conductivity of crystalline Selenium [13, 14]. The inventor of the telephone, Alexander Graham Bell, first described the "Production and Reproduction

---

[1]The terms OA and photoacoustic are used interchangeably in the literature. The term OA will be used throughout this work.

of Sound by Light" in two publications[2] in fall 1880 [15, 16]:

> "We find that when a vibratory beam of light falls upon these substances they emit sounds, the pitch of which depends upon the frequency of the vibratory change in the light."

where the authors also present the first recorded application of the OA effect, the so-called *photophone*. The OA effect was also studied by John Tyndall, who still in 1880 showed that light can also create an acoustic signal in gas [17]. These experiments where confirmed by Bell and Wilhelm Conrad Röntgen in the following year when Bell also confirmed the OA effect in liquids [18, 19]. Still in the same year, Lord Rayleigh provided a simple theoretical explanation of the effect [20]:

> "We may conclude, I think, that there is at present no reason for discarding the obvious explanation that the sounds in question are due to the **bending of the plates under unequal heating**."

The OA effect[3] has since been used extensively for gas analysis in spectrophones [23]. While spectrophones were used for over a century, they offered only few advantages over conventional gas absorption spectroscopy until 1970. However, the advent of the laser in combination with more sensitive microphones brought the sensitivity and specificity of OA spectroscopy to a new level [24]. The possibility to study gases, liquids and solids *in situ* has made the OA effect a valuable spectroscopic tool and the field is still under active development [25].

For over a century, the OA effect was used almost exclusively for the spectroscopy of gases, until *Rosencwaig* [26] followed Bell's original approach and investigated the OA effect in solids rather than gases. In the same year, *Rosencwaig* also suggested the potential use of OA spectroscopy in biology [23] rather than material sciences. It took another decade, until 1981, for *Bowen* to suggest an imaging scheme that would eventually lead to OA imaging as we know it today. His approach was to use *"RF or microwave electromagnetic radiation, high*

---

[2]These two publications are a remarkable case of duplicate publication, as the manuscripts submitted to the *American Journal of Science* and to *Nature* are virtually identical.

[3]The term "optic-acoustic" effect was first used by *Veingerov* [21] in 1938 and was later used by *Delany* [22].

intensity ultrasonic radiation or therapeutic levels of ionizing radiation" to deposit energy in the tissue and to create a sound wave [27].

This more general approach, now called thermoacoustics [28–31], also yields interesting results, but *Bowen* did not realize the potential use of light as an excitation source. The general interest in OAs steadily increased in the following decade and laser-induced sound generation was studied to non-destructively evaluate materials [32]. The theoretical fundamentals of optoacoustic signals generated in fluids were also developed during that time. Based on the acoustic wave equation, *Diebold et al.* [32–34] were able to precisely describe the shape and amplitude of the generated sound waves as a function of both the shape of the absorbing body as well as the duration of the exciting laser pulse. This understanding of the relationship between generated sound waves and object geometry would later allow the development of inverse reconstruction algorithms. These algorithms make it possible to deduce the size and shape of the emitting body or tissue by measuring the sound wave it creates, which ultimately enabled OAT.

It was only due to the combination of theoretical understanding, technological advancements (i.e. high power laser sources, sensitive ultrasound (US) transducers, reconstruction algorithms and computing capabilities [5]) as well as an increasing need for small animal imaging [35] that it was possible to create the first "truly" OA imaging scheme in 1994. Both *Kruger et al.* [36] as well as *Oraevsky et al.* [37, 38] presented the first experimental implementation of OA imaging. After these first papers, the field developed very rapidly and a large number of different tomographic and microscopic imaging methods were developed in the years which followed [28, 39–43].

Research on the OA effect and in particular OA imaging has skyrocketed in recent years, as shown in Figure 1.1. The number of publications on OAs and OA imaging has steadily increased in the last decade with an overall growth of more than 300 % in the number of OA papers published[4]. OA imaging is now being translated into more and more commercial systems by both established industry leaders and a number of startup companies such as FUJIFILM VisualSonics, iThera Medical or Seno Medical.

---

[4]Data based on Elsevier's Scopus search for the terms photoacoustic and optoacoustic (link)
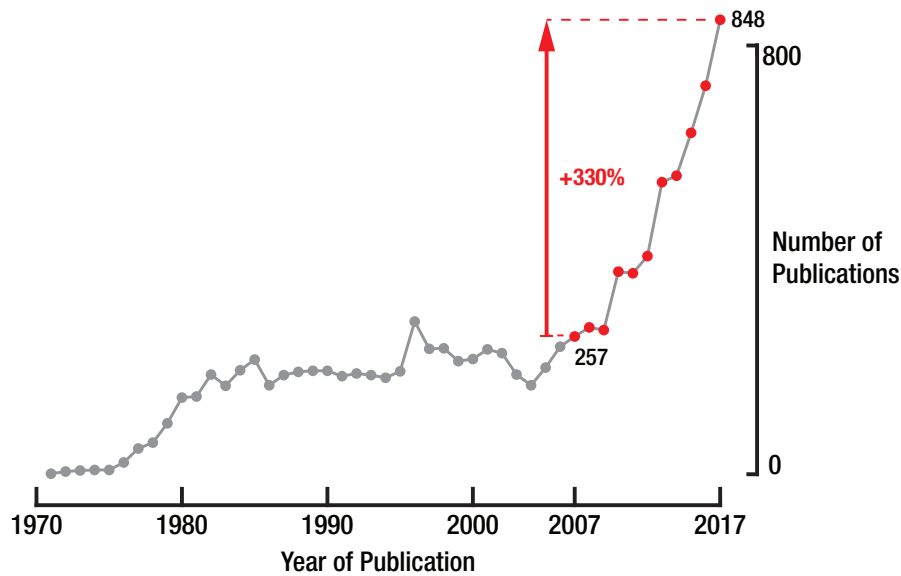
Figure 1.1.: The number of publications on optoacoustics and optoacoustic imaging has steadily increased in the last decade. Data based on Elsevier's Scopus search for the terms photoacoustic and optoacoustic (link).

1.1.2. The Optoacoustic Effect

Despite being known for more than a century, interest in applying the OA effect to the biomedical imaging field has tremendously increased in the last decades, as described in the previous chapter. Hence, OA imaging is still an emerging and quite novel imaging modality. The OA effect utilizes short-pulsed electromagnetic radiation[5] in order to excite broadband acoustic waves via photon absorption and thermoelastic expansion. The US waves are detected by an US transducer and are converted into an image similar to conventional US imaging. Figure 1.2 illustrates this three step process, consisting of optical excitaiton (Fig. 1.2a), US generation (Fig. 1.2b), and US sensing (Fig. 1.2c).

The combination of optical excitation along with US propagation and detection offers distinct advantages to all OA imaging modalities [9, 10]:

- Both endogenous and exogenous optical contrast enables functional and morphological imaging from the molecular to the whole body scale

---

[5]OA imaging typically relies on light in the visible and near-infrared range but other forms of electromagnetic radiation such as radiofrequency radiation in the kilo to gigahertz range can be utilized as well. [28–31]
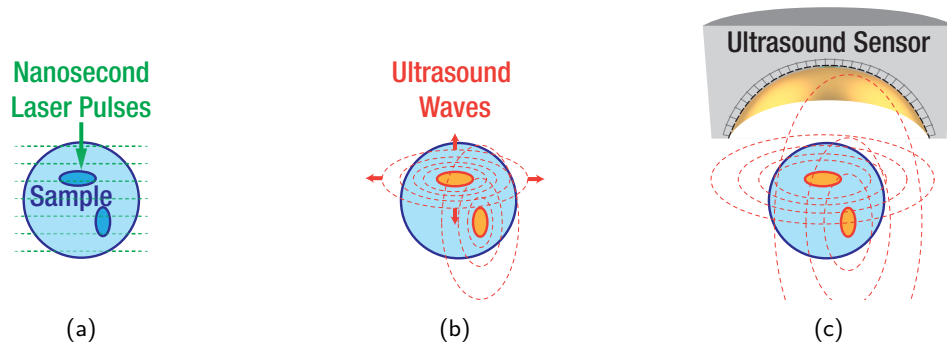
Figure 1.2.: The optoacoustic effect. a) Pulsed laser light illuminates an optically absorbing sample. b) The light is locally absorbed and generates broadband US waves. c) The US waves propagate through the tissue and are absorbed by an US transducer.

- Optical excitation using multiple wavelengths allows spectrally resolved volumetric images where the chemical composition of biological tissues can readily be identified

- Soft biological tissues such as muscle and most organs are almost transparent for propagating US waves, allowing orders of magnitude greater penetration in combination with scalable spatial resolution when compared to purely optical techniques.

- Most OA imaging approaches are compatible and complementary with existing imaging modalities.

- Optical excitation is safer and more cost effective than using ionizing radiation.

1.1.3. Optoacoustic Wave Equation

Section 1.1.2 provided a brief conceptual explanation of the OA effect, however, a more quantitative description is required in order to build and optimize real-world imaging system based on the OA effect and in order to reconstruct images from measured OA signals. This section therefore provides a short theoretical overview of the generation of OA waves while focusing on the resulting technical requirements and considerations regarding OA imaging systems. A more detailed theoretical derivation and description of the phenomenon can be found in the literature [11, 44].

Pressure waves generated by the absorption of short pulses of laser radiation can be

described based on the solution of the acoustic wave equation [33, 44]:

$$\left[\boldsymbol{\nabla}^2 - \frac{1}{v_s^2} \frac{\partial}{\partial t^2} \right] p = - \frac{\beta}{C_P} \frac{\partial H}{\partial t}, \tag{1.1.1}$$

with $\boldsymbol{\nabla}$ the gradient, v_s the speed of sound (SOS)[6], and p the resulting pressure field and with the source term on the right hand side with H the local energy deposited by the optical pulse, C_p the heat capacity and β the thermal expansion.

The wave equation (1.1.1) is valid only if both temporal *heat confinement* and *stress confinement* criteria are met [45]. These criteria need to be fulfilled by the excitation light source, and are hence of tremendous importance for practical implementations of OA systems.

Heat confinement requires that energy deposited by the laser pulse is not lost through heat diffusion. Using the heat diffusion equation, it is possible to approximate the heat diffusion length d for a given heating time τ to be [46]:

$$d = \sqrt{4\alpha\tau} \tag{1.1.2}$$

with the thermal diffusivity α. For absorbers of size d, the heat confinement requirements can be expressed as a pulse duration

$$\tau_h < \frac{d^2}{4\alpha}. \tag{1.1.3}$$

With the thermal diffusivity α of aproximately 1.5×10^{-7} mm^{2}s^{-1} for biological tissue [47] and absorbers with a size of approximately 10 micrometers or more, the heat confinement time τ_h is more than 100 microseconds.

Stress confinement requires the pressure relaxation during the laser pulse to be negligible as is the case if the duration of the laser pulse is shorter than the time required for the pressure wave to propagate out of the imaged structure [45]:

$$\tau_s < \frac{d}{c}. \tag{1.1.4}$$

---

[6]The speed of sound in both water and biological tissue is approximately 1500 ms^{-1}.

The SOS in tissue is close to that in water, approximately $1500\,\text{ms}^{-1}$. Absorbers with sizes smaller than 15 micrometers therefore require laser pulse durations shorter than 10 nanoseconds. Since temporal stress confinement requires nanosecond laser pulses compared to the millisecond pulses required by the heat confinement criteria, the latter can be neglected. The stress confinement criteria does however have a major impact on the design of any OA imaging system. Nanosecond short pulses with sufficient per pulse energy are not easily generated with standard lasers and special care has to be taken when imaging with micrometer precision. If the illuminating laser pulses are too long and thus do not meet the stress confinement requirements, they have a low-pass filtering effect on the generated US frequencies [29]. The higher the desired resolution the shorter the excitation pulses have to be in order to still fulfill the conditions of both the heat diffusion and temporal stress confinements in biological tissues.

If heat and stress confinement requirements are fulfilled, (1.1.1) is valid. However, representing the wave equation in the form of a velocity potential ϕ simplifies finding a solution:[7]

$$\left[\boldsymbol{\nabla}^2 - \frac{1}{v_s^2} \right] \phi = \frac{\beta}{\rho C_P} H, \tag{1.1.5}$$

with ρ being the fluid density. The resulting pressure is then simply calculated as

$$p = -\rho \frac{\partial \phi}{\partial t}. \tag{1.1.6}$$

Equation 1.1.5 can be solved analytically for infinite space and for the case of a uniformly irradiated sphere using Green's functions [49]:

$$\phi(\boldsymbol{x}, t) = -\frac{\beta}{4\pi\rho C_p} \int \frac{H(\boldsymbol{x}, t - \frac{|\boldsymbol{x}-\boldsymbol{x}'|}{v_s})}{|\boldsymbol{x} - \boldsymbol{x}'|} d\boldsymbol{x}. \tag{1.1.7}$$

The heating function $H(r, t)$ created by a very short laser pulse that homogeneously irradiates

---

[7]Representing (1.1.1) using the velocity potential reduces the difficult problem of finding the particle velocity vector to the simpler problem of finding the scalar ϕ. This "trick" is often used in electrostatics and electrodynamics, where the electric field **E**, i.e. a vector field, can be described by the electric potential V, i.e a scalar field. See Chapter 2.3.2 "Comments on Potential" in [48] for a detailed explanation of the benefits gained by such a representation.

a sphere can be expressed as

$$H(r, t) = \mu_a F \Pi_{0,R}(r)\delta(t),$$ (1.1.8)

μ_a the optical absorption coefficient, F the optical fluence, R the sphere radius and where $\Pi_{a,b}(r)$ is a boxcar function defined as

$$\Pi_{a,b}(r) = \begin{cases} 1 \text{ for } a < r < b \\ 0 \text{ otherwise} \end{cases}.$$ (1.1.9)

Equation (1.1.8) hence describes the case of a sphere which is heated by a delta function optical pulse. By inserting (1.1.8) into (1.1.7) one can calculate the velocity function (see [11] for a detailed derivation) from which the resulting pressure field is then calculated using (1.1.6). The pressure field created by a short laser pulse illuminating a sphere can then be found to be

$$p(r, t) = \frac{\mu_a \beta F v_s^2 R}{2 C_P r}(1 - \tau)\Pi_{0,2}(\tau),$$ (1.1.10)

with the dimensionless retarded time τ relative to the perimeter of the sphere

$$\tau = \frac{v_s}{R}\left(t - \frac{r - R}{v_s}\right).$$ (1.1.11)

This pressure field is shown in Figure 1.3 together with the corresponding pressure fields created by an infinity cylinder as well as an infinite layer. The corresponding formulas describing the pressure fields can be derived in a similar fashion as was used to derive (1.1.10) as shown in [11, 33].

By examining the equation for the retarded time (1.1.11), one can find a qualitative description between the size of the illuminated object and the pulse duration Δt. Solving (1.1.11) for t

$$t(\tau) = \frac{\tau R}{v_s} + \frac{r - R}{v_s}$$ (1.1.12)
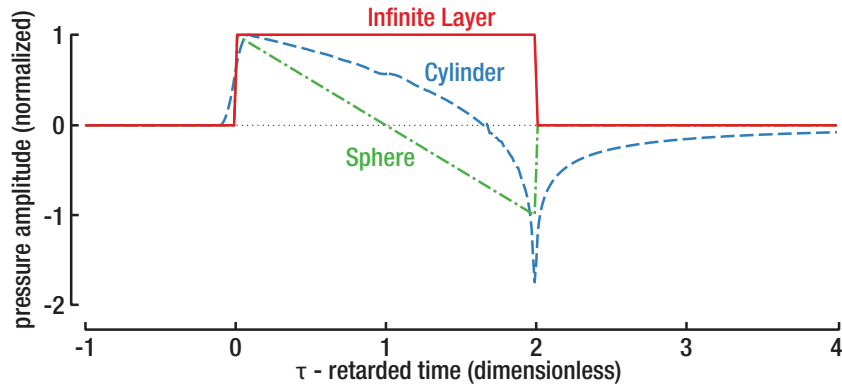
Figure 1.3.: Photoacoustic pressure waves created by homogeneously illuminating a sphere, an infinite cylinder and an infinite layer with a very short laser pulse. Calculated by numerically differentiating the corresponding velocity potentials given in [11].

and calculating the start $(t_1(\tau = 0))$ and end time $(t_2(\tau = 2))$ of the pulse as

$$t_1(\tau = 0) = \frac{r - R}{v_{\mathrm{s}}} \tag{1.1.13}$$

$$t_2(\tau = 2) = \frac{2R}{v_{\mathrm{s}}} + \frac{r - R}{v_{\mathrm{s}}} \tag{1.1.14}$$

the pulse duration Δt can be easily calculated as

$$\Delta t = t_2 - t_1 = \frac{2R}{v_{\mathrm{s}}}. \tag{1.1.15}$$

Hence, the pulse duration decreases for smaller spheres, as is intuitively expected. The smaller the irradiated object, the shorter the generated OA pulse, whereas larger objects will create longer pulses. Small absorbers create shorter pulses, which in turn have a higher bandwidth, and contain higher frequencies. This imposes the second major constraint when designing an OA imaging system. In order to obtain high resolution images, it is important to excite high-frequency and high-bandwidth US waves using nanosecond laser pulses and to measure those generated waves using US sensors sensitive to the generated frequency range. Hence the laser, the US transducer and the subsequent electronics have to be matched in order to obtain optimal imaging results.

1.2. Instrumentation for Optoacoustic Imaging

After having introduced the principles on which all OA imaging systems rely, this section will describe the parts comprising actual OA imaging systems. Section 1.2.1 will discuss the OA imaging chain in principle and sections 1.3.2 and 1.3.1 will discuss the two OA imaging systems most relevant to this thesis, namely OAT and OR-OAM.

1.2.1. The Optoacoustic Imaging Chain

Figure 1.2 provides a very simplicistic view of the underlying principle of OA imaging. Figure 1.4 provides a more realistic overview by more accurately breaking down the single steps taking place in the OA imaging chain.

optical path	acoustic path	electronic path
pulsed (laser) source	ultrasound generation	digitization
light delivery and propagation	us propagation	signal processing
optical absorption	acoustic detection	reconstruction and display
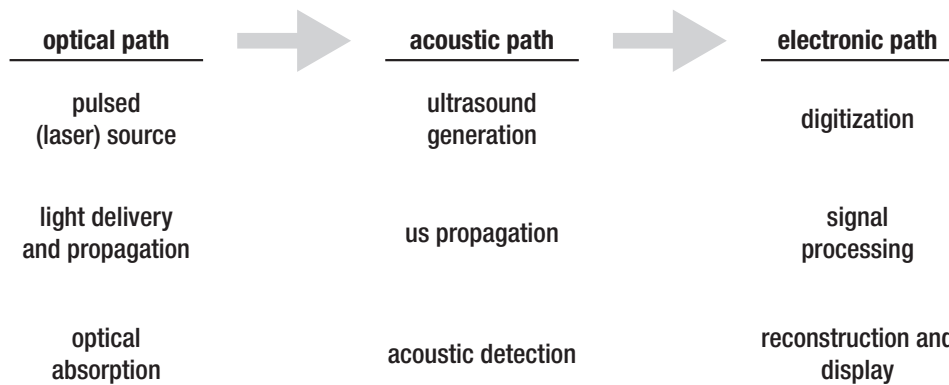
Figure 1.4.: The optoacoustic imaging chain can be broken down into three parts based on the transmitted signal: The optical path, the acoustic path, and the electronic path.

Optical Path   The OA effect is based on laser-generated acoustic waves and hence a suitable pulsed laser source is required in order to efficiently generate OA signals, as already discussed in section 1.1.3 in the context of OA wave generation. Practically all implementations of OA imaging systems rely on high-power, Q-switched laser sources, as those provide the required nanosecond laser pulses. Recently, pulsed LED light sources have also been applied for OA imaging [50], where there low cost and small size could provide significant advantages for translating OA imaging into the clinics.

The generated short pulsed light then has to be delivered to the investigated tissue. Free

beam optics offer great power handling and highly efficient transmission, however they require fixed mirrors and are hence very inflexible in terms of the illumination geometries that can be realized. Optical fibers and optical fiber bundles on the other hand offer great flexibility as they allow an almost arbitrary arrangement for illumination. Hence, OA imaging systems almost exclusively rely on optical fibers to relay the light from the source to the target.

Once light enters biological tissue, it is significantly attenuated, often over distances as short as hundreds of micrometers. The attenuation of light fluence[8] can be expressed as an exponential decay, known in spectroscopy as the Beer-Lambert law [51]. Fluence as a function of the distanced z traveled within a homogenous and attenuating material is described as

$$\Phi(z) = \Phi_0 e^{-\mu_{\text{eff}} z}, \tag{1.2.1}$$

with μ_{eff} being the effective rate of decay, also called transport or absorption coefficient and Φ_0 being the initial fluence. The two main sources of attenuation in tissue are scattering and absorption, i.e.

$$\mu_{\text{eff}} = \mu_a + \mu_s. \tag{1.2.2}$$

Depending on the tissue and wavelength of the propagating wave, either absorption or scattering may dominate [52, 53].

While both scattering and absorption of light occur in biological tissues, scattering typically dominates over absorption [54]. This is the underlying reason why OAT can utilize the rich optical absorption of chromophores but is still capable of penetration depths of several centimeters. Scattering deflects propagating photons from their original direction and the amount of scattering can be characterized by the average distance between scattering events, called the mean free path (MFP), defined as the inverse of the absorption-coefficient, i.e.

---

[8]Light fluence and intensity are often used synonymously, with fluence being the more accurate description (units W/m^2). Sound intensity on the other hand is well defined as the product of pressure and sound velocity, i.e. $\vec{I} = p\vec{v}$ and is therefore not the same as sound pressure. It is noteworthy that the human eye senses light intensity while the human ear directly senses the acoustic pressure.

MFP $= 1/\mu_{\text{eff}}$. In highly scattering tissue, such as brain or skin tissue, the MFP is of the order of $10 - 100\,\mu\text{m}$ [54]. Due to the short MFP, most photons propagating through tissue with a thickness of $100\,\mu\text{m}$ or more will therefore be scattered and will deviate from their original trajectory, resulting in a blurred image. In order to prevent this photon scattering, it is necessary to reduce the distance light travels within the tissue. It is for this reason that tissue slices used for traditional microscopy are only a few micrometers thick, resulting in unscattered photon propagation and high resolution, diffraction-limited images.

Confocal laser scanning microscopy (CLSM), multiphoton fluorescence microscopy (MPF), light sheet fluorescence microscopy (LSFM), and optoacoustic microscopy (OAM) are less limited in their imaging depth in tissue. They are limited by the so-called transport mean free path (TMFP) which takes into account the average angle by which photons are deflected as a result of each scattering event. Since this deflection is typically quite small, it takes approximately ten scattering events until the photon has completely lost its initial direction and undergoes a random walk. Hence, the TMFP lengths are typically one order of magnitude larger than the MFP. Typical values of the TMFP are $0.6\,\text{mm}$ in the brain and $1.1\,\text{mm}$ in muscle tissue [55]. Optical scattering contributes to a significant resolution and fluence loss since the light will leave the tissue after what is effectively a random walk. It is therefore not possible to image through several millimeters or centimeters of scattering tissue using conventional microscopy techniques. The TMFP hence also represents an upper limit to the possible penetration depth in OR-OAM.

Acoustic Path Once light has propagated through the tissue it is absorbed by localized chromophores and will generate an initial temperature rise, which is converted to a pressure rise via thermoelastic expansion. This is the first step of the acoustic path, namely the generation of US waves.

It was shown in section 1.1.3 that the initial pressure distribution generated by local optical absorption of short laser pulses depends on numerous factors. Using equation (1.1.10), the

initial pressure distribution $p(r, t = 0)$ can be expressed more generally as

$$p(r, t = 0) = \frac{\beta v_{\mathrm{s}}^2}{C_P} \mu_a(r) F(r). \tag{1.2.3}$$

Typically, the first part describing the conversion efficiency of energy to pressure is called Grüneisen parameter, $\Gamma = \beta v_{\mathrm{s}}^2 / C_P$, further simplifying equation (1.2.3):

$$p(r, t = 0) = \Gamma \mu_a(r) F(r). \tag{1.2.4}$$

Hence, the amplitude of the generated US pressure waves depend on local optical properties, acoustic properties and the light fluence.

This initial pressure rise propagates as an US wave, and considerations regarding acoustic intensity are equivalent to those described above for optical fluence. However, US scattering in biological tissue is two or three orders of magnitude weaker compared to optical scattering [56]. The TMFP is therefore also two or three orders of magnitude longer, allowing for much higher depth penetration in both conventional US imaging and OAT. Scattering loss typically comprises less than 20% of the overall attenuation for US propagation in soft tissue and it is important to consider absorption as a limiting factor. As was the case for optical attenuation, US attenuation can be described as an exponential decay, where the initial pressure p_0 is attenuated after propagation trough a medium of thickness z:

$$p(z) = p_0 e^{-\alpha z}, \tag{1.2.5}$$

with α the US attenuation coefficient expressed in Np/cm[9]. Just like it's optical counterpart, α depends on the frequency of the propagating US wave:

$$\alpha(f) = \alpha_0 \times f^m. \tag{1.2.6}$$

However, the attenuation in soft tissues is typically approximated to be linear with frequency, i.e. $\alpha \propto f^1$. Typical values for the attenuation coefficient are in the order of

---

[9]$Np = 20 \log_{10} e\, dB \approx 8.685889638$ dB

$0.002\,\mathrm{dB}/(\mathrm{cm} \times \mathrm{MHz})$ for water, $0.17\,\mathrm{dB}/(\mathrm{cm} \times \mathrm{MHz})$ for blood, $0.52\,\mathrm{dB}/(\mathrm{cm} \times \mathrm{MHz})$ for fat, and $1.2\,\mathrm{dB}/(\mathrm{cm} \times \mathrm{MHz})$ for muscle tissue [57]. As an example, US waves with a frequency of $5\,\mathrm{MHz}$ propagating through 1 cm of tissue and assuming an attenuation of $0.75\,\mathrm{dB}/(\mathrm{cm} \times \mathrm{MHz})$ or $0.0863\,\mathrm{Np}/(\mathrm{cm} \times \mathrm{MHz})$ for mixed tissue will be attenuated by 35%. In contrast, a wave with a frequency of 50 MHz propagating through the same tissue will be attenuated by almost 99%. This frequency-dependent absorption results in reduced signal-to-noise ratio (SNR) as well as a temporal dispersion of the acoustic waves and hence contributes to the broadening of the OA signals [58].

In order to form an image based on the generated US waves it is necessary to record a time-resolved electrical signal of the pressure wave using an US transducer. The conversion from pressure waves, i.e. mechanical displacement, to voltage is typically achieved via piezo-electric devices. This conversion step is crucial for all OA imaging systems, as both sensitivity and image resolution are mostly depending on the transducer characteristics. Hence the US transducer is one of the most important components in an OA imaging system. OAT usually utilizes numerous detectors (so called US transducer arrays) while OR-OAM relies on single, high-frequency, and focused US transducers as discussed in more detail in sections 1.3.1 and 1.3.2.

Electronic Path The voltage signals created by the transducer must be amplified, digitized, and processed to be finally analyzed or displayed, which is the last step in the OA imaging chain.

Amplification of the voltage signals close to the source, i.e. the US transducer elements, prior to digitization is often required. Noise sources such as thermal and coupled noise can ultimately not be avoided and the electronic signals generated by the transducer are often only moderately above this fundamental noise level. Using carefully designed and impedance matched low noise amplifiers (LNAs) significantly improves the signal power (typically $20\,\mathrm{dB}$ amplification) while only moderately degrading the SNR [59]. This increased power enables transmission of the electronic signal from the sensing location near the transducer to the analog-to-digital converter (ADC) device with little additional noise being picked up. The

amplifier furthermore acts as an impedance matching element between the high-impedance of most piezoelectric transducers and the 50 Ω input impedance commonly used in ADC devices. Additionally, the increased signal power also allows the ADC to fully utilize its digital range, hence improving the effective number of bits (ENOB)[10].

Digitization is performed using ADCs build into data acquisition systems (DAQs) which can furthermore offer filtering and amplification of the electronic signals prior to digitization. The requirements for the used electronic equipment are dictated by the employed US transducer. When selecting a suitable ADC device, three aspects are most crucial in order to not impede the overall system performance, namely the *resolution*, the *sampling rate* and the *transmission bandwidth*. The requirements for the resolution, expressed as the number of available bits (see also comment on the ENOB above), depend on both the specific implementation as well as the other system parts. Generally, the resolution should be chosen as to not be the limiting factor when digitizing the analog signals. Hence, for a given input range of the ADC, the least significant bit should encode a value that is less or equal to the noise floor of the system. Typical resolutions used in OA imaging systems today are 10 bit to 14 bit [12].

The sampling rate[11] of the ADC has to match both the imaging modality and specifically the used transducer. Here, the *Nyquist–Shannon* sampling theorem has to be fulfilled, which states [60]:

> *"If a function x(t) contains no frequencies higher than B hertz, it is completely determined by giving its ordinates at a series of points spaced $1/(2B)$ seconds apart."*

Hence, a transducer with a bandwidth of 10 MHz has to be sampled at least at twice the rate, i.e. 20 Msps. In reality, accurate digitization requires sampling rates three to four times the

---

[10]The resolution of ADCs is specified by the number of discrete levels used to store the converted analog values which is defined by the number of bits used to represent the value where n-bits provide 2^n discrete levels. The electronics used in ADC devices introduce noise which reduces the number of effectively available bits. This is expressed via the ENOB which specifies the resolution of an ideal ADC with the same resolution.

[11]The analog signal is converted to a stream of numbers called samples. The number of samples per second is called the sampling rate, measured in samples per second (sps).

assumed bandwidth. Generally, OAM utilizes higher bandwidth US transducers and hence requires ADCs with a higher sampling rate while OAT uses numerous, lower bandwidth transducer elements. The requirements for OAM where a single channel is sampled at rates between 100 and 250 Msps are easily fulfilled by modern electronics. In contrast, OAT imaging systems are less demanding in terms of the sample rate (typically less than 40 Msps) but their often huge number of available channels makes digitization challenging.

While not directly a measure of the analog to digital conversion but more of the subsequent communication electronics, a sufficient transmission bandwidth is crucial for high-speed imaging applications both in OAM and OAT . The large number of elements utilized in OAT in combination with sampling rates of 40 Msps or more and imaging depths of a few centimeters result in a large amount of data. For example, using a 512 element transducer sampled with a resolution of 12 bit at 50 Msps and imaging a depth[12] of 5 cm results in $16\,\text{bit} \times 50\,\text{Msps} \times 3.3\,\mu s \times 512 \approx 14\,\text{Mb}$ of data generated by a single laser shot and hence for a single image[13]. As imaging rates in OAT can approach hundreds of Hertz [61], data transmission rates increase accordingly and easily reach hundreds of megabits per second. Taking into account transmission overhead, this can become a limiting factor for the imaging speed if not taken into account when designing an OA system.

Once the digitized signals are transmitted to a PC numerous processing steps are carried out in order to obtain volumetric images of high quality and which allow quantitative analysis of the imaged structures. Those steps include digital filtering[14] preprocessing to reduce the amount of data and speed up processing, correction of the transducers impulse response and most importantly image reconstruction. This reconstruction step is generally straight forward in OAM due to the point-by-point scanning (see Section 1.3.2). In OAT however the

---

[12]With the SOS in water of $\approx 1500\,\text{m/s}$ the 5 cm imaging depth are equivalent to sampling over a period of $\approx 3.3\,\mu s$.

[13]16 bit are required to store and transmit the 12 bit number recorded by the ADC as computers store and transmit numbers in bytes rather than bits.

[14]Typically a bandpass filter is used in order to remove a potential DC-bias and low-frequency artifacts as well as high-frequency noise. The lower cutoff frequency can be estimated as $f_l = c/d$ wit c the speed of sound in water of approximately $1500\,\text{m/s}$ and d the size of the field-of-view (FOV). Hence, for larger FOVs f_l has to be reduced accordingly, as larger structures generate lower frequency OA responses. Typically values for f_l are around 50 kHz for OAT and 200 kHz for OAM . The upper cutoff frequency should be chosen as to match the upper limit of the US transducers sensitivity.

reconstruction is decisive for the final image quality. Numerous reconstruction approaches exist, each driven by obtaining higher quality images as fast as possible. In general, two major approaches exist, namely back-projection or model-based reconstruction. The former is computationally highly effective and allows real-time visualization of OA images with high frame rates when being performed on a GPU [62] while model-based reconstructions provide higher image quality and obtain more accurate and hence quantitative reconstructions. Despite their importance for OAT imaging, reconstruction approaches and their implementations were not part of the presented thesis and are hence beyond the scope of this introduction. Numerous reviews and books provide a thorough introduction into the topic [5, 6, 9–11, 63–65].

1.2.2. Sensitivity of Optoacoustic Imaging Systems

The overall acoustic sensitivity of an OA imaging system is limited by both the transducer and the electronic characteristics and is ultimately limited by thermal acoustic noise [66]. Any OA imaging system's sensitivity can be quantified using the noise equivalent pressure (NEP) [67]:

$$\text{NEP}(f) = \sqrt{k_B T[1 + F_n/\eta(f)]Z_a/A}} \tag{1.2.7}$$

with k_B the Boltzmann constant, T the temperature, F_n the noise factor, $\eta(f)$ the efficiency of the US transducer at frequency f, Z_a is the acoustic impedance of the medium, and A the detector area. Here, $\eta(f)$ and A are evidently depending only on the utilized transducer while the noise factor F_n is influenced by both the transducer and amplification electronics. The combination of transducer efficiency and area together with the added electronic noise therefore imposes a fundamental lower limit to the sensitivity of the OA imaging system. The NEP of resonant, spherically focused US transducers with a high Q-factor and this low damping is in the order of tens of $\mu\text{Pa}/\sqrt{\text{Hz}}$ due to their very high on-resonance efficiency $\eta(f)$. However, these undamped, resonant transducers are not suitable for the detection of broadband OA signals. The broadband transducers used in OA imaging typically have much lower efficiencies, resulting in typical NEPs of approximately $1\,\text{mPa}/\sqrt{\text{Hz}}$.

Recently, novel approaches to US detection are driven by the need for affordable, high-frequency US arrays with many elements. Here, optical sensors and capacitive micromachined ultrasonic transducers (cMUTs) seem to be the most promising candidates to replace conventional piezoelectric transducers. The former, optical detection approaches already provide sensitivities as low as $2\,\text{mPa}/\sqrt{\text{Hz}}$ [68] while cMUTs with even better sensitivity of $0.9\,\text{mPa}/\sqrt{\text{Hz}}$ [69] have been achieved. Both approaches allow the integration of US transducer into miniature catheters, since their performance is less dependent on the sensitive area. For example, a fiber based transducer with an microscopic[15] effective area of only $270\,\mu\text{m} x 125\,\mu\text{m} = 0.03 mm^2$ showed a sensitivity of $25\,\text{mPa}/\sqrt{\text{Hz}}$ [70].

1.3. Practical Implementations of Optoacoustic Imaging Systems

The two implementations of OA imaging, OAT and OR-OAM, which are of most interest for this thesis are shown schematically in Figure 1.5 together with conventional optical microscopy and pulse echo US imaging. This section provides a quick overview of how the challenges of light delivery and acoustic detection are solved in practical OA imaging implementations while focusing on the OAT and OAM imaging systems used for the presented thesis. Section 1.3.1 also presents a general description of the 3D-array based system which was used for the publication presented in Chapter 3. Section 1.3.2, focusing on OAM , also presents the hybrid-focus optoacoustic microscope (HFOAM) system which is described and characterized in detail in the publication presented in Chapter 4.

1.3.1. Optoacoustic Tomography

Optoacoustic tomography is probably the best known OA imaging modality due to its suitability for imaging on various size scales and the combination of endogenous contrast, centimeter scale imaging depth and very high achievable imaging speeds. This enables potential application in all stages of bio-medical research, from investigations on cells and molecules

---

[15]This area is approximately four times the cross-sectional area of a human hair!
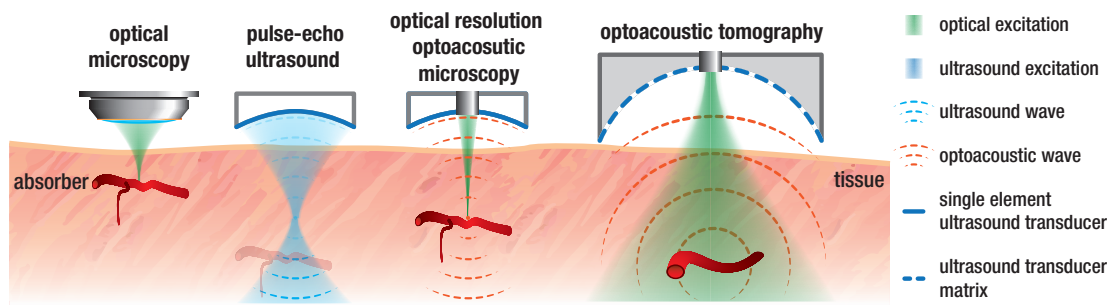
Figure 1.5.: Comparison of optoacoustic imaging systems...

over whole-mouse imaging to imaging on humans [10, 71, 72]. OAT, shown schematically on the right of Figure 1.5 is characterized by a combination of diffuse light delivery and simultaneous acoustics detection by hundreds of transducer elements. The simple and diffuse light delivery and volumetric image reconstruction following a single laser pulse makes OAT the most general and least restrictive OA imaging technique.

Light sources for OAT have to provide large per pulse energies of several millijoule since the light is evenly distributed in the tissue where it needs to generate sufficient OA signals even after propagating trough optically thick tissue. To this end, diode pumped, actively q-switched optical parametric oscillators (OPOs) are used [73]. These lasers combine the required millijoules pulse energies with repetition rates of more than $100\,\mathrm{Hz}$ while also being wavelength tunable. The ability to perform rapid wavelength switching between individual shots enables multispectral OAT , which allows for label-free, functional imaging [8, 74].

Light delivery from the laser source to the sample is typically performed using commercially available fiber light guides. Those bundles are easy to use due to their large size and their resulting ruggedness, making them very suitable for experimental work in the laboratory or for use in clinical settings. However, they are expensive and limit the illumination geometry. Recently, our group has investigated the application of inhouse-made optical fiber bundles. These bundles can be made cheaply and quickly based on the required geometry and my work on these bundles has led to the publication presented in Chapter 3.

Once light is delivered to the target, OA signals are generated, propagate through the tissue and acoustic detection is performed by US transducer arrays with typically at least 128 elements and with up to 512 and more elements in recent implementations. The transducer

elements are arranged on a either planar, cylindrical, or spherical surfaces. All three geometries can be used in OAT but cylindrical and spherical arrangements are preferred for their increased sensitivity due to mechanical focusing. However, since cylindrical and spherical detection geometries require access around the target and have a reduce FOV and are hence more limited to applications such as breast or mouse imaging. Planar arrays do not have these limitations and can hence be easier applied to imaging humans, however at the cost of reduced SNR.

Conventional US imaging systems utilize transducer arrays consisting of a large number of piezoelectric elements [75]. Similar arrays are used in OAT as these arrays can provide video-rate imaging since no mechanical scanning of the transducer is necessary and they can be applied for real time OA imaging [55, 76]. However, the fabrication of US arrays with a high number of elements, high central frequency and high bandwidth is still challenging, making the US transducer arrays one of the most expensive parts of any OAT system.

Figure 1.6 shows an illustration of a modern OAT imaging system as used in our laboratory. This system was the basis for the publication described in detail in Chapter 3 and has been used extensively in recent years [62, 77, 78]. An OPO based laser (Innolas Laser GmbH, Krailling, Germany) provides nanosecond ($<$10 ns) pulses in the visible wavelength range with up to 100 Hz repetition rate. The laser light is coupled into a fiber bundle and the distal end of the bundle terminates in a central bore of a spherical high frequency US matrix array. The US matrix array consists of 256 or 512 detection elements distributed on a spherical cap and a three to four cm radius[16]. The resolution of OAT imaging systems depends on various factors such as transducer bandwidth, aperture, sensing geometry, and sampling and can further be influenced by the imaged sample. However, as a first approximation the transducer's bandwidth typically is the main factor limiting the spatial resolution. For a transducer with a large detection bandwidth, the resolution can be approximated as

$$\delta_r \approx 0.8 \times \lambda_{\text{cut-off}} = \frac{c}{f_{\text{cut-off}}}. \tag{1.3.1}$$

---

[16]Our lab utilizes both a 256 and a 512 element transducer with similar geometries.

with $\lambda_{\text{cut-off}}$ the cut-off wavelength defined as $c/f_{\text{cut-off}}$ and c the SOS in water[17]. The individual US transducer elements have a central frequency of 4 MHz and 100% detection bandwidth. The resulting cut-off frequency of 6 MHz predicts a resolution of approximately 200 μm which has been experimentally validated.
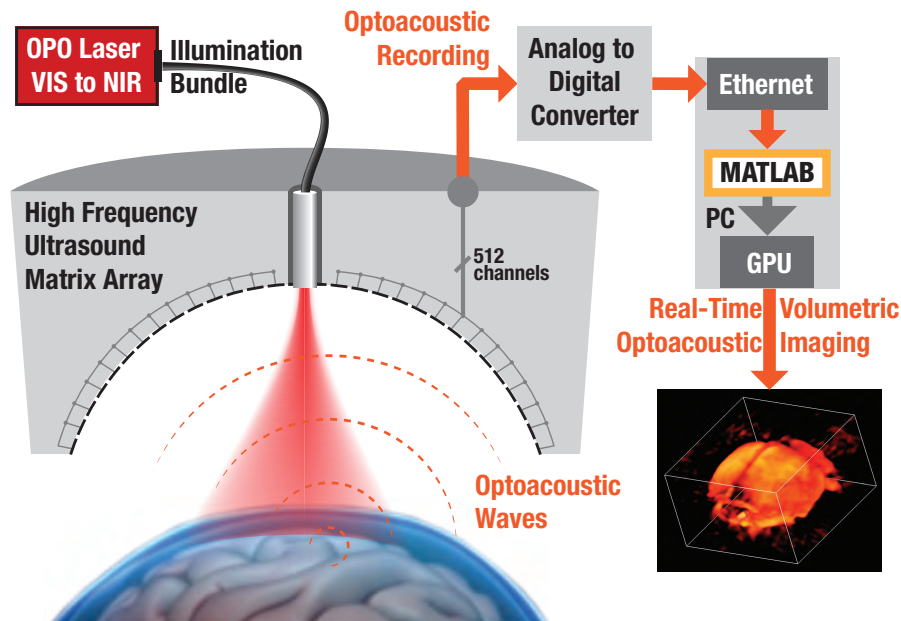
Figure 1.6.: Exemplary optoacoustic tomography implementation illustrating the main parts of every OAT system, namely a pulsed light source, diffuse light delivery, and tomographic detection using multiple transducers and image reconstruction.

1.3.2. Optoacoustic Microscopy

Much like optical microscopy, OR-OAM utilizes focused light for the excitation of OA signals. As indicated in Figure 1.5, this reduces the depth penetration of OAM to the quasi-ballistic photon regime and hence a depth of less than 1 mm compared to several centimeter depth penetration possible with OAT imaging in the diffusive regime (see also paragraph *optical path* in Section 1.2.1)[18].

Almost all OAM implementations rely on confocal optical illumination and acoustic detec-

---

[17]See Section 1.3.2 for a derivation of Equation 1.3.1

[18]For this chapter, OAM will be assumed to mean OR-OAM. A description of acoustic-resolution optoacoustic microscopy (AR-OAM) is beyond the scope of this thesis and interested readers are referred to [29, 79–81].

tion[19], as shown in an exemplary way in both in Figure 1.5 and 1.8. Each focused excitation pulse is aimed at a different spot in the target for which a time-resolved OA response is recorded. The excitation pulse is then moved over the specimen and hence a volumetric image can be formed "step by step" and without the need for computationally expensive image reconstruction.

The spatial resolution is typically anisotropic in OAM systems, and one has to distinguish between the lateral resolution δ_r and the axial resolution δ_z. This difference in resolution is a result of the confocal optical illumination and acoustic detection. The lateral or in-plane (typically x/y-axes) resolution is given by the employed optics and the resulting optical focus. The axial resolution describes the resolution along the transducer axis (typically the z-axis), i.e. along the propagation direction of the US waves and is a result of the characteristics of the US transducer.

The lateral resolution of OAM is determined by the optical focus, assuming an optical focus smaller than the acoustic focus as is the case for virtually all OR-OAM implementations. The lateral resolution δ_r in focus is limited by optical diffraction and can be estimated using the well known Abbe diffraction limit [83]:

$$\delta_r = \frac{\lambda}{2n\sin\theta} = \frac{\lambda}{2\text{NA}} \tag{1.3.2}$$

with λ the optical wavelength, n the refractive index of the propagation medium[20], θ the opening half-angle and NA the numerical aperture. With modern, high-quality immersion objectives, a resolution of less than one micrometer can easily be achieved using visible light [85].

While high resolution is a desirable quality for any imaging system, one has to also take into account the achievable depth of focus (DOF). The Rayleigh length, defined as the distance from the focus for which the area of the beams cross section is doubled, is a possible way to

---

[19] A notable exception of OAM without this confocal design was presented by Allen *et al.* in 2018 [82]. There, focused optical excitation is performed using galvanometric mirrors while acoustic detection is performed with a stationary, unidirectional US transducer.

[20] Since OA requires acoustic coupling between the sample and the US transducer, the propagation medium is almost exclusively water with a refractive index of 1.33 in the visible range [84].

define the DOF. For a Gaussian beam, the Rayleigh length z_R is calculated as [86]:

$$z_R = \frac{\pi w_0^2}{\lambda} \qquad (1.3.3)$$

with w_0 the radial beam size in focus. One can easily appreciate the compromise that has to be made between resolution and DOF when replacing w_0 with the in-focus resolution δ_r defined in Equation 1.3.2 and expressing the DOF as twice the Rayleigh length, as both areas before and behind the focal spot are of interest:

$$\text{DOF} = 2z_R = \frac{2\pi w_0^2}{\lambda} = \frac{\pi \delta_r^2}{2\lambda} = \frac{\pi \lambda}{8\text{NA}^2}, \qquad (1.3.4)$$

which is close to the value found by Born and Wolf [87, 88]:

$$\text{DOF} = \frac{\lambda}{2\text{NA}^2}. \qquad (1.3.5)$$

Comparing Equations 1.3.4 to 1.3.2 it is noteworthy that the resolution is an inversely proportional function of the NA while the DOF scales quadratically with the inverse of the NA. Hence, doubling the NA will double the achievable resolution while the DOF will be four times smaller. Figure 1.7 and Table 1.1 illustrate this tradeoff between high resolution and low DOF for realistically achievable values of the NA between 0.01 and 1.3.

Table 1.1.: Comparison of NA, lateral resolution and DOF in practical OR-OAM implementations.

Author	Year	NA	d (μm)	DOF (μm)	Ref.
Zhang *et al.*	2010	1.23	0.22	0.2[*]	[85]
Zhang *et al.*	2012	0.50	0.58	1.0	[89]
Hu *et al.*	2011	0.13	2.56	15[*]	[90]
Maslov *et al.*	2008	0.10	3.70	40	[91]
Yao *et al.*	2015	0.10	3.00	83	[92]
Rebling *et al.*	2018	0.015	12.0	2000	[93]

[*] Value not provided but calculated based on NA.

Superior depth penetration is one of the major advantages of OAM compared to conventional optical microscopy. It is for this reason, that most practical OAM implementations
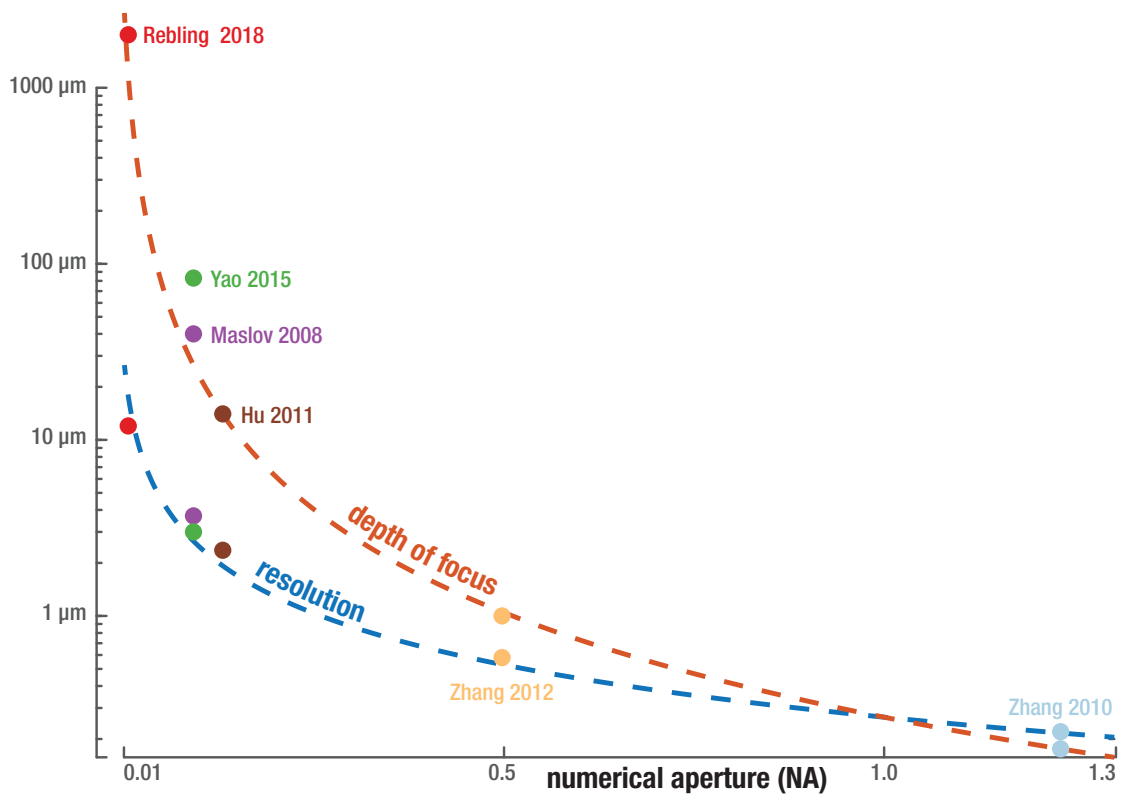
Figure 1.7.: Lateral resolution and depth of focus as function of the numerical aperture. See Table 1.1 for numerical values and references.

trade in-focus resolution for enhanced depth-of-field. This can be seen by the relatively low NA optics used in most of the OAM implementations shown. Almost all systems have an NA of less than 0.5 with the majority having an NA of approximately 0.1 and with the exception of the work by Zhang *et al.* [85]. The limited DOF shown in Figure 1.7 and Table 1.1 are caused by the strongly diverging beams when using high NA objectives and are not due to photon scattering. Hence, DOF is not equal to the achievable depth penetration. As mention in Section 1.2.1, the latter is limited by the ballistic photon regime and is approximately 1 mm in scattering biological tissue for all OAM implementations. The DOF does however limit the effective depth penetration for a single scan in OAM . OAM implementations with a large NA such as those presented by Zhang *et al.* [85] requires numerous scans at various depths to fully image a thick or curved sample[21]. OAM systems with a low NA, such as

---

[21] Acquiring images at various focal planes is commonly used in conventional optical microscopy. This so-called

the one presented in Chapter 4 sacrifice sub-micron resolution for an extended DOF, thus eliminating the need for z-stacking.

The axial resolution δ_z is determined mainly by the frequency bandwidth B for which the US transducer is sensitive, as was the case for OAT described in Section 1.3.1. The point-spread function (PSF) of any imaging system can be used to fully characterize the resolution [94]. When a real-world signal is measured, the PSF is convoluted with the actual signal and produces the measured signal. The width of the PSF is therefore a direct indication of the signal quality and ultimately of the resolution. This is easily understood in the frequency domain, where the modulation transfer function (MTF), i.e. the Fourier transform of the PSF, describes the band-pass function of the system. Since a convolution in the time domain is simply a multiplication in the frequency domain, one can easily appreciate the filtering function of the MTF. The band-pass function $H(k)$ of a real US transducer will have a limited frequency bandwidth and will act as a low-pass filter with a cutoff frequency $f_{\text{cut-off}}$, i.e.

$$H(k) = \begin{cases} 1 \text{ for } f \leq f_{\text{cut-off}} \\ 0 \text{ otherwise} \end{cases}, \tag{1.3.6}$$

and hence with a bandwidth B that is equal to the cut-off frequency: $B = f_{\text{cut-off}}$. It can be shown[22] that the axial PSF of a photoacoustic point source located at r_a as a function of the band-pass function $H(k)$ is given as

$$\text{PSF}_z(R) = \frac{1}{2\pi^2} \int_0^\infty H(k) j_0(kR) k^2 dk, \tag{1.3.7}$$

with $R = |\boldsymbol{r} - \boldsymbol{r}_a|$ being the distance from the point source, j_n the spherical Bessel function of the first kind and k the wavenumber, defined as $k = \frac{2\pi}{\lambda} = \frac{2\pi f}{c}$. The integration in (1.3.7) can be performed, and after normalization one obtains

$$\text{PSF}(R) = \frac{3 j_1(k_{\text{cut-off}} R)}{k_{\text{cut-off}} R}. \tag{1.3.8}$$

---

focus-stacking or z-stacking improves the DOF at the cost of increased acquisition times.
[22] See section 5.3 "Bandwidth-Limited PSFs" in [11].

The resolution of a system is often defined using the full-width at half-maximum (FWHM). Using $3j_1(x)/x = 0.5$ when $x = 2.4983$, the axial resolution δ_z is easily computed as

$$\delta_z = 2 \times \frac{2.4983}{k_{\text{cut-off}}} \approx 0.8 \times \lambda_{\text{cut-off}} \approx 0.8 \times \frac{c}{f_{\text{cut-off}}}. \tag{1.3.9}$$

It is evident that in order to maximize the axial resolution of an OAM system, it is necessary to use US transducers with a high bandwidth. The larger the bandwidth, the tighter the resulting PSF and the better the achievable resolution. For an US transducer with a bandwidth $B = 30\,\text{MHz}$ it is possible to obtain an axial resolution of $\delta_z \approx 40\,\mu\text{m}$. However, there is an upper limit to improving the bandwidth and hence the axial resolution. In addition to the difficulties of manufacturing very high frequency transducers with bandwidths of $100\,\text{MHz}$ and more, US is strongly attenuated for those high frequencies, again limiting the depth penetration to less than 1 mm.

The illuminated volume[23] in OAM is several orders of magnitude smaller when compared to OAT . The diffuse illumination used in OAT requires a homogenous illumination of the entire FOV at once, i.e. illumination of more than $1\,\text{cm}^2$ with fluences of several mJ/cm^2 and hence several mJ per-pulse energy. In contrast, OAM is based on illuminating an area smaller than the US focus, with beam diameters of only a few micrometers. In addition, the use of focused and hence more sensitive US transducers further reduces the required light fluence. As a result, OAM requires lasers with per-pulse energies of typically less than $1\,\mu\text{J}$. While the per-pulse energy requirements are modest in OAM , laser with much higher pulse repetition frequencies (PRFs) are needed. In order to sample a FOVs of 10 mm by 10 mm with a step size of $10\,\mu\text{m}$ within one minute, a minimum PRF of $16\,\text{kHz}$ is required. This is several order of magnitude faster than the few tens of hertz typically utilized in OAT . Modern OAM implementations hence utilize fast diode-pumped solid-state (DPSS) lasers with PRFs of $100\,\text{kHz}$ and more in order to facilitate rapid imaging [95, 96]. Per-pulse energies of $1\,\mu\text{J}$ for nanosecond pulses are easily achieved with modern DPSS lasers. However, the required combination of microjoule energies at kilohertz rates generates average powers of several

---

[23]The physically important quantity in both OAT and OAM is the energy deposited or available per tissue volume, i.e. light or energy density (W/m^3). However, light is delivered from the outside of tissue and hence light fluence (W/m^2) is typically used to describe the illumination in OA imaging.

watts, which requires carefully engineered and hence expensive lasers.

Light delivery in OAM is again performed using fiber light guides. Unlike OAT where bulky multi-mode fiber (MMF) bundles are used, OAM relies on small and fragile single-mode fibers (SMFs) to deliver OA excitation light. OAM requires an optimally tight optical focus. Only SMF can provide this diffraction limited performance, as the additional modes propagating in a MMF increase the spot size in focus [86]. While SMFs provide the smallest spot sizes when their output is focus, they are also significantly more difficult to handle and efficient coupling into the micrometer-sized fibers is challenging. A typical SMF which is optimized for operation in the visible range between 450 nm and 600 nm has a core diameter of 2.5 µm [97], compared to several hundred micrometers for MMFs. This small core diameter hence requires strong focusing and the resulting high fluences can easily burn and destroy the fiber when the pulse energies are to high. For applications where per-pulse energies of several microjoule are required in combination with diffraction limited operation[24], SMFs are hence not a feasible option. As an alternative, photonic crystal fibers (PCFs) can be used. The specifically structured air gaps present in fibers such as the LMA-20 [99] create a larger mode area (20 µm) while still only allowing single-mode operation. Hence, these fibers can handle per-pulse energies of 10 µJ and more at PRFs of several kilohertz.

As described earlier in this section, OAM relies on optically focusing the excitation light pulses to a size smaller than the US transducers focus. The light exiting the SMF is collimated and then focused using high-NA microscope objectives for sub-micrometer resolution or simple aspherical lenses when a lower NA is required. Alternatively, light exiting the SMF can also be focused using a gradient-index (GRIN) lens which is directly attached to the fiber, as shown in Figure 1.8 on the right for the HFOAM scan-head. Focusing using GRIN lenses significantly reduces the size of the scan-head when compared to conventional optics.

US detection in OAM can be performed both with focused and unfocused US transducers or even US arrays [100]. However, most modern OAM systems make use of spherically focused, high-frequency and high bandwidth US transducers due to their superior sensitivity. This high sensitivity is required as OAM allows for no averaging due to the fast scanning

---

[24]For example, an early version of the HFOAM system investigated short and long-term phototoxicity in cell colonies with per-pulse energies of more than 10 µJ [98].

and since pulses with energies of less than $1\,\mu J$ are used. The lateral resolution in OAM is determined by the optical focus while the axial resolution is dictated by the US transducer characteristics (see beginning of this section). In order for the resolution anisotropy to remain small, US transducers with central frequencies and bandwidths of $10\,MHz$ to $80\,MHz$ are used. The higher the transducer bandwidth, the better the resulting axial resolution (between $120\,\mu m$ for $10\,MHz$ and $15\,\mu m$ for $80\,MHz$ bandwidth using Equation 1.3.9). However, for frequencies beyond $10\,MHz$ US attenuation in tissue is no longer negligible and can limit the depth penetration to less than the optical penetration depth for frequencies beyond $50\,MHz$.

One major challenge in OAM which OAT does not face is the joint scanning of the acoustic and optical focus. The imaging speed of most OAM systems is limited either by this scanning speed or the laser PRF. Hence many scanning approaches exist, each differing in complexity, imaging speed and FOV which are described briefly below.

Mechanical Raster Scanning Both the US transducer and the focusing optics are mechanically raster-scanned over the sample in a point-by-point fashion. This scanning modality is easiest to implement, as any two simple linear stages are sufficient for imaging. While the FOV can be very large for this scanning method, in reality it is limited by the very slow imaging speed of this method. Post-processing is trivial since the target is sampled in a regular grid and hence no remapping of the data is required and one can directly obtain maximum amplitude projection (MAP) or cross section (B-scan) images. The slow scanning speed of raster scanning results from the need to move to a position, stop the scan head there, probe the sample and then move to the next position. The combination of these small mechanical steps and communication overhead results in much fewer A-scans per second than most DPSS lasers are capable of. The first OAM systems used this scanning methods for its simplicity but modern OAM system no longer use this approach due to B-scan rates[25] of less than $1\,Hz/mm$ [85, 101].

---

[25]Imaging speed is compared using the B-scan rate expressed in sampled points (A-scans) per distance, i.e. Hz/mm independent of the FOV which can be achieved by the system in order to facilitate comparison of the imaging speed.

Quasi-continuous Mechanical Scanning   In this modality US transducer and focusing optics are again scanned by two orthogonal mechanical stages, much like in the mechanical raster scanning. However, both stages are moved continuously over the sample with one slower stage moving linearly over the region of interest (ROI) while a second, fast stage oscillates rapidly, thus creating a zig-zag or sinusoidal sampling pattern. This eliminates communication overhead and the stages can fully accelerate without having to stop for every step. The improved scanning speed comes at the cost of more complicated, expensive and time-consuming readout and post-processing as the target is no longer sampled at regular intervals and thus the data has to be remapped to a regular grid. The step-size and hence resolution of this modality is then determined by the laser PRF. A PRF of 10 kHz will result in a step size of 10 µm for a stage moving with a peak velocity of 100 mm/s. When trying to optimize the scanning speed in the quasi-continuous mode one has to pay careful attention to the combination of required step-size, laser PRF, and obtainable stage speed, as either can impose a limit on the imaging speed. Modern direct drive linear stages can provide thrusts as high as 15 N, reaching velocities of up to 1400 mm/s over less than 1 cm. While the imaging rate is significantly faster than that of mechanical raster scanning, both methods share the advantage of basically arbitrarily large FOVs. Scan FOVs of 10 mm by 10 mm can be imaged with a B-scan rates of 50 Hz/mm and with modern linear drives offering potentially even faster operation [93, 102, 103].

Mirror Scanning   With modern laser sources reaching PRFs of 100 kHz and more, even fast moving mechanical stages become a factor limiting the imaging speed. Fast scanning galvanometric or micro mirrors can be used to achieve imaging rates beyond what is possible with even advanced mechanical scanning, much like in other optical scanning microscopy such as confocal microscopy or optical coherence tomography (OCT) [104]. Fundamentally, one can differentiate between techniques in which both the optical and US focus are scanned and those in which the optical focus is scanned within the sensitive FOV of the US transducer. The maximal possible imaging speed in OAM can be achieved when the optical focus is scanned within the static FOV of a non-moving US transducer. In order to not sacrifice

detection sensitivity, the optical focus can be scanned within the FOV of a focused US transducer. While offering B-scan rates of up to 180 Hz/mm, the FOV is then severely limited to an size of less than 300 μm [82, 105]. This very limited FOV can be overcome when using unfocused US transducers, thus achieving a FOV of approximately 1 mm with a B-scan rate of 93 Hz/mm. However, the sensitivity is significantly reduced in these systems due to the lack of US focusing. Combined mirror scanning of the optical and US focus provides fast OAM imaging while not sacrificing as much on the obtainable FOV. Typically, a single mirror is used to provide fast-scanning along one axis while a simple motorized stage provides sufficient speed for the slower axis. Several mirror devices have been proposed, all of which have to operate in a liquid in order to enable US propagation. Using a custom made microelectromechanical systems (MEMS) scanning mirror a 3 mm FOV has been achieved with a B-scan rate of 1.2 kHz/mm in 2015 [92] while a 12 mm FOV with a B-scan rate of 10.8 kHz/mm was shown recently [92].

The electronic path in OAM is trivial compared to OAT since only a single US channel needs to be sampled. Sampling rates of 100 Msps and more are required to fulfil the *Nyquist–Shannon* sampling theorem, but DAQs with this performance are readily available. The combination of time-resolved detection of the US waves in combination with the x-y scanning described above readily generates a volumetric images without the need for sophisticated reconstruction algorithms.

Figure 1.8 is a schematic of the basic components of the HFOAM OR-OAM imaging system which has been developed in our laboratory during the last years. This system was the basis for the publication presented in Chapter 4 where it is also described in detail. In short, nanosecond pulsed excitation is provided by a 532 nm Nd:YAG DPSS laser which in turn pumps a tunable dye laser with the wavelength set to 578 nm where blood shows a peak absorbance. The per-pulse energy can be adjusted using a combination of a half-wave plate and a polarizing beam splitter (PBS). Part of the beam is sampled using a combination beam sampler (BS) and a photodiode (PD) in order to correct for fluctuations in the per-pulse energies. The beam is launched into a PCF whose output is terminated in the combined

US and OA scan-head shown in the right of Figure 1.8. The scan-head is comprised of a spherically focused US transducer with a central aperture. The PCF is terminated inside this aperture where a GRIN lens provides co-axial focusing of the optical and US foci.
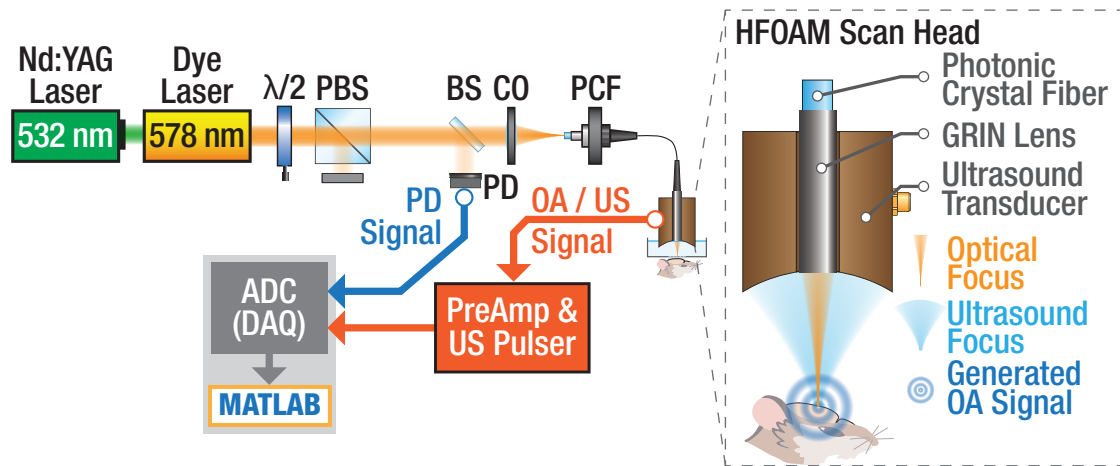
Figure 1.8.: Schematic of the HFOAM optical resolution optoacoustic microscope when setup for morphological imaging, i.e. using one wavelength. $\lambda/2$-half-wave plate, PBS-polarizing beam splitter, BS-beam sampler, CO-collimating lens, PCF-photonic crystal fiber, PD-photodiode

References

[1] Minghua Xu and Lihong V. Wang. „Photoacoustic imaging in biomedicine". In: *Review of Scientific Instruments* 77.4, 041101 (2006).
DOI: 10.1063/1.2195024.

[2] L. V. Wang. „Multiscale photoacoustic microscopy and computed tomography". In: *Nat Photonics* 3.9 (2009), pp. 503–509. ISSN: 1749-4885 (Print) 1749-4885 (Linking).
DOI: 10.1038/nphoton.2009.157.

[3] Paul Beard. „Biomedical photoacoustic imaging". In: *Interface focus* (2011).
DOI: 10.1098/rsfs.2011.0028.

[4]   L. V. Wang and S. Hu. „Photoacoustic Tomography: In Vivo Imaging from Organelles to Organs". In: *Science* 335.6075 (Mar. 2012), pp. 1458–1462. DOI: 10.1126/science.1216210.

[5]   C. Lutzweiler and D. Razansky. „Optoacoustic imaging and tomography: reconstruction approaches and outstanding challenges in image performance and quantification". In: *Sensors (Basel)* 13.6 (2013), pp. 7345–84. DOI: 10.3390/s130607345.

[6]   A. Rosenthal, V. Ntziachristos, and D. Razansky. „Acoustic Inversion in Optoacoustic Tomography: A Review". In: *Curr Med Imaging Rev* 9.4 (2013), pp. 318–336. DOI: 10.2174/15734056113096660006.

[7]   J. Xia and L. V. Wang. „Small-animal whole-body photoacoustic tomography: a review". In: *IEEE Trans Biomed Eng* 61.5 (2014), pp. 1380–9. ISSN: 1558-2531 (Electronic) 0018-9294 (Linking). DOI: 10.1109/TBME.2013.2283507.

[8]   Adrian Taruttis and Vasilis Ntziachristos. „Advances in real-time multispectral optoacoustic imaging and its applications". In: *Nature Photonics* 9.4 (2015), pp. 219–227. DOI: 10.1038/nphoton.2015.29.

[9]   L. V. Wang and J. Yao. „A practical guide to photoacoustic tomography in the life sciences". In: *Nat Methods* 13.8 (2016), pp. 627–38. ISSN: 1548-7105 (Electronic) 1548-7091 (Linking). DOI: 10.1038/nmeth.3925.

[10]   Deán-Ben X. L. et al. „Advanced optoacoustic methods for multiscale imaging of in vivo dynamics". In: *Chemical Society Reviews* 46.8 (2017), pp. 2158–2198. DOI: 10.1039/c6cs00765a.

[11]   Lihong V. Wang. *Photoacoustic Imaging and Spectroscopy*. CRC Press, Mar. 2009. ISBN: 9781420059915.

[12]   Malini Olivo, U. S. Dinish, et al. *Frontiers in Biophotonics for Translational Medicine*. Springer, 2016.

[13] Werner Siemens. „Science in Germany". In: *Nature* 13.319 (Dec. 1875), p112.
      DOI: 10.1038/013112a0.

[14] Werner Siemens. „Üeber den Einfluss der Beleuchtung auf die Leitungsfähigkeit des
      krystallinischen Selens." In: *Monatsberichte der Königlichen Preussische Akademie
      des Wissenschaft* (May 1875), p. 280.
      DOI: 10.1007/978-3-662-36584-7_23.

[15] Alexander Bell and Sumner Tainter. „On the production and reproduction of sound
      by light". In: *American Journal of Science* 20 (Oct. 1880), pp. 305–324.
      DOI: 10.2475/ajs.s3-20.118.305.

[16] Alexander Graham Bell and Sumner Tainter. „Selenium and the Photophone". In:
      Nature 22 (Sept. 1880).
      DOI: 10.1038/022500a0.

[17] John Tyndall. „Action of an Intermittent Beam of Radiant Heat upon Gaseous Mat-
      ter". In: *Proceedings of the Royal Society of London* (1880).
      DOI: 10.1098/rspl.1880.0037.

[18] Alexander Graham Bell. „THE PRODUCTION OF SOUND BY RADIANT EN-
      ERGY". In: *Science* os-2.49 (1881), pp. 242–253.
      DOI: 10.1126/science.os-2.49.242.

[19] Wilhelm C. Röntgen. „On tones produced by the intermittent irradiation of a gas".
      In: *Philosophical Magazine Series 5* (1881).
      DOI: 10.1080/14786448108627021.

[20] Rayleigh. „The Photophone". In: *Nature* 23 (Jan. 1881), pp. 274–275.
      DOI: 10.1038/023274a0.

[21] M. L. Veingerov. „New Method of Gas Analysis Based on Tyndall-Roentgen Opto-
      Acoustic Effect". In: *Dokl. Akad. Nauk. (USSR)* 19.687 (1938).

[22] M. E. Delany. „The optic-acoustic effect in gases". In: *Science Progress* 47 (1959),
      pp. 459–467.

[23] A. Rosencwaig. „Photoacoustic Spectroscopy of Biological Materials“. In: *Science* 181.4100 (1973), pp. 657–658.
DOI: 10.1126/science.181.4100.657.

[24] L. B. Kreuzer and C. K. N. Patel. „Nitric oxide air pollution: Detection by optoacoustic spectroscopy“. In: *Science* 173.3991 (1971), pp. 45–47.
DOI: 10.1126/science.173.3991.45.

[25] Pietro Patimisco et al. „Recent advances in quartz enhanced photoacoustic sensing“. In: *Applied Physics Reviews* 5.1 (2018), p. 011106.
DOI: 10.1063/1.5013612.

[26] A. Rosencwaig. „Photoacoustic spectroscopy of solids“. In: *Optics Communications* 7.4 (1973), pp. 305–308.
DOI: 10.1016/0030-4018(73)90039-4.

[27] T. Bowen. „Radiation-Induced Thermoacoustic Soft Tissue Imaging“. In: *1981 Ultrasonics Symposium*. Oct. 1981, pp. 817–822.
DOI: 10.1109/ULTSYM.1981.197737.

[28] Robert A. Kruger et al. „Thermoacoustic CT with Radio Waves: A Medical Imaging Paradigm 1“. In: *Radiology* 211.1 (1999), pp. 275–278.
DOI: 10.1148/radiology.211.1.r99ap05275.

[29] Murad Omar, Jérôme Gateau, and Vasilis Ntziachristos. „Raster-scan optoacoustic mesoscopy in the 25 – 125 MHz range“. In: *Optics Letters* 38.14 (July 2013), pp. 2472–2474.
DOI: 10.1364/OL.38.002472.

[30] D. Razansky, S. Kellnberger, and V. Ntziachristos. „Near-field radiofrequency thermoacoustic tomography with impulse excitation“. In: *Medical Physics* 37.9 (2010), pp. 4602–.
DOI: 10.1118/1.3467756.

[31]   Stephan Kellnberger et al. „Near-field thermoacoustic tomography of small animals".
        In: *Physics in Medicine and Biology* 56.11 (2011), p. 3433.
        DOI: 10.1088/0031-9155/56/11/016.

[32]   Dane Bicanic, ed. *Photoacoustic and Photothermal Phenomena III: Proceedings of
        the 7th International Topical Meeting (Springer Series in Optical Sciences)*. Springer,
        Oct. 1991.

[33]   G. J. Diebold, T. Sun, and M. I. Khan. „Photoacoustic monopole radiation in one,
        two, and three dimensions". In: *Physical review letters* 67.24 (1991).
        DOI: 10.1103/physrevlett.67.3384.

[34]   T. Sun and G. J. Diebold. *Generation of ultrasonic waves from a layered photoacoustic
        source*. 1992.
        DOI: 10.1038/355806a0.

[35]   Robert A. Kruger et al. „Thermoacoustic molecular imaging of small animals." In:
        Molecular imaging 2.2 (2003), pp. 113–123.
        DOI: 10.1162/15353500200303109.

[36]   Robert A. Kruger. „Photoacoustic ultrasound". In: *Medical Physics* 21.1 (1994),
        pp. 127–131.
        DOI: 10.1118/1.597367.

[37]   A. A. Oraevsky et al. „Laser-based optoacoustic imaging in biological tissues". In: *So-
        ciety of Photo-Optical Instrumentation Engineers (SPIE) Conference Series*. Vol. 2134.
        Society of Photo-Optical Instrumentation Engineers (SPIE) Conference Series. Aug.
        1994, A122.
        DOI: 10.1117/12.182927.

[38]   A. A. Oraevsky et al. „Time-resolved optoacoustic imaging in layered biological tis-
        sues". In: *Advances in Optical Imaging and Photon Migration* 21 (1994), pp. 161–
        165.

[39] R. A. Kruger et al. „Photoacoustic ultrasound (PAUS)–reconstruction tomography.“ In: *Medical Physics* 22.10 (1995), pp. 1605–9.

DOI: 10.1118/1.597429.

[40] Alexander A. Oraevsky et al. „Laser optoacoustic tomography for medical diagnostics: principles“. In: *Proc. SPIE*. Ed. by Robert A. Lieberman, Halina Podbielska, and Tuan Vo-Dinh. Vol. 2676. Biomedical Sensing, Imaging, and Tracking Technologies I, 22. Apr. 1996, pp. 22–31.

DOI: 10.1117/12.238786.

[41] Rinat O. Esenaliev et al. „Laser optoacoustic imaging for breast cancer diagnostics: limit of detection and comparison with x-ray and ultrasound imaging“. In: *Proc. SPIE, Optical Tomography and Spectroscopy of Tissue: Theory, Instrumentation, Model, and Human Studies II*. Vol. 2979. 1997, pp. 71–82.

DOI: 10.1117/12.280213.

[42] C. G. A. Hoelen et al. „Three-dimensional photoacoustic imaging of blood vessels in tissue“. In: *Optics Letters* 23.8 (1998), pp. 648–650.

DOI: 10.1364/OL.23.000648.

[43] G. Ku and L. V. Wang. „Scanning thermoacoustic tomography in biological tissue.“ In: *Medical physics* 27.5 (2000), pp. 1195–1202.

DOI: 10.1118/1.598984.

[44] Daniel Razansky and Vasilis Ntziachristos. „Hybrid photoacoustic fluorescence molecular tomography using finite-element-based inversion“. In: *Medical Physics* 34.11 (2007), pp. 4293–4301.

DOI: 10.1118/1.2786866.

[45] R. O. Esenaliev, A. A. Karabutov, and A. A. Oraevsky. „Sensitivity of laser optoacoustic imaging in detection of small deeply embedded tumors“. In: *IEEE Journal of Selected Topics in Quantum Electronics* 5.4 (1999), pp. 981–988.

DOI: 10.1109/2944.796320.

[46] E. Marin. „Characteristic dimensions for heat transfer". In: *Latin-American Journal of Physics Education* 8.1 (Mar. 2014), pp. 56–60.

[47] M. A. El-Brawany et al. „Measurement of thermal and ultrasonic properties of some biological tissues". In: *Journal of Medical Engineering & Technology* 33.3 (Jan. 2009), pp. 249–256.
DOI: 10.1080/03091900802451265.

[48] David J. Griffiths. *Introduction to Electrodynamics (3rd Edition)*. 3rd. Addison Wesley, Jan. 1999.

[49] Philip McCord Morse and Herman Feshbach. *Methods of Theoretical Physics, Part I*. McGraw-Hill Science/Engineering/Math, June 1953.

[50] Yunhao Zhu et al. „Light Emitting Diodes based Photoacoustic Imaging and Potential Clinical Applications". In: *Scientific reports* 8.1 (2018), p. 9885. ISSN: 2045-2322.
DOI: 10.1038/s41598-018-28131-4.

[51] Beer. „Bestimmung der Absorption des rothen Lichts in farbigen Flüssigkeiten". In: *Annalen der Physik* 162.5 (1852), pp. 78–88.
DOI: 10.1002/andp.18521620505.

[52] W.-F. Cheong, S. A. Prahl, and A. J. Welch. „A review of the optical properties of biological tissues". In: *Quantum Electronics, IEEE Journal of* 26.12 (Dec. 1990), pp. 2166–2185.
DOI: 10.1109/3.64354.

[53] Francis A. Duck. *Physical Properties of Tissue: A Comprehensive Reference Network*. Academic Press, Feb. 1990.

[54] Fritjof Helmchen and Winfried Denk. „Deep tissue two-photon microscopy." In: *Nature methods* 2.12 (2005), pp. 932–940.
DOI: 10.1038/nmeth818.

[55] V. Ntziachristos and D. Razansky. „Molecular imaging by means of multispectral optoacoustic tomography (MSOT)". In: *Chemical Reviews* 110.5 (2010), pp. 2783–94.

DOI: 10.1021/cr9002566.

[56] Thomas L. Szabo. *Diagnostic Ultrasound Imaging: Inside Out, Second Edition (Biomedical Engineering)*. 2nd ed. Academic Press, Dec. 2013.

[57] James A. Zagzebski. *Essentials Of Ultrasound Physics*. Mosby, 1996. ISBN: 0815198523.

[58] X. Luíis Deán-Ben, Daniel Razansky, and Vasilis Ntziachristos. „The effects of acoustic attenuation in optoacoustic signals". In: *Physics in Medicine and Biology* 56.18 (2011), p. 6129.

DOI: 10.1088/0031-9155/56/18/021.

[59] Martin Werner. „Rauschen in Kommunikationssystemen". In: *Nachrichten-Uebertragungstechnik: Analoge und digitale Verfahren mit modernen Anwendungen* (2006), pp. 138–157.

[60] Claude Elwood Shannon. „Communication in the presence of noise". In: *Proceedings of the IRE* 37.1 (1949), pp. 10–21.

DOI: 10.1109/jproc.1998.659497.

[61] Ali Özbek, Xosé Luís Deán-Ben, and Daniel Razansky. „Optoacoustic imaging at kilohertz volumetric frame rates". In: *Optica* 5.7 (2018), pp. 857–863.

DOI: 10.1364/optica.5.000857.

[62] Deán-Ben X. L., A. Ozbek, and D. Razansky. „Volumetric real-time tracking of peripheral human vasculature with GPU-accelerated three-dimensional optoacoustic tomography". In: *IEEE Trans Med Imaging* 32.11 (2013), pp. 2050–5.

DOI: 10.1109/TMI.2013.2272079.

[63] J. Xia, J. Yao, and L. V. Wang. „Photoacoustic tomography: principles and advances". In: *Electromagn Waves (Camb)* 147 (2014), pp. 1–22.

[64] Changhui Li and Lihong V. Wang. „Photoacoustic tomography and sensing in biomedicine". en. In: *Physics in Medicine and Biology* 54.19 (Oct. 2009), R59.

DOI: 10.1088/0031-9155/54/19/R01. (Visited on 01/11/2014).

[65] Daniel Razansky. „Multispectral Optoacoustic Tomography—Volumetric Color Hearing in Real Time". In: *IEEE Journal of Selected Topics in Quantum Electronics* 18.3 (2012), pp. 1234–1243.
DOI: 10.1109/jstqe.2011.2172192.

[66] Robert H. Mellen. „The Thermal-Noise Limit in the Detection of Underwater Acoustic Signals". In: *The Journal of the Acoustical Society of America* 24.5 (1952), pp. 478–480.
DOI: 10.1121/1.1906924.

[67] Amy M. Winkler, Konstantin Maslov, and Lihong V. Wang. „Noise-equivalent sensitivity of photoacoustics". In: *Journal of Biomedical Optics* 18.9 (Sept. 2013), p. 097003.
DOI: 10.1117/1.jbo.18.9.097003.

[68] Edward Z. Zhang and Paul C. Beard. „A miniature all-optical photoacoustic imaging probe". In: *Photons plus ultrasound: imaging and sensing 2011*. Vol. 7899. International Society for Optics and Photonics. 2011, 78991F.
DOI: 10.1117/12.874883.

[69] I. O. Wygant et al. „An integrated circuit with transmit beamforming flip-chip bonded to a 2-D CMUT array for 3-D ultrasound imaging". In: *IEEE Trans Ultrason Ferroelectr Freq Control* 56.10 (2009), pp. 2145–56.
DOI: 10.1109/TUFFC.2009.1297.

[70] Georg Wissmeyer et al. „All-optical optoacoustic microscope based on wideband pulse interferometry". In: *Optics letters* 41.9 (2016), pp. 1953–1956.
DOI: 10.1364/ol.41.001953.

[71] Thomas Felix Fehm et al. „In vivo whole-body optoacoustic scanner with real-time volumetric imaging capacity". In: *Optica* 3.11 (2016), pp. 1153–1159.

[72] Deán-Ben X. L. and D. Razansky. „Functional optoacoustic human angiography with handheld video rate three dimensional scanner". In: *Photoacoustics* 1.3-4 (2013), pp. 68–73.
DOI: 10.1016/j.pacs.2013.10.002.

[73] Frank J. Duarte. *Tunable laser applications*. CRC press, 2016.

[74] Daniel Razansky et al. „Multispectral opto-acoustic tomography of deep-seated fluorescent proteins in vivo". In: *Nature Photonics* 3.7 (2009), pp. 412–417.
      DOI: 10.1038/nphoton.2009.98.

[75] J. M. Cannata et al. „Development of a 35-MHz piezo-composite ultrasound array for medical imaging". In: *IEEE Transactions on Ultrasonics, Ferroelectrics and Frequency Control* 53.1 (Jan. 2006), pp. 224–236.
      DOI: 10.1109/TUFFC.2006.1588408.

[76] J. J. Niederhauser et al. „Combined ultrasound and optoacoustic system for real-time high-contrast vascular imaging in vivo". In: *Medical Imaging, IEEE Transactions on* 24.4 (Apr. 2005), pp. 436–440.
      DOI: 10.1109/TMI.2004.843199.

[77] A. Buehler et al. „Three-dimensional optoacoustic tomography at video rate". In: *Optics express* 20.20 (2012), pp. 22712–22719.
      DOI: 10.1364/oe.20.022712.

[78] Xosé Luís Deán-Ben and Daniel Razansky. „Adding fifth dimension to optoacoustic imaging: volumetric time-resolved spectrally enriched tomography". In: *Light: Science & Applications* 3.1 (2014).
      DOI: 10.1038/lsa.2014.18.

[79] Roman Gr. Maev, ed. *Advances in Acoustic Microscopy and High Resolution Imaging: From Principles to Applications*. 1st ed. Wiley-VCH, Apr. 2013.
      DOI: 10.1002/9783527655304.

[80] Murad Omar et al. „Ultrawideband reflection-mode optoacoustic mesoscopy". In: *Optics Letters* 39.13 (July 2014), pp. 3911–3914.
      DOI: 10.1364/OL.39.003911.

[81] J. Aguirre et al. „Mesoscopic optoacoustic tomography at 100 MHz reveals skin layers". In: *Optics Letters (accepted)* (2014).

[82] Thomas J. Allen et al. „Large area laser scanning optical resolution photoacoustic microscopy using a fibre optic sensor“. In: *Biomedical optics express* 9.2 (2018), pp. 650–660.
DOI: 10.1364/boe.9.000650.

[83] Ernst Abbe. „Beiträge zur Theorie des Mikroskops und der mikroskopischen Wahrnehmung“. In: *Archiv für mikroskopische Anatomie* 9.1 (1873), pp. 413–418.
DOI: 10.1007/bf02956173.

[84] Masahiko Daimon and Akira Masumura. „Measurement of the refractive index of distilled water from the near-infrared region to the ultraviolet region“. In: *Applied optics* 46.18 (2007), pp. 3811–3820.
DOI: 10.1364/ao.46.003811.

[85] Chi Zhang, Konstantin Maslov, and Lihong V. Wang. „Subwavelength-resolution label-free photoacoustic microscopy of optical absorption in vivo“. In: *Optics letters* 35.19 (2010), pp. 3195–3197.
DOI: 10.1364/ol.35.003195.

[86] Eugene Hecht. *Optics*. 4th ed. Addison-Wesley, Aug. 2001.
DOI: 10.1119/1.1987895.

[87] I. T. Young et al. „Depth-of-focus in microscopy“. In: *8th Scandinavian Conference on Image Analysis, Tromso, Norway*. Citeseer. 1993.

[88] Max Born et al. *Principles of Optics*. Cambridge University Press, 1999. ISBN: 9781139644181.
DOI: 10.1017/cbo9781139644181.

[89] Chi Zhang et al. „Reflection-mode submicron-resolution in vivo photoacoustic microscopy“. In: *Journal of biomedical optics* 17.2 (2012), p. 020501.

[90] Song Hu, Konstantin Maslov, and Lihong V. Wang. „Second-generation optical-resolution photoacoustic microscopy with improved sensitivity and speed“. In: *Optics letters* 36.7 (2011), pp. 1134–1136.
DOI: 10.1364/ol.36.001134.

[91] Konstantin Maslov et al. „Optical-resolution photoacoustic microscopy for in vivo imaging of single capillaries." In: *Optics letters* 33.9 (2008), pp. 929–931. DOI: 10.1364/OL.33.000929.

[92] J. Yao et al. „High-speed label-free functional photoacoustic microscopy of mouse brain in action". In: *Nature Methods* 12.5 (2015), pp. 407–10. DOI: 10.1038/nmeth.3336.

[93] **Johannes Rebling** et al. „Dual-wavelength hybrid optoacoustic-ultrasound biomicroscopy for functional imaging of large-scale cerebral vascular networks". In: *Journal of biophotonics* (May 2018), e201800057. DOI: 10.1002/jbio.201800057.

[94] Jack D. Gaskill. *Linear Systems, Fourier Transforms, and Optics (Wiley Series in Pure and Applied Optics)*. 1st ed. Wiley-Interscience, June 1978.

[95] Yizhi Liang et al. „2 MHz multi-wavelength pulsed laser for functional photoacoustic microscopy". In: *Optics letters* 42.7 (2017), pp. 1452–1455. DOI: 10.1364/ol.42.001452.

[96] Wei Qin et al. „Large-field-of-view optical resolution photoacoustic microscopy". In: *Optics Express* 26.4 (Feb. 2018), p. 4271. DOI: 10.1364/oe.26.004271.

[97] Nufern. *460-HP*. 2018. URL: https://www.nufern.com/pam/optical_fibers/881/460-HP/ (visited on 10/16/2018).

[98] Sven Gottschalk et al. „Short and long-term phototoxicity in cells expressing genetic reporters under nanosecond laser exposure". In: *Biomaterials* 69 (Nov. 2015), pp. 38–44. DOI: 10.1016/j.biomaterials.2015.07.051.

[99] Thorlabs. *LMA-20 - ESM Large Mode Area Photonic Crystal Fiber*. 2018. URL: https://www.thorlabs.de/thorproduct.cfm?partnumber=LMA-20 (visited on 10/16/2018).

[100] Tian Jin et al. „Portable optical-resolution photoacoustic microscopy for volumetric imaging of multiscale organisms". In: *Journal of Biophotonics* 11.4 (Nov. 2017), e201700250.

DOI: `10.1002/jbio.201700250`.

[101] Junjie Yao and Lihong V. Wang. „Photoacoustic microscopy". en. In: *Laser & Photonics Reviews* 7.5 (2013), p. 758778.

DOI: `10.1002/lpor.201200060`. (Visited on 01/11/2014).

[102] L. Wang et al. „Fast voice-coil scanning optical-resolution photoacoustic microscopy". In: *Optics Letters* 36.2 (2011), pp. 139–41.

DOI: `10.1364/OL.36.000139`.

[103] H. Estrada et al. „Real-time optoacoustic brain microscopy with hybrid optical and acoustic resolution". In: *Laser Physics Letters* 11.4 (2014), p. 45601.

DOI: `Artn04560110.1088/1612-2011/11/4/045601`.

[104] Jeffrey M. Larson, Stanley A. Schwartz, and Michael W. Davidson. *Resonant scanning in laser confocal microscopy*. 2000. URL: `www.microscopyu.com/techniques/confocal/resonant-scanning-in-laser-confocal-microscopy`.

[105] Bin Rao et al. „Real-time four-dimensional optical-resolution photoacoustic microscopy with Au nanoparticle-assisted subdiffraction-limit resolution". In: *Optics Letters* 36.7 (Mar. 2011), p. 1137.

DOI: `10.1364/ol.36.001137`.

2. Optoacoustic characterization of capacitive micromachined ultrasonic transducers

Summary and Author Contribution

The emerging technology of capacitive micromachined ultrasonic transducers (cMUTs) has greate potential in optoacoustic (OA) imaging. The cMUTs technology offers various potential advantages over existing, piezo-electric transducers, including a large bandwidth and high central frequency, a large number of transducer elements at moderate costs and superior electronic performance. Those advantages make them ideal transducers to be used in optoacoustic tomography (OAT) , where hundreds of broadband transducer elements are required for high quality and quantitative imaging. The French company Vermon, a research partner of our group, is actively pursuing the development of cMUTs to complement their existing line of lead zirconate titanate (PZT) transducers. This study was jointly developed during my secondment at Vermon where I helped to build a first ultrasound (US) transducer test bench that was used to characterize US transducers in transmit-receive mode [2]. All authors agreed that an OA characterization of the tested transducers would be beneficial to better access their performance for OA imaging. I proposed a characterization setup based on an OA absorber, utilizing the optical parametric oscillator (OPO) laser and motorized stages available in our laboratory at the *"Institute of Biological and Medical Imaging"* (IBMI). This

system was used to characterize and compare the bandwidth and angular sensitivity of a conventional PZT transducer to that of a cMUT with similar geometry.

My contribution to the presented manuscript where the following:

Methodology I implemented the hardware required for the characterization measurement, including the mechanical stages, optical alignment, phantom preparation, transducer mounting and electronics with help from OW. I also developed the software required to automate the characterization, i.e. software controlling the stages and the data acquisition system (DAQ). I furthermore developed a model to measure the transducer directivity using only a simple linear motion while correcting for the source-sensor distance. Data for the characterization of the tested US transducers was collected with help from OW.

Analysis I developed all code required to process and analyze the collected data using Matlab. I also implemented the developed model to extract the transducer directivity. For imaging reconstruction I adapted code provided by the k-Wave toolbox [3]. I analyzed the collected data using the Matlab code I developed.

Writing and Revisions I drafted the initial manuscript with significant contributions from all authors. I created all figures using Matlab and Adobe Illustrator with critical suggestions from all authors. I performed additional experiments, amended the manuscript and modified the figures as per reviewer request and with significant contributions from Daniel Razansky.

This study was presented at the *SPIE Medical Imaging 2017* conference, where it won a poster award [4].

Abstract

Frequency characteristics of ultrasounds detectors used in optoacoustic tomography have a major impact on imaging performance. It is common practice to select transducers based on their sensitivity at the central frequency and under normal incidence. However, the bandwidth and angular sensitivity play an equally important role in establishing the quality and accuracy of the reconstructed images. Here we developed a calibrated optoacoustic characterization method specifically tailored for broadband measurements of the angular transducer sensitivity (directivity). Ultrawideband omnidirectional optoacoustic responses were generated by uniformly illuminating thin absorbing sutures with nanosecond laser pulses and characterized with a needle hydrophone. This calibrated optoacoustic source was used to characterize the frequency dependence of the angular response of a conventional lead zirconate titanate ultrasonic transducers (PZT-UTs) and a cMUTs with similar size and central frequency. Furthermore, both transducers had no pre-amplification electronics directly attached to the detection elements. While the PZT-UT presented a 7.8 dB sensitivity advantage at normal incidence, it was only able to provide detectable signal-to-noise levels at incidence angles of up to 20° whereas the cMUT maintained reasonable sensitivity levels and broadband response at incidence angles of 40° and beyond. We further experimentally showcase a reduction in the limited-view image artifacts resulting from the broader acceptance angle of the cMUT.

2.1. Introduction

High performance OA tomographic systems rely on the use of multi-element arrays to simultaneously capture the emitted broadband OA responses at multiple locations around the imaged object. A clear trade-off exists between the size, sensitivity and bandwidth of the individual detection elements and key performance characteristics, such as signal-to-noise and contrast-to-noise, imaging frame rate, as well as the quantitativeness and accuracy of the reconstructed images [5–8]. Conventional piezoelectric transducers used in pulse-echo medical US imaging and non-destructive-testing (NDT) applications, such as those made of PZT composites, are designed to have a strong directivity. As a result, US waves are preferentially

emitted and detected at angles close to normal incidence, contributing to a good signal-to-noise performance of those probes. However, due to the omnidirectional and ultrawideband nature of the generated OA responses [9, 10], such strong transducer directivity is not a desirable feature for OA imaging applications and may result in limited-view reconstruction artifacts, thus impairing the visual appearance, spatial resolution and quantitativeness of the images [7, 11, 12].

While piezocomposite transducers have so far dominated the medical imaging field, the emerging technology of cMUT has seen a rapid development in the last decade. CMUTs utilize existing silicon fabrication technology and allow the tight integration of receive electronics with the transducer, thus improving the noise characteristics while also reducing the need for extensive cabling [13, 14]. Both linear and matrix arrays with a very high element count can be realized, thus offering great prospects for the US imaging field [15–18]. The intrinsically low mechanical impedance mismatch of the thin vibrating cMUT membranes results in a generally broader bandwidth and good transduction efficiency. This better acoustic coupling eliminates the need for complicated matching layers which are typically used in piezoelectric transducers[19]. Those matching layers are optimized for pulse-echo US imaging, thus hindering detection of obliquely incident waves and rendering cMUT transducers better candidates for efficient detection of broadband, omnidirectional OA signals.

To this end, the feasibility of OA imaging with cMUTs has been demonstrated by a number of studies [20–23]. Yet, broadband directivity patterns of typical cMUTs have not been systematically studied. Typically, the frequency response of US transducers is characterized via comparison to a calibration standard, e.g. by using self-reciprocity [24–26] or by optical interferometry[27–30]. Directivity measurements then utilize a broadband acoustic signal generated by nonlinear propagation of an acoustic wave emitted by a second US transducer [31–33]. However, those methods are not well suited for accurate characterization of broadband directivity in receive mode. An OA calibration method has been suggested recently for frequency calibration of ultrasonic sensors [34], however, its utility for directivity measurements has not been investigated. Yet, the precise knowledge of the detector's directivity over a broad frequency range is not only advantageous for the purpose of optimal

transducer selection but can also be used as a priori knowledge during the inversion process that can aid in reducing reconstruction artifacts via correction for the frequency and spatial response of the transducers using model-based approaches [11, 12].

The ultimate image quality and detection sensitivity of OA tomography depends on multiple factors, among them the amount of light reaching the imaged location, distribution of the local optical absorption coefficient, US attenuation in the medium, as well as tomographic coverage, sensitivity and directivity of the detection system [6, 35, 36]. In this paper we concentrate on the last element in this chain, i.e. characteristics of the US transducers employed for recording the generated OA signals. In particular, we propose a calibrated OA characterization method specifically tailored for broadband directivity measurements of the angular transducer sensitivity which is readily applicable for the detector characterization in most existing OA imaging setups. The technique further allows for a direct and reproducible comparison between different types of detectors by accounting for the end-to-end, angular frequency response of the entire imaging system. The method was used for characterizing the frequency dependence of the angular response of a conventional PZT-UT and a cMUT transducer with similar size and central frequency.

2.2. Materials and Methods

2.2.1. Experimental Setup

Figure 2.1 shows a schematic representation of the experimental setup used for transducer characterization in a two-dimensional setting. In the presented system, the US directivity measurement is not performed using a frequency swept US emitter but instead relies on the generation of broadband, omni-directional US waves via the OA effect. At the heart of the method is an OA emitter consisting of a $100\,\mu m$ diameter highly-absorbing surgical suture (Ethilon, 5-0 gauge, Polyamide 6 black monofilament, Ethicon US). For the OA signal excitation, the suture was embedded in 1.5% clear agarose, fixed in a water tank and illuminated with short high-energy laser pulses. The $10\,ns$ duration pulses were generated by an optical parametric oscillator-based laser (Innolas Laser GmbH, Krailling, Germany) at

a wavelength of 720 nm, per-pulse energy of around 16 mJ, and a pulse repetition rate of 50 Hz. The pulsed light was guided from the laser to the suture by means of a custom-made, four-arm fiber bundle (CeramOptec GmbH, Bonn, Germany). The four branches of the fiber bundles, each delivering one fourth of the laser energy, were fixed in the water tank on both sides of the suture at a distance of approximately 3 cm, uniformly illuminating the entire 4 mm-long absorbing suture. In this way, the suture served as an acoustic line source emitting a broadband cylindrical acoustic wave.
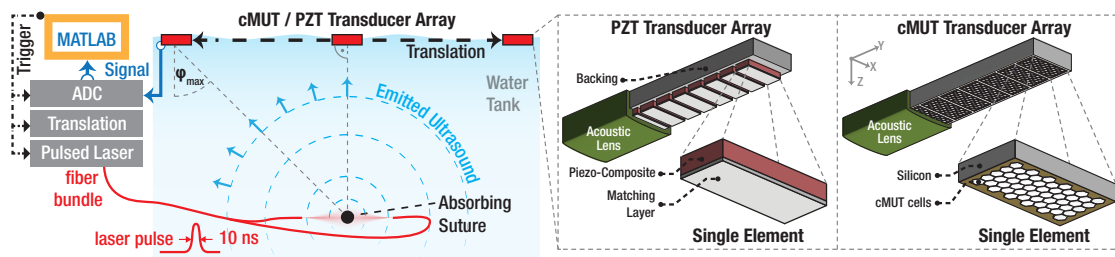
Figure 2.1.: Experimental setup to perform the OA characterization of broadband directivity patterns (left side). The system employs an OA broadband source which is formed by an absorbing suture which generates broadband cylindrical acoustic waves upon illumination with short laser pulses. The cylindrical waves propagate trough a water tank and are detected by the transducer under test at an incidence angle φ depending on the transducer position. The method was used to characterize the frequency dependence of the angular response of a conventional PZT and a cMUT with similar size and central frequency (shown on the right).
Reproduced with permission from [1]. © SPIE.

To effectively create a delta OA source in both time and space, both temporal heat and stress confinement criteria are to be fulfilled by the source [37]. Heat confinement requires for heat diffusion in the absorbing suture to be negligible for the duration of the laser pulse, which is readily satisfied for pulse durations < 1 µs. The temporal stress confinement also requires that the pressure relaxation during the laser pulse is negligible. This is the case if the duration of the laser pulse is shorter than the time required for the pressure wave to propagate out from the absorbing structure. For the 100 µm diameter suture and an approximate speed of sound in Polyamide 6 of 2620 m/s [38], it would take approximately 40 ns for the generated OA wave to leave the suture, which is much longer than the 10 ns duration of the excitation laser pulse.

In order to measure the transducer's directivity, it is necessary to measure its sensitivity for

detecting waves impinging under different angles. Conventional transmit-receive directivity measurements commonly employ a rotating US emitter in order to generate acoustic plane waves under different angles. The rotation axis of the emitter then needs to be fixed at the position of the sensor under investigation, which requires a precise and cumbersome alignment of both transducers. In contrast, our suggested method measures the directivity using a simple linear translation of the tested transducer. As indicated in Fig. 2.1, the angle between the normal of the US wavefront and the normal of the transducer then only depends on the lateral position (along the y-axis) of the transducer. This translation was performed using a simple motorized linear stage (RCP3-TA5C, IAI Industrieroboter GmbH, Schwalbach, Germany) with a travel range of 50 mm but could in principle also be done with a manual stage.

The complete directivity measurement was synchronized using custom developed MATLAB interface, which controlled the laser, the linear stage as well as the data acquisition system. For each transducer position, several laser shots were triggered, and a data acquisition system digitized and recorded the US time signals for each laser shot.

2.2.2. Transducer Broadband Directivity Comparison

To verify the assumption that the absorbing suture truly acts as a broadband acoustic source, the proposed characterization method was validated using needle hydrophones. A calibrated polyvinylidene fluoride (PVdF) needle hydrophone with a 1 mm diameter was used together with a matching wide-band amplifier and a direct current (DC) coupler (Precision Acoustics Ltd, Dorchester, United Kingdom). The hydrophone provides a nearly flat frequency response up to 10 MHz and has an excellent sensitivity due its large active area. In order to measure the frequency content of the generated OA signals, the hydrophone was lowered into the water tank and centered over the suture at a distance of 11 mm. The generated acoustic signals were digitized with 100 MS/s using a dedicated 12 bit DAQ (ATS9351, Alazar Technologies Inc., Pointe-Claire, Canada) connected to the DC coupler output. The laser was triggered with 50 Hz for 10 s and 500 averages were acquired at each position in order to optimize the signal-to-noise ratio (SNR).

The directivity measurement method proposed here is based on the assumption that the long surgical suture will emit nearly ideal cylindrical waves when illuminated with pulsed laser radiation. This assumption cannot be accurately verified with the 1 mm hydrophone owing to its inherent directivity due to spatial averaging by the 1 mm active area. We therefore used a PVdF needle hydrophone with a 75 μm diameter which was translated by means of the motorized linear stage. The 75 μm hydrophone has a very broad acceptance angle, performing nearly as a point detector for the investigated frequency range. The hydrophone was placed in the water tank at a distance of 13 mm from the suture and translated over a lateral range of 40 mm with 200 μm steps, resulting in 201 discrete time signals each averaged again over 500 consecutive pulses.

Subsequently, two similar PZT and cMUT linear array prototypes (VERMON S.A., Tours, France) were characterized, both having 200 μm element pitch and central frequency around 5 MHz. A detailed description of the manufacturing process of the PZT-UT and the cMUT is available elsewhere [19, 39]. Both transducers used an acoustic lens to focus along the elevational (long) axis of the linear arrays. For the directivity measurement, the single elements of the transducer, accessed through a custom-made breakout board, were connected to an analog front-end (AFE) specifically designed for ultrasound measurements (AFE5809 Evaluation Module, Texas Instruments, Dallas, United States). The AFE had 8 analog inputs, each combining low-noise amplifiers (total gain 54 dB) and a 40 MHz, 14 bit analog to digital convertor having a band-pass filter with cut-off frequencies between 50 kHz and 15 MHz. The AFE also offered a programmable active termination allowing for impedance matching between the transducers and the DAQ in order to optimize system performance. The directivity measurement carried out for both the PZT-UT and the cMUT was almost identical to that of the 75 μm hydrophone described above. The pulse repetition rate of the laser was reduced to 10 Hz as compared to 50 Hz used for the hydrophone characterization to account for the slow acquisition speed of the AFE. Each transducer head was immersed in the water tank and positioned at a distance of approximately 10 mm from the suture, corresponding to the acoustic focus of the transducers. Both transducers were translated over a range of 50 mm with a step size of 200 μm and 9 temporal optoacoustic waveforms

were averaged per position.

In order to eliminate dependence of our results on the laser energy fluctuations, we measured the long term pulse-to-pulse energy variability of the laser system. Over a typical measurement period of 100 s, the laser energy fluctuates between a minimum value of 15.6 mJ and a maximum value of 17.2 mJ with a standard deviation 3.02%. However, since signals from 9 consecutive shots were averaged in our measurements, the actual dependence on the laser energy fluctuations is somewhere between 16.1 mJ and 16.5 mJ, i.e. standard deviation of below 0.5%, much lower than the range of the measured differences in the transducer sensitivity.

2.2.3. Data Analysis

The recorded US time signals were processed and analyzed using a custom made MATLAB script in order to obtain the transducer sensitivity and directivity. A zero-phase first-order Butterworth high-pass infinite impulse response (IIR) filter having a cut-off frequency of 500 kHz was applied to all the signals in order to remove DC offsets and low frequency components. The individual signals measured at each transducer position were then averaged and used to extract the exact position of the transducer with respect to the suture. As explained in the previous section, the presented directivity measurement does not rely on the rotation of an emitter but instead relies on a linear translation of the receiving (tested) transducer with respect to a line source. In order to retrieve the angle under which the cylindrical wave was incident on the transducer surface, it is necessary to know the precise location of the transducer with respect to the suture in the y-z plane. For a given position along the y-axis, the time of arrival of the OA signal originating at position (y_0,z_0) can be expressed as

$$t(y) = \sqrt{\frac{(y - y_0)^2}{c^2} + \frac{z_0^2}{c^2}} \qquad (2.2.1)$$

with c being the speed of sound in water and y the transducer position defined by the translation stage. Fitting this hyperbolic function to the time points (y) at which the

maximum amplitude of the time signals was recorded results in a precise measurement of the fit parameters, namely the center along the y-axis (y_0), the z position of the suture (z_0) and the speed of sound (c). With this information the angle between the cylindrical wave and the transducer is then calculated using simple trigonometry as

$$\varphi = \tan^{-1} \frac{y - y_0}{z_0} \tag{2.2.2}$$

It is evident from Eq. 2.2.2 as well as from Fig. 2.1 that the maximum angle of incidence that can be measured is limited by the translation range along y as well as the distance between transducer and source along the z axis. For the given setup, angles between $\pm 60°$ were measured. Following this fitting step, the precise position of the suture is known and can be extrapolated for all transducer positions (i.e. angles).

An additional factor to be taken into account is the amplitude of cylindrical waves which decays by a factor of $1/\sqrt{r}$, r being the distance from the source. Based on the previously described fitting procedure, the distance between the detector position and the suture is simply calculated as $r = \sqrt{(y - y_0)^2 + z_0^2}$, which is then used to correct for the reduction in the measured signal amplitudes due to the cylindrical wave propagation. After applying the correction, the signal amplitudes for a given angel $I(\varphi)$ can be subsequently retrieved from the measured time signals, allowing for extracting the detector's directivity in dB via

$$D(\varphi) = -20 \log_{10}\left(\frac{I_{max}}{I(\varphi)}\right) = -20 \log_{10}\left(\frac{I_{\varphi=0}}{I(\varphi)}\right) \tag{2.2.3}$$

where $I_{max} = I_{\varphi=0}$ is the maximum signal amplitude measured at normal incidence. Finally, the frequency dependent directivity was calculated by Fourier transforming the signals recorded from the suture.

2.2.4. Image Reconstruction

To demonstrate the effect of the detector's directivity on the resulting OA image quality, a k-space reconstruction algorithm was used to reconstruct images of the suture phantom with both PZT and cMUT transducers [3]. We further imaged a phantom consisting of an

absorbing tube having an inner diameter of 800 μm, which was filled with highly absorbing India ink solution. For the imaging purposes, the tomographic data collection was performed by recording the generated optoacoustic responses at discrete transducer positions along the y-axis, which were then used to calculate the initial acoustic pressure distribution generated by the laser light being absorbed in the suture.

2.3. Results

2.3.1. Source Directivity Measurements

Figure 2.2 presents results from the source characterization measurements. Figure 2.2a) displays the spectrum of the generated optoacoustic response captured by the calibrated 1 mm needle hydrophone with the corresponding waveform shown in the inset. The spectrum clearly demonstrates the broadband nature of the generated signal, with a $-6\,$dB bandwidth of more than 8 MHz and a central frequency of 5.5 Mhz. This is in good agreement with the simulated values for a line emitter with a diameter of 100 μm [3]. In principle, given the 10 ns laser pulse duration, it would be possible to excite broadband OA signals for sutures of diameters as small as 25 μm, resulting in an even higher central frequency and bandwidth. However, the spectrum generated by the 100 μm suture is sufficient for the given frequency response of the tested transducers while thinner sutures and larger bandwidth would also lead to smaller signal amplitudes and increased noise in the signals.

Figure 2.2b) depicts the sinogram of the optoacoustic responses measured with the 75 μm needle hydrophone over a scan range of approximately 30 mm. Due to the small active area of the hydrophone, it is sensitive to signals recorded over a broad range of angles. This is clearly visible in Fig. 2.2c), where its directivity is plotted according to Eq. 2.2.3. The measured hydrophone amplitudes (green solid line) show a decrease of the signal amplitude of less than $6\,$dB over the measured angular range of $\pm 40°$, which is in good agreement with the previously reported values [31]. The dashed line in Fig. 2.2c) shows the slight influence of the amplitude correction due to the $1/\sqrt{r}$ signal drop of the cylindrical wave.
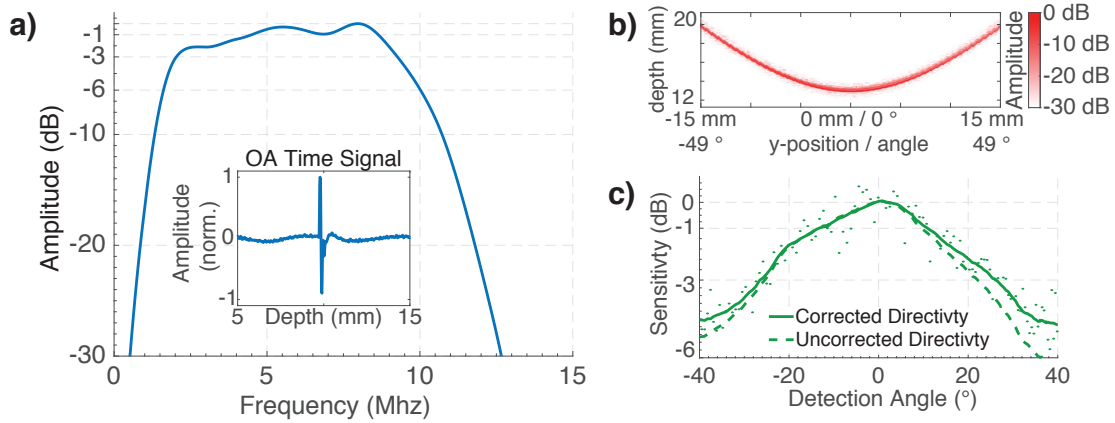
Figure 2.2.: Overview of the OA source characterization. (a) Spectrum of the generated OA response with the corresponding waveform shown in the inset. (b) Sinogram of the OA responses measured with a 75 µm needle hydrophone, showcasing signals recorded over a broad range of angles. (c) Sensitivity of the 75 µm hydrophone as a function of the angle. (a-c) Clearly demonstrates the broadband and omnidirectional nature of the OA signals emitted from the absorbing suture.
Reproduced with permission from [1]. © SPIE.

2.3.2. PZT and cMUT Transducer Directivity

The results of the amplitude-based directivity measurements are shown in Fig. 2.3 for both the PZT transducer (green) and the cMUT transducer (orange). Figure 2.3a) compares the absolute sensitivities of both transducers based on their signal-to-noise ratio (SNR), calculated as the ratio of the signal variance to the variance of the noise for each incidence angle:

$$SNR\left(\varphi\right) = \frac{\sigma_{sig}\left(\varphi\right)}{\sigma_{noise}\left(\varphi\right)} \tag{2.3.1}$$

For small incidence angles up to $\pm 20°$, the PZT transducer shows a better overall sensitivity compared to the cMUT transducer. The PZT has a 7.8 dB sensitivity advantage at normal incidence with an SNR of 266 (48.5 dB) versus 108 (40.7 dB) for the cMUT. However, for incidence angles larger than $\pm 20°$ the cMUT transducer is still sensitive and shows a much more gradual decrease of its sensitivity with increasing angles. In Fig. 2.3b) we calculated the directivities according to Eq. 2.2.3 by further correcting for the $1/\sqrt{r}$ signal decrease due to the cylindrical wave propagation and normalizing to the respective maximum values. Despite

the equal element pitch and size of the two transducers, the cMUT's broader acceptance angle is readily evident since its sensitivity only drops to 50% ($-6\,$dB) at an incidence angle of $\pm18°$, to 30% ($-10\,$dB) at $\pm25°$and 10% ($-20\,$dB) at $\pm50°$. In contrast, PZT exhibits significantly higher directivity with sensitivity decreasing to 50% ($-6\,$dB) at an incidence angle of $\pm12°$, to 30% ($-10\,$dB) at $\pm16°$, nearing the noise levels at $\pm35°$.
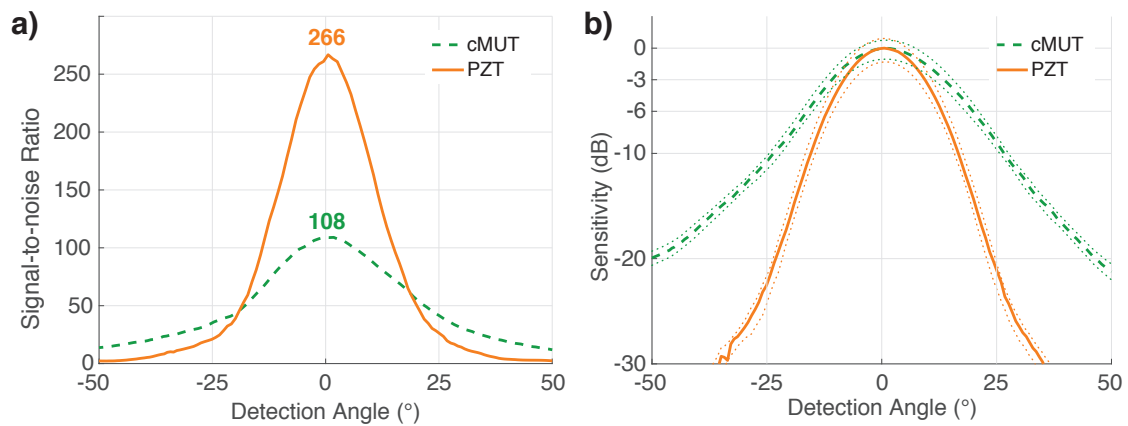
Figure 2.3.: Amplitude based directivity comparison of the cMUT (green) and PZT transducers (orange). (a) Signal-to-noise ratio as a function of the incidence angle for both transducers. (b) Normalized sensitivity plots, showing a strongly favorable sensitivity of the cMUT transducer for larger angles. Dots represent the maximum amplitude values for a given angle, solid lines represent the smoothed mean and dashed lines show the confidence interval with $+/-$ one standard deviation. Reproduced with permission from [1]. © SPIE.

The spectral sensitivity analysis shown in Fig. 2.4 makes an even stronger case for the superior angular sensitivity performance of cMUT. Figure 2.4a) and 2.4b) display the spectral sensitivity of the transducers as a function of the angle, essentially creating a sensitivity map of the transducer that simplifies the sensitivity comparison. It is evident from the sensitivity maps that the cMUT transducer shows a much broader angular sensitivity, in particular in the frequency range between 2 MHz and 6 MHz.

For a better quantitative comparison, we further plotted the frequency dependence of the sensitivity for both transducers at different incidence angles, as shown in Fig. 2.4c) and 2.4d). As can be seen in Fig. 2.4c), the PZT transducer only exhibits broadband behavior at angles close to normal incidence (blue solid line), in which case the $-6\,$dB bandwidth measures almost 10 MHz at a central frequency of 5 MHz. For incidence angles of $\pm20°$,

PZT's sensitivity drops by 15 dB (red solid line) while it reaches the noise floor at $\pm 40°$ angles (3% remaining sensitivity at the central frequency). This strong sensitivity drop can also be observed in Fig. 2.4e) where the directivity of the PZT transducer is plotted for discrete frequencies of 3, 5 and 8 MHz (blue, red and yellow curves, respectively). Figure 2.4e) closely resembles the amplitude-based PZT directivity plot shown in Fig. 2.3a) (orange line), with a 30 dB decrease in sensitivity at an angle of $\pm 40°$.

The corresponding frequency dependent sensitivity of the cMUT transducer (Fig.2.4d) and 2.4f)) does not exhibit such a strong decline in its broadband detection response over a large range of incidence angles. At normal incidence (Fig. 2.4d), blue solid line) the cMUT has a similar $-6\,\mathrm{dB}$ bandwidth of 10 MHz, yet a slightly higher sensitivity towards the higher frequencies. For incidence angles around $\pm 20°$ the cMUT sensitivity is only decreased by 6 dB (red solid line). For angles of $\pm 40°$, its frequency response is considerably shifted toward the lower frequencies but the overall sensitivity drop is still less than 20 dB (yellow solid line). The same behavior can again be observed in Fig. 2.4f), showcasing the cMUTs broad angular sensitivity with a sensitivity decrease of 15 dB at $\pm 50°$ for both 3 and 5 MHz (blue and red solid lines respectively) and with a sensitivity decrease of 30 dB at $\pm 50°$ even at 8 MHz (yellow solid line).

Since both PZT and cMUT have a similar element size and were measured using the same acquisition system with identical connectors, cables and sampling electronics, the striking difference in the measured directivity may only result from the basic physical differences between the two technologies. In standard piezoelectric transducers, the active elements are bulk resonators. The incident US wave then couples to a standing wave within the element but is largely reflected due to the big impedance mismatch between water and the piezoelectric material. An acoustic matching layer is needed to facilitate acoustic coupling, which is the most probable cause of the observed poor angular sensitivity [19]. On the other hand, the thin membranes used by cMUTs do not require matching layers, thus allowing for a broader acceptance angle [16].
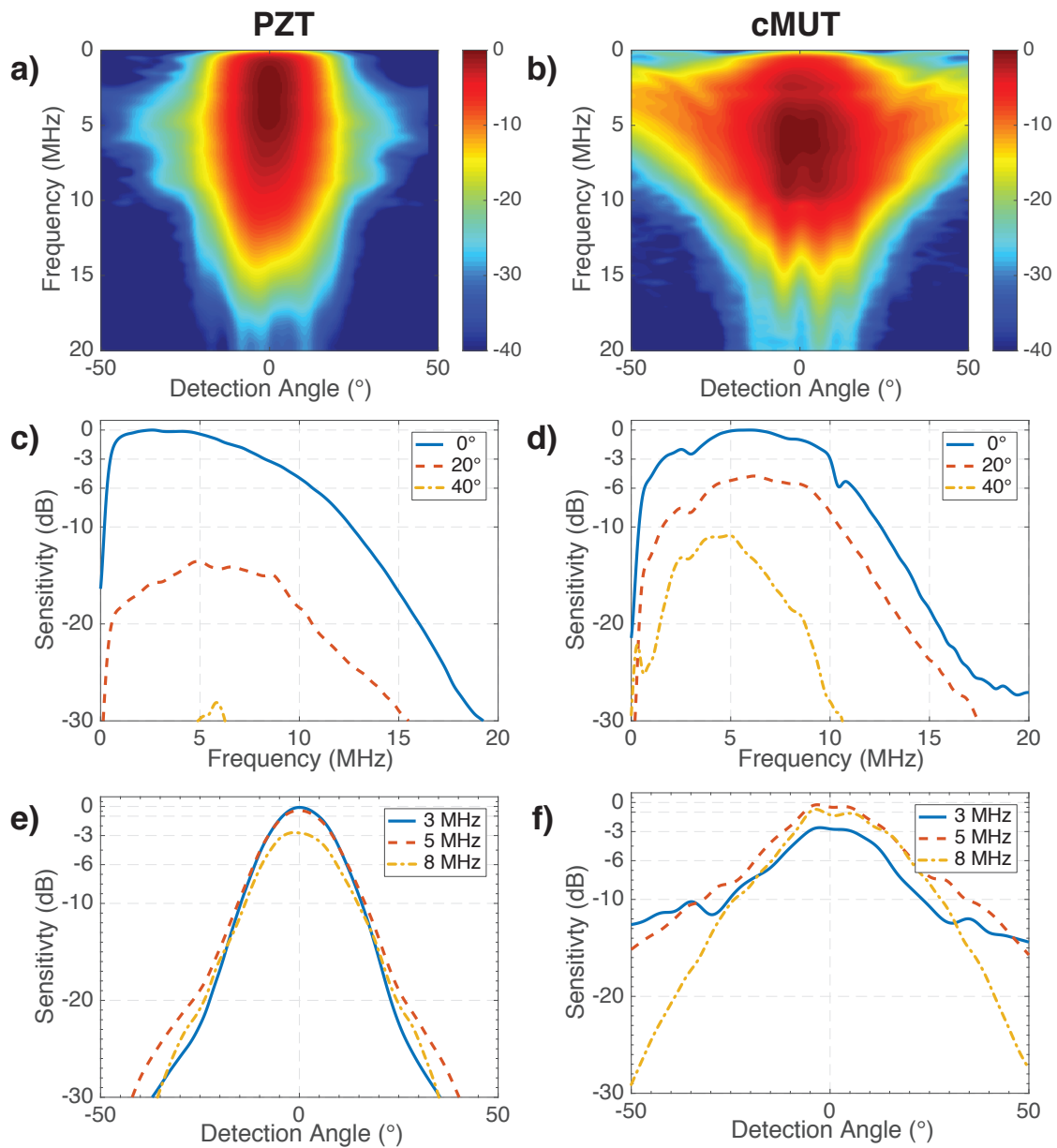
Figure 2.4.: Spectral sensitivity comparison of the cMUT (left) and PZT transducers (right), showing a strongly favorable sensitivity of the cMUT transducer for larger angles over a broad frequency range. Figures a) and b) display the spectral sensitivity map of the transducers as a function of both incidence angle and frequency. The spectral sensitivity for discrete incidence angles (0°, 20°, and 40°) is shown in c) and d) for the PZT and the cMUT respectively. Figures e) and f) present the sensitivity spectra for discrete frequencies of 3, 5 and 8 MHz (blue, red and yellow curves, respectively). A strong decrease in sensitivity with increasing angle can be observed for the PZT transducer shown in a), c) and e) while the cMUT transducer in b), d) and f) does not exhibit such a strong decline in its broadband detection response over a large range of incidence angles.
Reproduced with permission from [1]. © SPIE.

2.3.3. Optoacoustic Imaging Results

Figures 2.5a) and 2.5b) display the reconstructed OA images of the ink tube phantom for the PZT and cMUT transducers, respectively. Both transducers are able to properly reconstruct the tube features in the direction facing the detector. However, the PZT-derived image exhibits stronger limited-view artifacts with the side walls of the tube completely lacking in the image. Figures 2.5c) and 2.5d) further show the images of the absorbing suture that were again reconstructed with both transducers. Ideally, the reconstructed image would represent a 100 µm diameter circle. However, both the axial and lateral resolution of the reconstruction are limited by acoustic diffraction constraints as well as the particular tomographic scanning geometry. In principle, the depth resolution δ_z is established by the transducer's bandwidth and can be approximated as $\delta_z \approx 0.8c/BW$, where c is the speed of sound and BW is the bandwidth of the transducer[40]. Given their 10 MHz bandwidth and a speed of sound in water of 1500 m/s, the theoretical axial resolution of both transducers is $\delta_z \approx 120$ µm. The lateral resolution, i.e. the resolution in the x-y plane, is however dependent not only on the available bandwidth but also on the element size or pitch d via $\delta_y \approx \sqrt{d^2 + (c/BW)^2}$ [41]. In the present case, this corresponds to $\delta_y \approx 250$ µm given the element width of 200 µm.

The axial size of the reconstructed suture for both PZT and cMUT is around 160 µm as shown in Fig. 2.5e). After deconvolving the suture's diameter, this translates into an axial resolution of approximately 120 µm, as expected from the theory. This is not surprising given the almost identical bandwidth of the two transducers. The reconstructed suture has, however, a very different size in the lateral dimension, as shown in Fig. 5f. While the cMUT-rendered reconstruction leads to a lateral width of about 300 µm, the corresponding PZT image results in a lateral width of more than 500 µm, evincing of the limited-view artifacts produced by the highly directive piezoelectric elements. While in the case of cMUT signals recorded from all the scanning positions have contributed to the reconstruction, the PZT was only able to record signals when detector's y-position was very close to the suture, i.e. for small incidence angles.

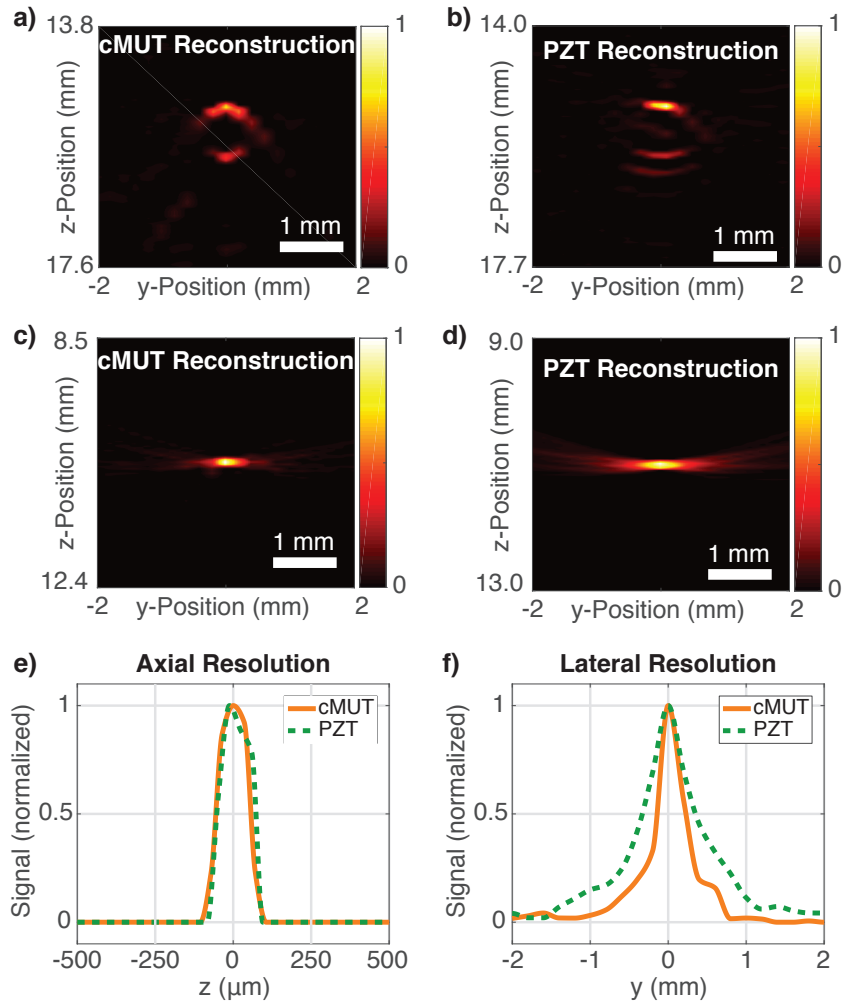Figure 2.5.: Comparison of the OA images acquired with the cMUT and PZT, showing significantly stronger limited-view artifacts for the latter. In (a) and (b) images of a 800 μm diameter tube filled with India ink solution are shown. In (c) and (d) images of a 100 μm absorbing suture are shown. Figures e) and f) display the axial and lateral resolution of the reconstructed suture images in c) and d).

2.4. Conclusions

Capacitive micromachined ultrasonic transducers (cMUT) have recently evolved as a promising alternative to the well-established piezoelectric detection technology in the field of ultrasound imaging. In the context of optoacoustic imaging applications, spatial and frequency response characteristics of ultrasound transducers have a major impact on the imaging performance. While the feasibility of optoacoustic imaging with cMUT transducers has been demonstrated recently, broadband directivity patterns of typical cMUTs have not been systematically studied.

Here we presented a universal method for characterizing the broadband directivity of ultrasound transducers used in optoacoustic imaging systems. Our technique allows for the transducer frequency response to be investigated both under normal incidence as well as for arbitrary angles of incidence as large as $\pm 60°$. The method can be adapted to the desired frequency range by changing the size of the absorbing source, thereby changing the frequency content of the emitted OA signals. No additional ultrasound emitter is required, resulting in a fast and simple characterization method that does not require complicated alignments and precise positioning hardware. The data processing is simple, robust and only requires a sufficient signal-to-noise ratio in order to localize and analyze the recorded signals. The proposed method can therefore be used to characterize the directivity of an arbitrary number of transducer elements simultaneously using any existing OA imaging system. In the future, the method can be extended to enable characterization of matrix array transducers by replacing the OA line source with a point absorbing source, e.g. a microsphere, while also translating the matrix array being tested in both lateral dimensions.

The validity of the proposed methodology has been demonstrated with calibrated hydrophone measurements, which were used to calibrate the broadband omni-directional optoacoustic sources used in this study. We subsequently used the newly developed methodology to compare the characteristics of a typical piezo-electric PZT transducer to a cMUT transducer with similar geometrical and frequency response parameters. In our experiments, the PZT transducer has attained a 7.8 dB higher sensitivity at normal incidence as compared with the cMUT. Note that the sensitivity performance can be significantly optimized when

implementing the front-end electronics close to the detector, which was not done here. It was in fact previously demonstrated that cMUT transducers may attain a comparative or better sensitivity when the pre-amplification is implemented within the cMUT chip [13–15]. Most importantly, the cMUT detector prototype tested here exhibited a significantly larger acceptance angle compared to the PZT while having comparable detection bandwidth at normal incidence. This suggests the cMUT technology as a more favorable candidate for use in optoacoustic imaging applications owing to its advantageous broadband angular sensitivity patterns that results in fewer reconstruction artifacts and better spatial resolution of the images.

Acknowledgements

References

[1] **Johannes Rebling** et al. „Optoacoustic characterization of broadband directivity patterns of capacitive micromachined ultrasonic transducers". In: *Journal of biomedical optics* 22.4 (Nov. 2016), p. 041005.
DOI: 10.1117/1.jbo.22.4.041005.

[2] O. Warshavski et al. „Experimental evaluation of cMUT and PZT transducers in receive only mode for photoacoustic imaging". (Conference Presentation and Proceedings Paper). In: *Photons Plus Ultrasound: Imaging and Sensing 2016*. Ed. by Alexander A. Oraevsky and Lihong V. Wang. Vol. 9708. International Society for Optics and Photonics. SPIE, Mar. 2016, p. 970830.
DOI: 10.1117/12.2211799.

[3] B. E. Treeby and B. T. Cox. „k-Wave: MATLAB toolbox for the simulation and reconstruction of photoacoustic wave fields". In: *Journal of Biomedial Optics* 15.2 (2010), p. 021314.
DOI: 10.1117/1.3360308.

[4] **Johannes Rebling** et al. „Broadband optoacoustic characterization of cMUT and PZT transducer directivity in receive mode". (Conference Poster and Proceedings Paper). In: *Medical Imaging 2017: Ultrasonic Imaging and Tomography*. Vol. 10139. International Society for Optics and Photonics. International Society for Optics and Photonics, Mar. 2017, 101391K.
DOI: 10.1117/12.2253850.

[5] A. Rosenthal, V. Ntziachristos, and D. Razansky. „Acoustic Inversion in Optoacoustic Tomography: A Review". In: *Curr Med Imaging Rev* 9.4 (2013), pp. 318–336.
DOI: 10.2174/15734056113096660006.

[6] J. Yao and L. V. Wang. „Sensitivity of photoacoustic microscopy". In: *Photoacoustics* 2.2 (2014), pp. 87–101.
DOI: 10.1016/j.pacs.2014.04.002.

[7] Deán-Ben X. L., A. Ozbek, and D. Razansky. „Volumetric real-time tracking of peripheral human vasculature with GPU-accelerated three-dimensional optoacoustic tomography". In: *IEEE Trans Med Imaging* 32.11 (2013), pp. 2050–5.
DOI: 10.1109/TMI.2013.2272079.

[8] C. Lutzweiler and D. Razansky. „Optoacoustic imaging and tomography: reconstruction approaches and outstanding challenges in image performance and quantification". In: *Sensors (Basel)* 13.6 (2013), pp. 7345–84.
DOI: 10.3390/s130607345.

[9] V. Ntziachristos and D. Razansky. „Molecular imaging by means of multispectral optoacoustic tomography (MSOT)". In: *Chemical Reviews* 110.5 (2010), pp. 2783–94.
DOI: 10.1021/cr9002566.

[10] M. Roumeliotis et al. „Development and characterization of an omni-directional pho-toacoustic point source for calibration of a staring 3D photoacoustic imaging sys-tem". In: *Development and characterization of an omni-directional photoacoustic point source for calibration of a staring 3D photoacoustic imaging system* (2009). DOI: `10.1364/oe.17.015228`.

[11] Y. Xu et al. „Reconstructions in limited-view thermoacoustic tomography". In: *Medical Physics* 31.4 (2004), pp. 724–33. DOI: `10.1118/1.1644531`.

[12] A. Buehler et al. „Model-based optoacoustic inversions with incomplete projection data". In: *Medical Physics* 38.3 (2011), pp. 1694–704. DOI: `10.1118/1.3556916`.

[13] I. O. Wygant et al. „An integrated circuit with transmit beamforming flip-chip bonded to a 2-D CMUT array for 3-D ultrasound imaging". In: *IEEE Trans Ultrason Ferro-electr Freq Control* 56.10 (2009), pp. 2145–56. DOI: `10.1109/TUFFC.2009.1297`.

[14] G. Gurun, P. Hasler, and F. L. Degertekin. „Front-end receiver electronics for high-frequency monolithic CMUT-on-CMOS imaging arrays". In: *IEEE Transactions on Ultrasonics, Ferroelectrics and Frequency Control* 58.8 (Aug. 2011), pp. 1658–1668. DOI: `10.1109/tuffc.2011.1993`.

[15] A. S. Savoia, G. Calianov, and M. Pappalardo. „A CMUT probe for medical ultra-sonography: from microfabrication to system integration". In: *IEEE Trans Ultrason Ferroelectr Freq Control* 59.6 (2012), pp. 1127–38. DOI: `10.1109/TUFFC.2012.2303`.

[16] P. C. Eccardt and K. Niederer. „Micromachined ultrasound transducers with improved coupling factors from a CMOS compatible process". In: *Ultrasonics* 38.1-8 (2000), pp. 774–80. DOI: `10.1016/s0041-624x(99)00085-2`.

[17] M. Legros et al. „Piezocomposite and CMUT arrays assessment through in vitro imaging performances". In: *Ultrasonics Symposium, 2008. IUS 2008. IEEE* (2009), pp. 1142–1145.
DOI: 10.1109/ULTSYM.2008.0275.

[18] G. Caliano et al. „Design, fabrication and characterization of a capacitive micromachined ultrasonic probe for medical imaging". In: *IEEE Trans Ultrason Ferroelectr Freq Control* 52.12 (2005), pp. 2259–69.
DOI: 10.1109/TUFFC.2005.1563268.

[19] S. Michau, P. Mauchamp, and R. Dufait. „Piezocomposite 30MHz linear array for medical imaging: design challenges and performances evaluation of a 128 elements array". In: *2004 IEEE Ultrasonics Symposium* 2 (2004).
DOI: 10.1109/ULTSYM.2004.1417880.

[20] S. Vaithilingam et al. „Three-dimensional photoacoustic imaging using a two-dimensional CMUT array". In: *IEEE Trans Ultrason Ferroelectr Freq Control* 56.11 (2009), pp. 2411–9.
DOI: 10.1109/TUFFc.2009.1329.

[21] S. R. Kothapalli et al. „Deep tissue photoacoustic imaging using a miniaturized 2-D capacitive micromachined ultrasonic transducer array". In: *IEEE Transactions on Biomedical Engineering* 59.5 (2012), pp. 1199–204.
DOI: 10.1109/TBME.2012.2183593.

[22] A. Nikoozadeh et al. „Photoacoustic imaging using a 9F microLinear CMUT ICE catheter". In: *Photoacoustic imaging using a 9F microLinear CMUT ICE catheter* (2012), pp. 24–27.
DOI: 10.1109/ULTSYM.2012.0007.

[23] S. Vaithilingam, T. J. Ma, and Y. Furukawa. „Investigating large 2D arrays for photoacoustic and acoustic imaging using CMUT technology". In: *Investigating large 2D arrays for photoacoustic and acoustic imaging using CMUT technology* (2008).
DOI: 10.1109/ultsym.2008.0299.

[24] W. R. MacLean. „Absolute Measurement of Sound Without a Primary Standard".
      In: *The Journal of the Acoustical Society of America* 12.1 (1940), pp. 140–146.
      DOI: 10.1121/1.1916085.

[25] Paul Ebaugh and Roland E. Mueser. „The Practical Application of the Reciprocity
      Theorem in the Calibration of Underwater Sound Transducers". In: *The Journal of
      the Acoustical Society of America* 19.4 (1947), pp. 695–700.
      DOI: 10.1121/1.1916540.

[26] K. Brendel and G. Ludwig. „Calibration of ultrasonic standard probe transducers".
      In: *Calibration of ultrasonic standard probe transducers* (1976).

[27] J. P. Monchalin. „Optical detection of ultrasound". In: *IEEE Trans Ultrason Ferro-
      electr Freq Control* 33.5 (1986), pp. 485–99.
      DOI: 10.1109/t-uffc.1986.26860.

[28] D. R. Bacon. „Primary calibration of ultrasonic hydrophone using optical interferom-
      etry". In: *Primary calibration of ultrasonic hydrophone using optical interferometry*
      (1988).
      DOI: 10.1109/58.4165.

[29] J. C. Baboux and H. Djelouah. „Interferometric measurements of transient ultrasonic
      fields. application to hydrophone calibration". In: *Interferometric measurements of
      transient ultrasonic fields. application to hydrophone calibration* (1988).
      DOI: 10.1109/ULTSYM.1988.49499.

[30] H. Djelouah, J. C. Baboux, and M. Perdrix. „Pulsed calibration technique of minia-
      ture ultrasonic receivers using a wideband laser interferometer". In: *Ultrasonics* 27.2
      (1989), pp. 80–85.
      DOI: 10.1016/0041-624x(89)90017-6.

[31] P. C. Beard, A. M. Hurrell, and T. N. Mills. „Characterization of a polymer film optical
      fiber hydrophone for use in the range 1 to 20 MHz: a comparison with PVDF needle
      and membrane hydrophones". In: *IEEE Trans Ultrason Ferroelectr Freq Control* 47.1

(2000), pp. 256–64.

DOI: 10.1109/58.818769.

[32]   R. A. Smith and D. R. Bacon. „A multiple-frequency hydrophone calibration technique". In: *Journal of the Acoustical Society of America* 87.5 (1990), pp. 2231–43.

DOI: 10.1121/1.399191.

[33]   D. R. Bacon. „Finite amplitude distortion of the pulsed fields used in diagnostic ultrasound". In: *Finite amplitude distortion of the pulsed fields used in diagnostic ultrasound* (1984).

DOI: 10.1016/0301-5629(84)90217-5.

[34]   A. Rosenthal, V. Ntziachristos, and D. Razansky. „Optoacoustic methods for frequency calibration of ultrasonic sensors". In: *IEEE Trans Ultrason Ferroelectr Freq Control* 58.2 (2011), pp. 316–26.

DOI: 10.1109/TUFFC.2011.1809.

[35]   D. Razansky, J. Baeten, and V. Ntziachristos. „Sensitivity of molecular target detection by multispectral optoacoustic tomography (MSOT)". In: *Medical Physics* 36.3 (2009), pp. 939–45.

DOI: 10.1118/1.3077120.

[36]   Alexander A. Oraevsky and Alexander A. Karabutov. „Ultimate sensitivity of time-resolved optoacoustic detection". In: *SPIE 3916, Biomedical Optoacoustics* (2000).

DOI: 10.1117/12.386326.

[37]   R. O. Esenaliev, A. A. Karabutov, and A. A. Oraevsky. „Sensitivity of laser optoacoustic imaging in detection of small deeply embedded tumors". In: *IEEE Journal of Selected Topics in Quantum Electronics* 5.4 (1999), pp. 981–988.

DOI: 10.1109/2944.796320.

[38]   William M. Haynes. „CRC handbook of chemistry and physics". In: *CRC press* (2014).

DOI: 10.1088/0031-9112/13/1/015.

[39] B. Belgacem et al. „Optimization of the fabrication of sealed capacitive transducers using surface micromachining". In: *Journal of Micromechanics and Microengineering* 14.2 (2004), pp. 299–304.
      DOI: 10.1088/0960-1317/14/2/019.

[40] Lihong V. Wang. *Photoacoustic Imaging and Spectroscopy*. CRC Press, Mar. 2009. ISBN: 9781420059915.

[41] J. Xia, J. Yao, and L. V. Wang. „Photoacoustic tomography: principles and advances". In: *Electromagn Waves (Camb)* 147 (2014), pp. 1–22.

3. Integrated catheter for simultaneous radio frequency ablation and optoacoustic monitoring of lesion progression

Johannes Rebling[†], Francisco Javier Oyaga Landa[†], Xosé Luís Deán-Ben, Alexandre Douplik, and Daniel Razansky. „Integrated catheter for simultaneous radio frequency ablation and optoacoustic monitoring of lesion progression". In: *Optics letters* 43.8 (Apr. 2018), pp. 1886–1889.

Summary and Author Contribution

Optoacoustic tomography (OAT) is a powerful tool for the real-time monitoring of biological processes due to its ability to form volumetric images at high frame rates (see Section 1.3.1). Utilizing this capability, our group has successfully applied OAT for monitoring of electro-surgery, i.e. the use of radiofrequency (RF) current for tissue ablation [2]. While showing promising results, the presented approach was not suitable for clinical application due to the geometry of light delivery, ablation electrode placement and ultrasound (US) detection. This manuscript describes a novel proof-of-concept catheter for simultaneous radiofrequency ablation and optoacoustic monitoring of lesion formation in. The catheter delivers electric current and optoacoustic excitation light using copper-coated multimode light-guides. The presented manuscript describes the manufacturing, catheter characterization and showcases the ablation-monitoring capabilities.

My contribution to the presented manuscript where the following:

Conceptualization During a visit, Prof. Douplik from the Ryerson University in Canada, presented prototype copper-coated multi-mode fibers (MMFs) they were co-developing in his laboratory. I had previously gained experience in manufacturing custom-made MMF-bundles in-house and when presented with the copper coated fibers, Prof. Razansky and I realized the potential to utilized them to create a bundle capable of delivering both light and ablation current to the targeted tissue.

Methodology Following first successful tests and improvements on fiber diameters, assembly and polishing I assembled approximately 100 fibers to form the bundle used in the study with the help of Francisco Javier Oyaga Landa. I connectorized the bundle to allow electrical and optical coupling, as described in the manuscript. The connectorized and encapsulated bundle thus formed a proof-of-concept ablation catheter, capable of delivering optoacoustic (OA) excitation in the fiber core while conduction ablation energy in the thin copper layer surrounding the individual MMF. Ablation characterization of the catheter was performed by Francisco Javier Oyaga Landa with my help. OA characterization and ablation with simultaneous OAT imaging was carried out by Francisco Javier Oyaga Landa and Xosé Luís Deán-Ben.

Writing and Revisions I prepared the initial manuscript with significant contributions from Daniel Razansky and Xosé Luís Deán-Ben. I created all figures including the shown schematics. OAT images and traces are based on OAT reconstructions performed by Francisco Javier Oyaga Landa and with critical suggestions from all authors. Francisco Javier Oyaga Landa and I performed additional experiments, I amended the manuscript and modified the figures as per reviewer request and with significant contributions from Daniel Razansky and Xosé Luís Deán-Ben.

This study was presented at the *SPIE Photonics West BIOS 2018* conference and was featured in the Optical Society of America (OSA) "Spotlight on Optics" in April 2018 [3, 4].

Abstract

Radiofrequency catheter ablation is commonly used to eliminate dysfunctional cardiac tissue by heating via an alternating current. Clinical outcomes are highly dependent on careful anatomical guidance, electrophysiological mapping, as well as careful radiofrequency power titration during the procedure. Yet, current treatments rely mainly on the expertise of the surgeon to assess lesion formation, causing large variabilities in the success rate. We present an integrated catheter design suitable for simultaneous radiofrequency ablation and real-time optoacoustic monitoring of the forming lesion. The catheter design utilizes copper-coated multimode light-guides capable of delivering both ablation current and near-infrared pulsed-laser illumination to the target tissue. The generated optoacoustic responses were used to visualize the ablation lesion formation in *ex vivo* bovine heart specimen in 3D. The presented catheter design enables the monitoring of ablation lesions with high spatio-temporal resolution while the overall therapy-monitoring approach remains compatible with commercially available catheter designs.

Main Manuscript

Radiofrequency catheter ablation (RFCA) is used for coagulation and destruction of dysfunctional tissues in the fields of oncology [5], cardiology [6], dermatology [7], and vascular diseases [8]. One common application in cardiology is the elimination of abnormal electrical pathways responsible for cardiac arrhythmias [6], particularly those shown to be resistant to drug therapy [9]. Much like other thermal ablation procedures, RFCA results in localized coagulation and desiccation of the target tissue while avoiding uncontrolled damage to neighboring structures. The ablation procedure is generally guided by electrophysiological and anatomic mapping as well as careful radiofrequency RF power titration [10]. The size of the induced lesion is mainly determined by the extent and duration of the heat affected area. Hence, real-time treatment monitoring is essential to optimize the outcome of the intervention. The ablation process is usually monitored via simple temperature or impedance measurements at the ablation tip [11, 12]. However, heat diffusion and the use of irrigated

ablation tips can substantially affect the size and shape of the heated area, resulting in failed treatments [13]. To this end, several imaging techniques have been proposed for ablation monitoring. For example, intravascular ultrasound (IVUS) and magnetic resonance imaging (MRI) allowed for a more precise placement and navigation of the ablation catheter and visualization of the RFCA-induced morphological tissue alterations [14]. Transformations of the tissue composition in coagulated or desiccated areas result in light scattering and absorption changes detectable via optical methods, such as spectroscopy or optical coherence tomography (OCT) [15]. Infrared thermal imaging furthermore allows the quantification of tissue temperature with high-resolution, but is restricted to superficial tissues [16]. US, x-ray computed tomography (CT) or MRI images were shown sensitive to temperature variations in the tissue, however real-time mapping of lesion formation is impeded with these techniques due to either limited temporal resolution or low contrast [17].

OA imaging has been suggested for ablation monitoring as early as 1993 [18], chiefly owing to its high sensitivity to changes in optical properties resulting from chemical transformations in ablated tissues [19] and to temperature variations [20]. OA has been used for temperature monitoring in forming lesions [21] and recently adopted for volumetric tomographic ablation monitoring in real time [2]. Volumetric OA tomography has also been shown to clearly discern vascular and organ morphology as well as extrinsically labeled structures *in vivo* [22], making it highly suitable for precise anatomical navigation. The high imaging speed of state-of-the-art OA tomography is efficient in capturing the dynamics of RFCA treatments with sub-second temporal resolution in two [19] and three dimensions [2]. However, in previous studies the excitation light was delivered into the ablated area through thick layers of turbid tissues, limiting applicability in realistic clinical scenarios involving monitoring of deep tissue lesions [23].

Herein, we present a conceptually different approach for simultaneous radiofrequency ablation and optoacoustic monitoring (RAOM) of the lesion formation. It combines the delivery of both electrical current and pulsed light within a single catheter (3.1) while detection of the generated OA responses is performed from outside the body using a spherical matrix array for optimal volumetric OA image formation. The integrated catheter consists of a bundle

of 96 copper-coated multimode fibers (3.1a). The excitation light and electrical current are coupled into the proximal end of the bundle (3.1b) and are delivered to the tissue at its distal end (3.1c). The individual, custom-made light-guides consist of step-index multi-mode optical fibers with a silica core and a fluorine-doped glass cladding, enabling efficient propagation of visible and near-infrared light with a transmission efficiency of approximately 30%. The fibers have a core diameter of 200 µm (220 µm including cladding) and a numerical aperture (NA) of 0.2. The light guides are further coated with a 25 µm thin copper film (3.1d). The copper coating was removed at the proximal end of the bundle in order to maximize light coupling efficiency. This was achieved by closely packing the fibers within a conventional optical fiber connector (inner diameter 2.5 mm, SMA905, Thorlabs, Newton, USA) and securing them using a high-temperature epoxy (353NDPK, Thorlabs, Newton, USA). After the epoxy was cured, the proximal end was polished to optical quality. 3.1b shows the facet of the polished proximal. A low-resistance electrical connection between the separate copper-coated light-guides was achieved using solder in the vicinity of the proximal end. Additionally, a copper cable was soldered to the same location, enabling the connection to the radiofrequency generator. The copper-coated light-guides align to each other in a nearly hexagonal pattern ensuring an even distribution of the ablation current at the distal tip. The bundle was embedded into a steel ferule with an outer diameter of 6 mm and an inner aperture of 4 mm using high temperature epoxy and polished to optical quality. The minimal short-term bending radius of the copper-coated fibers was experimentally found to be 2 mm, comparable to conventional 200 µm fibers, while the bending radius of the assembled bundle was less than 8 mm. 3.1c shows the polished facet of the distal end with and without light transmitted through the catheter. The assembled RAOM catheter (3.1d) was electrically insulated using PVC tubing (Tygon, Carl Roth GmbH, Karlsruhe, Germany), only exposing the ablation tip at the distal end. A schematic of the simultaneous RF ablation and OA signal detection experiment is shown in 3.1e. The ultrasound array consists of 256 detection elements distributed on a spherical cap with 90° apex angle (0.59π solid angle) and 4 cm radius. Its individual elements have a central frequency of 4 MHz and 100% detection bandwidth, resulting in nearly isotropic 3D imaging resolution of $\approx$200 µm

around the geometrical center of the sphere. OA signal excitation was achieved via an optical parametric oscillator (OPO)-based laser (Innolas Laser GmbH, Krailling, Germany) coupled into the proximal end of the RAOM catheter. The distal end of the catheter delivered short (<10 ns) laser pulses with ≈6 mJ energy and pulse repetition rate of 10 Hz, resulting in light fluence of ≈48 mJ/cm² at the fiber tip. The wavelength of the laser was tuned to 780 nm, corresponding to the highest lesion-specific OA contrast [2]. The 256 detection channels were simultaneously digitized at 40 mega-samples per second by a custom-made data acquisition system (Falkestein Mikrosysteme GmbH, Taufkirchen, Germany) triggered by the Q-switch output of the laser. The same trigger signal was used to switch off the RF current during the OA signal acquisition in order to avoid signal cross-talk. The acquired signals were deconvolved with the impulse response of the matrix array elements and band-pass filtered between 0.1 and 2 MHz to smoothen the images. The reconstructions were performed with a graphics-processing-unit-based three-dimensional back-projection algorithm [24, 25].

Performance of the RAOM catheter was first separately characterized in the OA imaging and RF ablation modes. For OA imaging, we used a two-layer agarose phantom (3.2a). The first layer mimicked strong tissue scattering and was used to quantify the OA signal levels generated by the catheter tip due to back-scattered light. It consisted of a 3 mm thick layer of agarose mixed with 1.2% (by volume) of Intralipid. The second 1.5 mm thick layer of the phantom mimicked tissue optical absorption of a=0.66cm^{-1} at 780nm [27] and comprised of agarose mixed with ink. The distal end of the catheter was positioned in direct contact with the scattering layer of the phantom and OA imaging was performed without RF ablation. 3.2b displays the side view of the recorded volumetric OA image where the absorbing layer is clearly visible at a depth of 3mm in the phantom (P). Part of the light emitted by the catheter is back-scattered towards the ablation tip where it is absorbed by both the copper surrounding the light guides as well as the steel ferule (see Fig. 1a). The signal generated at the catheter tip (C) is however much weaker in comparison to that generated by the tissue-mimicking absorbing layer. The catheter tip also acts as a partial acoustic reflector of the omnidirectional OA signals generated in the phantom. This results in shadow signals detected by the transducer (R). However, these artifacts do not
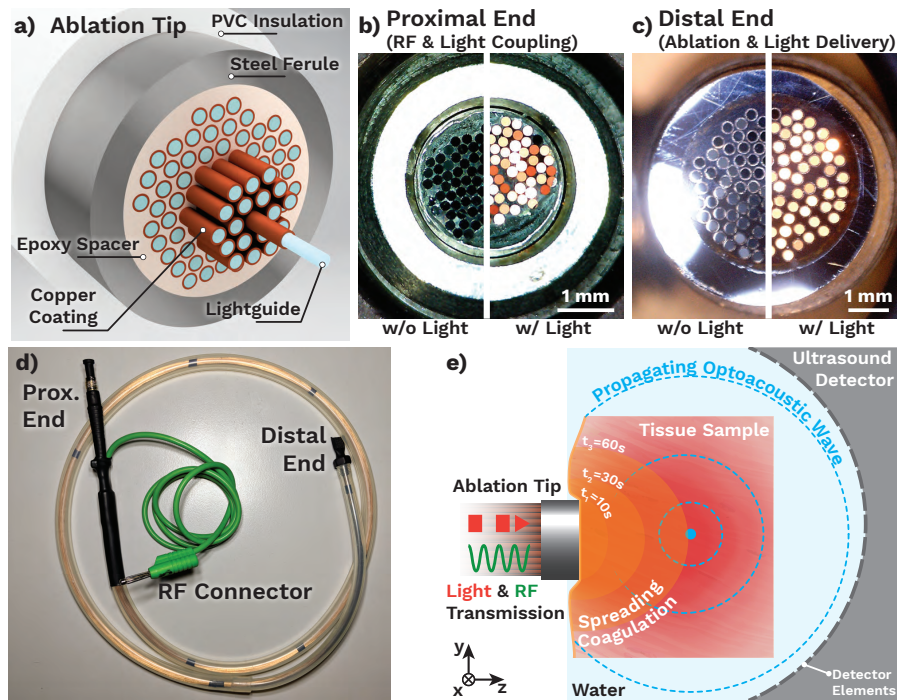
Figure 3.1.: Design and application of the combined radiofrequency ablation and optoacoustic monitoring (RAOM) catheter. (a) The catheter ablation tip, comprised of copper-coated light guides embedded in a steel ferule using high-temperature epoxy. (b) Proximal end-facet of the catheter, optimized for high light coupling efficiency. (c) Distal end-facet of the catheter, delivering both radiofrequency current and pulsed-light illumination. (d) Fully assembled bundle. (e) Layout of the combined RF ablation and OA monitoring experiment.

Reproduced with permission from [26]. © The Optical Society.

interfere with the signals originating from the region of interest and can easily be cropped. The top view of the volumetric OA image shown in 3.2c further illustrates the uniform illumination provided by the RAOM catheter. Ablation performance of the RAOM catheter was subsequently evaluated by generating lesions in a porcine heart tissue sample. The catheter was connected to a custom-build generator allowing precise control of the output RF power. The samples were immersed in phosphate-buffered saline (PBS, Sigma Aldrich, St. Louis, United States) and the ground-electrode with 20 cm^3 area was positioned under the tissue. The catheter delivered tone-bursts of electric current at 20 kHz carrier frequency with a duty-cycle of 3% (600 cycles in a burst, 10 Hz repetition frequency). On average, 9 W of electric power was delivered for 10 s, 20 s, 40 s and 60 s into the tissue samples. Photographs of the generated lesions are shown in 3.2d. The catheter formed a homogenous white coagulum having a typical pallor and a small depression due to desiccation without any visible charring. Longer ablation durations generated deeper lesions, reaching a maximal depth of $\approx$1 cm after 60 s. The tissue beyond the coagulation region appears unaffected in all four tissue samples. The uniform lesion shape indicates a homogenous current distribution due to the evenly distributed copper-coated light-guides.

The real-time ablation monitoring performance was then evaluated in a 4 cm thick porcine tissue sample, which was placed between the RAOM catheter and the surface of the spherical detection array. Ablation was carried out for 30 s and OA signals were acquired for 180 s to cover the cooling period. Light fluence decay was volumetrically corrected by dividing the reconstructed volumetric image with the solution of the light diffusion equation for a point source, i.e., a 3D exponential decay in the form of $(1/d)\exp(-\mu_{eff}d)$, where $\mu_{eff} = 3\ cm^{-1}$ is the effective attenuation coefficient and d is the distance in cm between the corrected voxel and the distal end of the fiber bundle. For distances d smaller than the radius of the ablation tip, the fluence was assumed to be constant. This particular correction function was applied as a purely qualitative measure aimed at achieving better contrast uniformity across the OA images.

3.3 displays OA images of the porcine tissue sample prior (3.3a), during (3.3b) and after (3.3c) the RF ablation procedure together with an OA signal time-trace of a coagulated
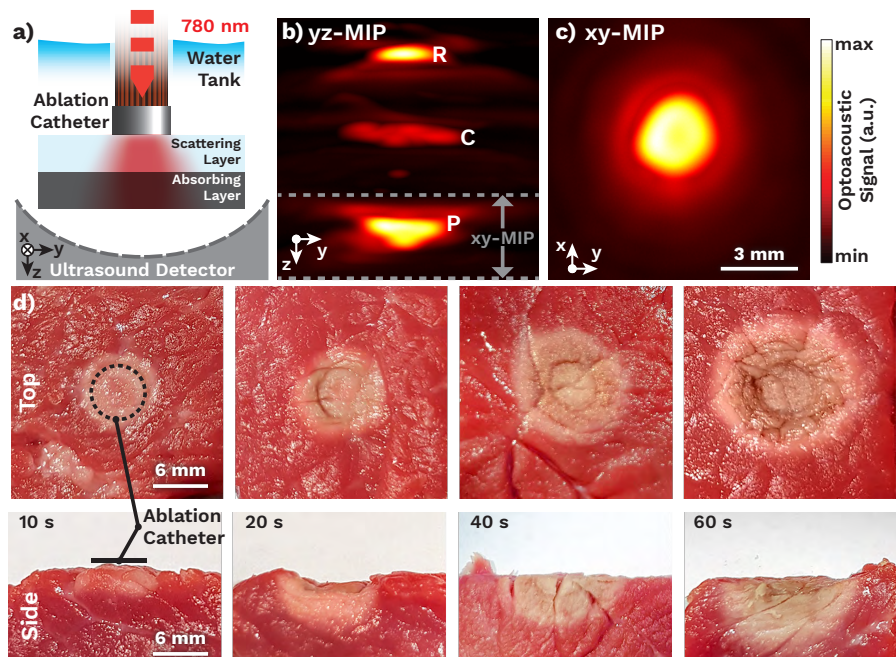
Figure 3.2.: Characterization of the RFOA catheter in standalone OA imaging and RF ablation modes. (a) Experimental arrangement for OA imaging with the catheter placed in direct contact with a scattering and absorbing phantom. (b) Reconstructed volumetric OA images of the phantom containing signals generated by the absorbing layer (P) and the catheter tip (C) as well as signal reflected by the catheter tip (R). Maximal intensity projection (MIP) along the x direction is shown. (c) The corresponding MIP image made along the depth (z) direction over the range indicated by the gray dashed lines in panel b. (e) Top- and side-view photographs of lesions generated in porcine heart tissue.
Reproduced with permission from [26]. © The Optical Society.

and a non-coagulated voxel (3.3d). As expected, the lowest OA signal intensity appears prior to the ablation due to the lowest temperature in the sample and lack of coagulation. A strong increase in the OA signal amplitude can be observed as the lesion progresses (3.3b, first 30 s in 3.3d). The signal increase is attributed to the enhanced lesion contrast associated to tissue coagulation [19] as well as the strong temperature dependence of the Grüneisen parameter in tissues [20]. While previously suggested approaches were afflicted by strong light attenuation in deep tissues thereby necessitating signal averaging [19], direct delivery of the excitation light into the ablated region via the catheter-based approach allows for monitoring of lesion without signal averaging. This represents a significant advantage of the integrated RAOM method for real-time clinical application. In 3.3c the OA images are further compared with gross pathology of the specimen taken after the RF ablation experiment, confirming a uniform coagulum without charring and a good qualitative correspondence between the yellow colored volume in the OA images and the appearance of coagulated area in the sliced specimen. As expected, cooler tissue (3.3c and 3.3d, t=180 s) exhibits lower OA signal levels as compared to the end of ablation time point (t = 30 s), which is attributed to the temperature dependence of the OA signals [20]. The OA signal levels at t=180s remain higher than in the pre-ablated specimen, supposedly due to incomplete cool-down and residual thermal diffusion effects in the rest of the sample. Note however that the signal in the coagulated zone (blue square in 3.3b) does not decline significantly during the cool-down period (blue plot in 3.3d), which is ascribed to an increase in optical absorption coefficient caused by denaturized tissue proteins in the coagulum [21].

The presented results illustrate the basic feasibility of the suggested integrated RAOM approach for simultaneous RF ablation and real-time OA monitoring of the lesion progression. Because of direct light delivery through the catheter, the ablated region is efficiently illuminated, thus enabling monitoring of deep-seated lesions. Evidently, *in vivo* experimentation is essential to demonstrate the applicability of the proposed monitoring configuration in a real clinical setting. For this, several outstanding technical issues need also to be addressed. The ablation tip diameter of 6 mm is to be reduced to the typical 4 mm electrodes used in RFCA, which can be achieved by reducing the size of the encapsulating steel ferrule, denser packing
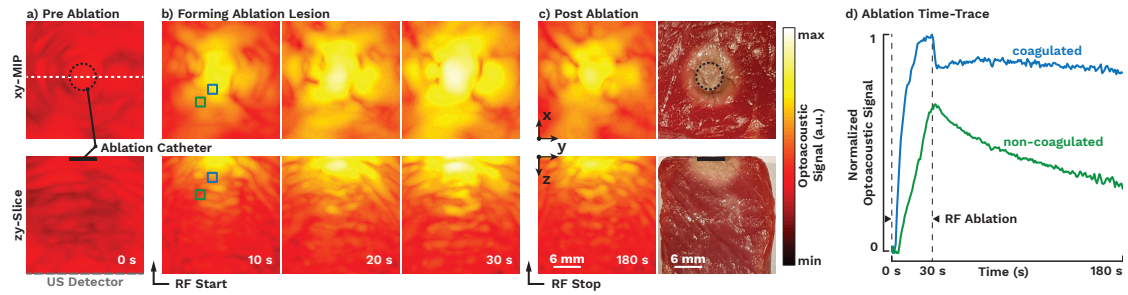
Figure 3.3.: Real-time optoacoustic monitoring of RF ablation in *ex vivo* porcine heart tissue. (a) OA images acquired from un-ablated tissue. (b) Non-invasive OA imaging of the lesion formation in 3D. (c) OA image acquired after the cool-down phase along with the photograph of coagulated area from a sliced specimen. Images on the top are top-view MIPs while the bottom row shows a single (z-y) slice through the center of the reconstructed OA volumes, as indicated by the white dashed line in (a). (d) Time evolution of the OA signal during and after RF ablation in the locations indicated in panel b.
Reproduced with permission from [26]. © The Optical Society.

the copper-coated fibers and/or reducing the number of fibers, the latter also resulting in a more flexible catheter design. This would allow for the integration of the RAOM catheter into conventional steerable catheter shafts, thus adding additional functionality, such as electrocardiographic and temperature monitoring at the tip. Both the ablation catheter and its tip could be further adapted to fit different types of ablation procedures. For instance, RF tumor ablation is regularly performed with large area ablation catheters, which can be achieved using a longer steel ferule at the ablation tip of the RAOM catheter [28]. The presented results indicate the basic feasibility of identifying changes related to tissue heating and coagulation with the suggested RAOM approach, making its potential combination with existing catheter and monitoring modalities simple and cost-effective. We observed dynamic changes in the OA images of forming RF lesions that corresponded well with the gross lesion pathology. However, the observed changes in the OA signal only allow for a qualitative assessment of the forming lesion, as the method does not allow for differentiating between alterations in the optical absorption due to coagulation versus changes of the temperature-dependent Grüneisen parameter. This can be possibly achieved via a multi-spectral imaging approach [29], thus attaining both real-time and quantitative feedback on the temperature distribution and the size of coagulated area during the intervention. Yet, real-time temperature mapping may still be possible in un-coagulated tissue areas where no alterations of the

optical tissue properties have occurred [29].

In conclusion, the suggested catheter combining RF ablation and light delivery for OA excitation in a single flexible and adaptable design represents an advantageous solution for optimizing the outcome of RFCA interventions. The high spatio-temporal resolution and deep-tissue imaging capacity of the integrated ablation monitoring approach anticipate its general applicability in a number of RF ablation procedures.

Acknowledgements

References

[1] **Johannes Rebling**[†] et al. „Integrated catheter for simultaneous radio frequency ablation and optoacoustic monitoring of lesion progression". In: *Optics letters* 43.8 (Apr. 2018), pp. 1886–1889.

    DOI: 10.1364/ol.43.001886.

[2] G. Pang et al. „Three-Dimensional Optoacoustic Monitoring of Lesion Formation in Real Time During Radiofrequency Catheter Ablation". In: *Journal of Cardiovascular Electrophysiology* 26.3 (2015).

    DOI: 10.1111/jce.12584.

[3] **Johannes Rebling** et al. „A new catheter design for combined radiofrequency ablation and optoacoustic treatment monitoring using copper-coated light-guides". In: *Optical Fibers and Sensors for Medical Diagnostics and Treatment Applications XVIII*. Ed. by Israel Gannot. Vol. 10488. International Society for Optics and Photonics. SPIE, Feb. 2018, p. 1048805.

    DOI: 10.1117/12.2287390.

[4] Roger J. Zemp. *Spotlight on Optics - Integrated catheter for simultaneous radio frequency ablation and optoacoustic monitoring of lesion progression*. 2018. URL: `https://www.osapublishing.org/spotlight/summary.cfm?id=385493` (visited on 11/09/2018).

[5] M. Pai et al. „Endoscopic ultrasound guided radiofrequency ablation, for pancreatic cystic neoplasms and neuroendocrine tumors". In: *World J Gastrointest Surg* 7.4 (2015), pp. 52–9.
DOI: `10.4240/wjgs.v7.i4.52`.

[6] Craig T. January et al. „2014 AHA/ACC/HRS Guideline for the Management of Patients With Atrial Fibrillation: Executive Summary A Report of the American College of Cardiology/American Heart Association Task Force on Practice Guidelines and the Heart Rhythm Society". In: *Circulation* 130.23 (2014), pp. 2071–2104.
DOI: `10.1161/CIR.0000000000000040`.

[7] S. S. Yu, W. D. Tope, and R. C. Grekin. „Cardiac devices and electromagnetic interference revisited: new radiofrequency technologies and implications for dermatologic surgery". In: *Dermatologic Surgery* 31.8 Pt 1 (2005), pp. 932–40.
DOI: `10.1111/j.1524-4725.2005.31808`.

[8] Carlo Pappone et al. „Circumferential Radiofrequency Ablation of Pulmonary Vein Ostia A New Anatomic Approach for Curing Atrial Fibrillation". In: *Circulation* 102.21 (2000), pp. 2619–2628.
DOI: `10.1161/01.CIR.102.21.2619`.

[9] T. Terasawa, E. M. Balk, and M. Chung. „Comparative Effectiveness of Radiofrequency Catheter Ablation for Atrial Fibrillation". In: *Comparative Effectiveness Review* 15 (2009).

[10] Michel Haïssaguerre et al. „Electrophysiological End Point for Catheter Ablation of Atrial Fibrillation Initiated From Multiple Pulmonary Venous Foci". In: *Circulation* 101.12 (2000), pp. 1409–1417.
DOI: `10.1161/01.CIR.101.12.1409`.

[11] M. Harvey et al. „Impedance Monitoring During Radiofrequency Catheter Ablation in Humans". In: *Pacing and Clinical Electrophysiology* 15.1 (1992).
DOI: 10.1111/j.1540-8159.1992.tb02897.x.

[12] H. Calkins et al. „Temperature monitoring during radiofrequency catheter ablation procedures using closed loop control. Atakr Multicenter Investigators Group". In: *Circulation* 90.3 (1994), pp. 1279–1286.
DOI: 10.1161/01.cir.90.3.1279.

[13] Z. Liu et al. „Characterization of the RF ablation-induced 'oven effect': the importance of background tissue thermal conductivity on tissue heating". In: *International Journal of Hyperthermia* 22.4 (2006).
DOI: 10.1080/02656730600609122.

[14] Christopher J. McGann et al. „New Magnetic Resonance Imaging-Based Method for Defining the Extent of Left Atrial Wall Injury After the Ablation of Atrial Fibrillation". In: *Journal of the American College of Cardiology* 52.15 (2008), pp. 1263–1271.
DOI: 10.1016/j.jacc.2008.05.062.

[15] D. Herranz et al. „Novel catheter enabling simultaneous radiofrequency ablation and optical coherence reflectometry". In: *Biomedical Optics Express* 6.9 (2015).
DOI: 10.1364/boe.6.003268.

[16] M. Wood et al. „Direct Measurement of the Lethal Isotherm for Radiofrequency Ablation of Myocardial Tissue". In: *Circulation Arrhythmia and Electrophysiology* 4.3 (2011).
DOI: 10.1161/CIRCEP.110.961169.

[17] Chiao-Yin Wang et al. „Monitoring radiofrequency ablation with ultrasound Nakagami imaging". In: *Medical physics* 40.7 (2013).
DOI: 10.1118/1.4808115.

[18] R. O. Esenaliev et al. „Studies of acoustical and shock waves in the pulsed laser ablation of biotissue". In: *Lasers in Surgery and Medicine* 13.4 (1993), pp. 470–84.
DOI: 10.1002/lsm.1900130412.

[19]   N. Dana et al. „In vitro photoacoustic visualization of myocardial ablation lesions".
        In: *Heart Rhythm* 11.1 (2014), pp. 150–7.
        DOI: 10.1016/j.hrthm.2013.09.071.

[20]   Irina V. Larina, Kirill V. Larin, and Rinat O. Esenaliev. „Real-time optoacoustic mon-
        itoring of temperature in tissues". In: *Journal of Physics D: Applied Physics* 38.15
        (2005), pp. 2633–2639.
        DOI: 10.1088/0022-3727/38/15/015.

[21]   Kirill V. Larin, Irina V. Larina, and Rinat O. Esenaliev. „Monitoring of tissue coag-
        ulation during thermotherapy using optoacoustic technique". In: *Journal of Physics
        D: Applied Physics* 38.15 (2005), pp. 2645–2653.
        DOI: 10.1088/0022-3727/38/15/017.

[22]   Deán-Ben X. L. et al. „Advanced optoacoustic methods for multiscale imaging of in
        vivo dynamics". In: *Chemical Society Reviews* 46.8 (2017), pp. 2158–2198.
        DOI: 10.1039/c6cs00765a.

[23]   Trevor Mitcham et al. „Photoacoustic imaging driven by an interstitial irradiation
        source". In: *Photoacoustics* 3.2 (2015), pp. 45–54.
        DOI: 10.1016/j.pacs.2015.02.002.

[24]   Deán-Ben X. L. and D. Razansky. „Functional optoacoustic human angiography with
        handheld video rate three dimensional scanner". In: *Photoacoustics* 1.3-4 (2013),
        pp. 68–73.
        DOI: 10.1016/j.pacs.2013.10.002.

[25]   Deán-Ben X. L., A. Ozbek, and D. Razansky. „Volumetric real-time tracking of pe-
        ripheral human vasculature with GPU-accelerated three-dimensional optoacoustic to-
        mography". In: *IEEE Trans Med Imaging* 32.11 (2013), pp. 2050–5.
        DOI: 10.1109/TMI.2013.2272079.

[26]   **Johannes Rebling** et al. „In-vivo assessment of radiation-induced cerebrovascular
        damage in mice by hybrid optoacoustic-ultrasound bio-microscopy (Conference Pre-
        sentation)". (Conference Presentation). In: *Photons Plus Ultrasound: Imaging and*

Sensing 2018. Ed. by Alexander A. Oraevsky and Lihong V. Wang. Vol. 10494. International Society for Optics and Photonics. SPIE, Mar. 2018, p. 104940I.

DOI: 10.1117/12.2290493.

[27] S. L. Jacques. „Optical properties of biological tissues: a review". In: *Physics in Medicine and Biology* 58.11 (2013), R37–61.

DOI: 10.1088/0031-9155/58/11/R37.

[28] S. N. Goldberg. „Radiofrequency tumor ablation: principles and techniques". In: *European Journal of Ultrasound* 13.2 (2001), pp. 129–47.

DOI: 10.1016/S0929-8266(01)00126-4.

[29] Daniel Razansky. „Multispectral Optoacoustic Tomography—Volumetric Color Hearing in Real Time". In: *IEEE Journal of Selected Topics in Quantum Electronics* 18.3 (2012), pp. 1234–1243.

DOI: 10.1109/jstqe.2011.2172192.

4. Dual-wavelength hybrid optoacoustic-ultrasound biomicroscopy for functional imaging of large-scale cerebral vascular networks

Johannes Rebling[†], Héctor Estrada[†], Sven Gottschalk, Gali Sela, Michael Zwack, Georg Wissmeyer, Vasilis Ntziachristos, and Daniel Razansky. „Dual-wavelength hybrid optoacoustic-ultrasound biomicroscopy for functional imaging of large-scale cerebral vascular networks".
In: *Journal of biophotonics* (May 2018), e201800057.
DOI: `10.1002/jbio.201800057`

Summary and Author Contribution

Simultaneous structural and functional imaging of neurovasculature is very challenging due to the acoustical and optical barriers formed by the skull and brain. Existing imaging approaches only provide information over a limited field-of-view (FOV) and are thus not able to image the entire cerebral vascular network. This chapter presents the hybrid-focus optoacoustic microscope (HFOAM) which is capable of rapid imaging of murine neurovasculature in-vivo, with high spatial resolution and a large field of view. The systems capability to perform dual wavelength imaging allows visualization of functional parameters through the intact skull. Simultaneous pulse-echo ultrasound provides complementary imaging contrast. The flexible hybrid design in combination with fast high-resolution imaging in 3D holds promise for generating better insights into the architecture and function of the neurovascular system. My contribution to the presented manuscript where the following:

Methodology The presented system is the result of continuous development of the HFOAM

system over the last years [2]. I improved and further developed large parts of the existing hardware setup, most importantly the optics used for dual-wavelength imaging and coupling into the delicate photonic crystal fiber (PCF). Additionally, I have improved the performance of the receive electronics, thus significantly reducing electronic noise and hence improving the systems overall sensitivity. The hardware development was performed with major contributions from Héctor Estrada and with help form Gali Sela, Michael Zwack and Georg Wissmeyer.

Data Collection I recorded phantom data for the resolution and unmixing characterization. *In vivo* mouse ear and brain imaging was performed by Héctor Estrada and myself with the help of Michael Reiss and Sven Gottschalk.

Computation I completely rewrote and optimized the software used for both data acquisition and post-processing of the acquired data based on code developed by Héctor Estrada and Jake Turner. This enabled high throughput studies due to improved system stability and performance. I further optimized the image processing of the acquired images, thus optimizing imaging quality of the final images.

Writing and Revisions I prepared the initial manuscript with significant contributions from Héctor Estrada and Daniel Razansky and help from all authors. I created all figures including the shown schematics. For the review process, Héctor Estrada and I amended the manuscript and modified the figures as per reviewer request and with significant contributions from Daniel Razansky.

This study was presented at the *SPIE Photonics West BIOS 2017* conference and was featured on the front cover of the *Journal of Biophotonics* in September 2018 [3, 4].

Abstract

A critical link exists between pathological changes of cerebral vasculature and diseases affecting brain function. Microscopic techniques have played an indispensable role in the study of neurovascular anatomy and functions. Yet, investigations are often hindered by sub-optimal

trade-offs between the spatiotemporal resolution, field-of-view and type of contrast offered by the existing optical microscopy techniques. We present a hybrid dual-wavelength optoacoustic biomicroscope capable of rapid transcranial visualization of large-scale cerebral vascular networks. The system offers 3D views of the morphology and oxygenation status of the cerebral vasculature with single capillary resolution and a field of view exceeding 6x8 mm^2, thus covering the entire cortical vasculature in mice. The large-scale optoacoustic imaging capacity is complemented by simultaneously acquired pulse-echo ultrasound biomicroscopy scans of the mouse skull. The new approach holds great potential to provide better insights into cerebrovascular function and facilitate efficient studies into neurological and vascular abnormalities of the brain.

4.1. Introduction

Many diseases affecting neurological functions can be linked to pathological alterations of the cerebral vasculature. Some of the alterations are known to cause the disease, support and accelerate its spread , while in many other cases the interaction between the disease etiology and vascular pathology is only poorly understood, as in the case of Alzheimer's disease.[5–7] This critical link between vascular changes and disease is increasingly targeted by pre-clinical studies in mouse models mimicking the pathological changes in human cerebrovasculature.[8]

Imaging techniques, such as positron emission tomography (PET), single-photon emission computed tomography (SPECT) and functional magnetic resonance imaging (fMRI) are commonly used to provide metabolic and functional brain images in humans.[9–11] However, they lack the required micron-scale spatial resolution, necessitate exogenous contrast agents and are generally costly. Various intravital techniques, such as confocal and two-photon microscopy, optical coherence tomography or functional ultrasound (US), enable *in vivo* imaging with sufficient spatial resolution to visualize activity in single cells and capillaries and allow for three-dimensional (3D) interrogation of the microvasculature in small animal brains.[12–14] Nevertheless, exogenous contrast agents are required for imaging oxygenation parameters with those techniques, while other limitations stem from their invasive nature and/or limited FOV.

Optoacoustic (OA) imaging techniques have recently provided unprecedented insights into the deep-tissue anatomy and physiology of animal model organisms due to the unique combination of rich and endogenous optical absorption contrast and weak scattering of US waves in biological tissues.[15, 16] Label-free OA tomography and acoustic-resolution microscopy have enabled long-term studies in living model organisms at centimetre-scale depths and have successfully been applied for deep brain imaging in zebrafish and mice.[17–19] Optical-resolution OA microscopy has further offered high spatial resolution in visualizing finest capillaries and sub-cellular structures as well as label-free mapping of oxygen saturation dependent absorption of oxy- and deoxyhemoglobin in the murine brain.[2, 20]

Imaging performance yet greatly differs among the different OA microscopy systems. For instance, a design based on a two-axis galvo-scanner has attained B-scan speed in the 1 mm/s range while additional depth scanning was necessary for rendering 3D image volumes due to the shallow optical focus.[21] A fast voice-coil scanning system was alternatively used to attain an extended lateral FOV and higher imaging speed, whereas the effective FOV in the depth direction was similarly limited by the high-numerical aperture (NA) focusing optics and reduced detection sensitivity due to the use of an optical-acoustic beam combiner.[22] Additional performance limitations stem from the lack of high pulse repetition frequency (PRF) lasers with wavelength tuning capacity essential for spectroscopic differentiation of the blood oxygen saturation. This has been partially overcome by employing two separate laser sources at 532 nm and 559 nm running at a PRF of 30 kHz, which have enabled simultaneous extraction of vascular anatomy, oxygen saturation, and blood flow.[21] The relatively slow PRF has nevertheless limited the maximum B-scan speed to about 1 mm/s, resulting in slow mechanical scanning and long image acquisition times. By employing two 100 kHz repetition lasers with different pulse durations and exploiting the difference between saturation of the OA signal by oxy- and deoxy-hemoglobin, fast MEMS-based functional OA microscopy has been recently demonstrated.[23] However, the employed saturation-based approach required high light fluence levels at the optical focus, greatly exceeding the in-vivo safety limits and potentially causing RBC damage.[24] In addition, the FOV in this study was limited to 3x3 mm^2 and the strong optical focus resulted in a narrow focal depth of

less than 150 µm (calculated as the Rayleigh length), requiring both tiling in the lateral plane as well as depth scanning to image the entire cortical vasculature in 3D. The presented design furthermore relied on a highly customized water-immersible MEMS scanner, which is not readily available. The latter was replaced by a conventional galvanometer mirror in a non-conducting liquid, the design yet suffering from a similarly limited FOV and shallow depth-penetration.[25]

To address these unmet challenges, we present a fast functional OA microscopy method that uses a Pockels-cell-based wavelength switching for rapid acquisition of the spectral data. The microscope is based on a coaxial alignment of the optical and acoustic foci within a fast moving scan-head, which features a low-NA optical focus for extended imaging depth and a rapid 3D image acquisition over large lateral FOV covering an entire mouse cortex. The system is furthermore capable to simultaneously image in US pulse-echo mode, allowing for an extraction of additional anatomical data of the murine skull.

4.2. Materials and Methods

4.2.1. Optoacoustic Biomicroscopy Setup

A schematic diagram of the biomicroscope is shown in Figure 4.1, with an overview of the dual-wavelength optics displayed in Figure 4.1a and an illustration of the fast scan head shown in Figure 4.1b. The core of the microscope is formed by an optical system that enables rapid wavelength switching in combination with a fast-moving scan head sampling the specimen in epi-illumination mode. Fast switching (up to 10 kHz) between 532 nm wavelength (close to the isosbestic point of hemoglobin at 529 nm) and a second wavelength tunable in the 565-595 nm range is used for spectral unmixing of the oxygen saturation.[20, 26] Linearly polarized light with a wavelength of 532 nm is generated by a Q-switched, diode end-pumped Nd:YAG laser (10 ns pulse length, model: IS8II-E, EdgeWave, Würselen, Germany). The pumping wavelength is either directly coupled into a single-mode, large mode area photonics crystal fiber (PCF, model: LMA-20, NKT Photonics, Birkerød, Denmark) or first guided into a dye laser (Credo, Sirah Lasertechnik, Grevenbroich, Germany, using a Pyrromethene 597 dye) for

generating a second wavelength tunable in the 570-610 nm range. Switching between the two wavelengths is achieved by combination of a Pockels cell (PC, model: PC12SR-532, Eksma Optics, Vilnius, Lithuania) and a polarizing beam splitter (PBS, model: 420-1254HT, Eksma Optics, Vilnius, Lithuania). When activated, the PC rotates the linearly polarized 532 nm light by 90°, thus enabling its transmission by the PBS into the dye laser. In contrast, the 532 nm light is reflected by the PBS when its polarization is not altered by an inactive PC.
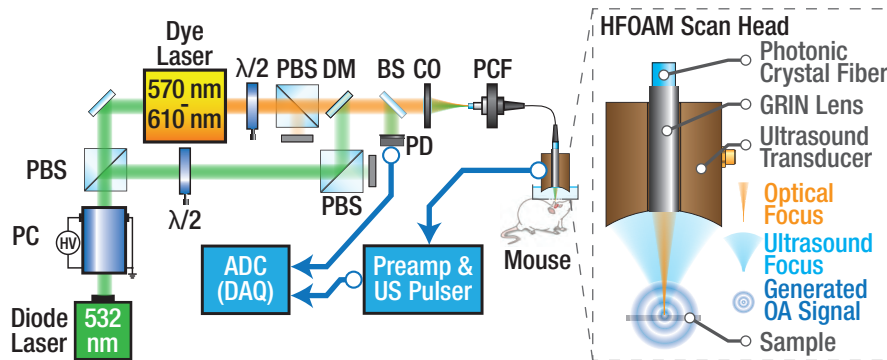

Figure 4.1.: (a) Schematic diagram of the dual-wavelength hybrid biomicroscopy system. Both 532 nm and 578 nm pulsed laser light is coupled into a Pockels cell (PCF) terminating in the fast-moving scan head, which records both the optoacoustic and pulse-echo ultrasound responses. PC-Pockels cell, PBS-polarizing beam splitter, $\lambda/2$-half-wave plate, DM-dichroic mirror, BS-beam sampler, CO-collimating lens, ADC-analog-to-digital converter, DAQ-data acquisition system. (b) Drawing of the scan head featuring a coaxial alignment of the optical and acoustic foci for hybrid imaging. Reproduced with permission from [27]. © Wiley-VCH.

The pulse energy of both the 578 nm and the 532 nm paths can be adjusted by means of a half-wave plate (AHWP10M-980 for 532 nm, WPH10M-532 for 578 nm, Thorlabs, Newton, USA) and an additional PBS (PBS25-532-HP for 532 nm, PBS251 for 578 nm, Thorlabs, Newton, USA) in each beam path, which allows the precise adjustment of the average pulse energies for both wavelengths. Both wavelengths are combined by a dichroic mirror (DMLP550, Thorlabs, Newton, USA) and coupled into the PCF by an achromatic lens (AC254-100-A, Thorlabs, Newton, USA). The distal end of the PCF terminates in a gradient-index (GRIN) lens (GRINTECH, Jena, Germany) which focuses the excitation light at a distance of 6.5 mm from the fiber end, as shown in 4.1b. The GRIN lens is mounted inside an opening in the center of a custom-made, spherically focused PVdF-based US detector having an ultrawideband frequency response extending beyond 35 MHz (Precision

Acoustics, Dorchester, United Kingdom). The optical and acoustic foci are aligned coaxially and confocally without the need for an optical-acoustic beam combiner [22], resulting in an optimized detection sensitivity. For volumetric imaging, the scan-head is rapidly oscillated along the x-axis by means of a fast piezostage (M-683, PI, Karlsruhe, Germany) while a second linear stage (LTM 60F-25 HSM, OWIS, Staufen, Germany) moves slowly and continuously along the y-axis, thus sampling the imaging target in a zigzag pattern. Optoacoustic A-scans are recorded by the US transducer and amplified by an 8 dB pre-amplifier (Precision Acoustics, Dorchester, United Kingdom) and a 24 dB low-noise amplifier (ZFL-500LN, Mini-Circuits, New York, USA) before they are digitized by a two-channel, 250 MS/s, 14-bit data acquisition card (M3i.4142, Spectrum Systementwicklung Microelectronic, Grosshansdorf, Germany). Pulse-echo US recording are performed using a pulser-receiver (5073PR, Olympus, Massachusetts, USA) and the same data acquisition chain. The precise position of the fast scanning stage (x-axis) is measured in real-time during the scan using a laser distance sensor (M11L/10, MEL Mikroelektronik GmbH, Eching, Germany), whose readings are sampled by a second DAQ card (NI PCIe-6321, National Instruments, Austin, USA) and converted into stage position values using a look-up table. The latter is based on an initial slow calibration with a build-in stage encoder. The position of the slowly and continuously moving stage (y-axis) is calculated based on the known acceleration and velocity of the stage. The step-size between adjacent A-scans can be adjusted by varying the laser PRF and/or speed of the scan-head. For each x-y position, the generated OA responses are recorded at both 532 nm and 578 nm wavelengths. The laser, Pockels cell and data acquisition are synchronized by a programmable pulse generator (PulseBlaster SP17, SpinCore Technologies, Gainesville, USA). In order to correct for per-pulse laser energy fluctuations, a small fraction the laser beam is split off by a beam sampler (BSF10-A, Thorlabs, Newton, USA), detected by a fast, calibrated photodiode (DET10A, Thorlabs, Newton, USA) and digitized by the second channel of the data acquisition card. The photodiode is calibrated prior to imaging by independently measuring the per-pulse energies for both wavelengths at the output of the GRIN lens using a power-meter (J-25MB-LE, Coherent Inc., Santa Clara, USA). The separate A-Scans are then remapped onto a regularly spaced 3D grid using bilinear interpolation.

4.2.2. Resolution Characterization

The lateral resolution of the hybrid dual-wavelength microscope was characterized in both OA and US modes using sharp edge of a silicon sample which was moved axially across the focus over a range of 2 mm with 100 μm steps. For each z-position, a 3D dataset was recorded and the resolution calculation was performed on the 2D maximum intensity projection (MIP) images, as shown in Figure 4.2a. The resolution analysis further shown in Figure 4.2b was performed by fitting a sigmoid line-spread function (LSF, red, solid line) to the measured edge response (blue dots). The point-spread function (PSF, yellow, dashed line) is then calculated as the derivative of the PSF and the resolution is measured as the full width at half maximum (FWHM) of the PSF.

4.2.3. Characterization of the Spectral Unmixing Capability

Ink filled tube phantoms were imaged to demonstrate and validate the spectral unmixing capabilities of the system (Figure 4.3). To this end, four crossing polyethylene tubes (outer diameter 500 μm, inner diameter 300 μm) were filled with varying concentrations of blue ink mixed into red ink (both Pelikan, Hannover, Germany), as shown in Figure 4.3a. The absorption spectra of both inks, as measured by a spectrophotometer (USB4000, Ocean Optics, Dunedin, USA), are shown in Figure 4.3b. The phantom was then positioned inside a water-filled Petri dish and scanned in both OA and US modes.

4.2.4. *In Vivo* Mouse Imaging

To showcase system's ability to extract both morphological and functional data of complex vascular networks, murine ear and brain were imaged. Six-week-old female athymic nude-Foxn1nu mice (Harlan Laboratories LTD, Itingen, Switzerland) were used for imaging, in full compliance with European laws on the protection of animals used for scientific purpose and the institutional guidelines of the Helmholtz Center Munich, and with approval from the Government District of Upper Bavaria. Animals were anaesthetized with isoflurane (1.5% to 2.5% v/v) in 100% O_2. Physiological parameters, including blood oxygenation, heart rate, and body temperature were continuously monitored throughout the experiments. The
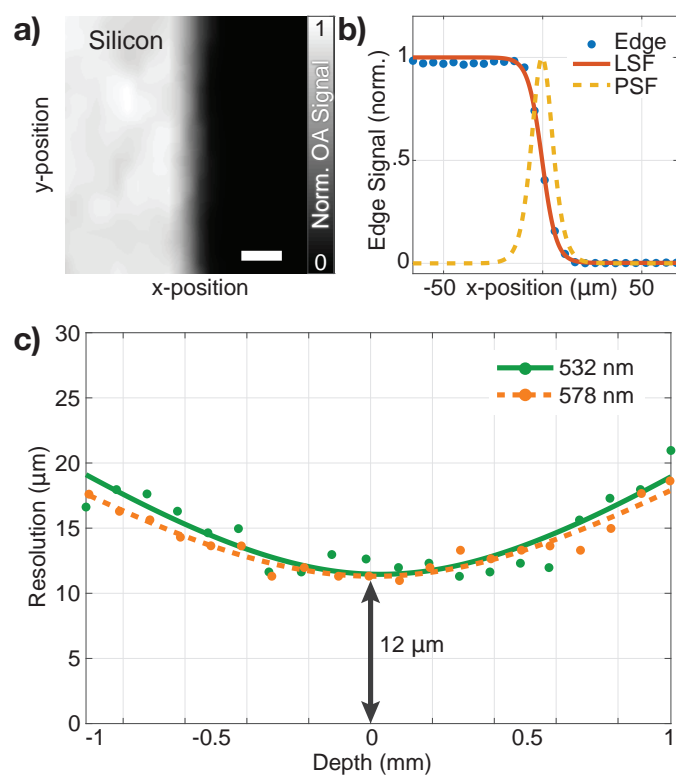
Figure 4.2.: Optoacoustic resolution characterization using a sharp silicon edge for both 532 nm and 578 nm excitation wavelengths, displaying the long depth of focus of the low-NA gradient index lens. (a) Optoacoustic maximum intensity projection (MIP) image of the silicon edge placed in the optical focus. Scale bar - 10 µm. (b) Resolution characterization based on the full width at half maximum of the point-spread function (PSF, yellow dashed line) calculated as the derivative of the line-spread function (LSF, red solid line) fitted to the recorded optoacoustic image of the edge (blue dots). (c) OA imaging resolution as a function of imaging depth, with an in-focus resolution of 12 µm for both 532 nm (green solid line) and 578 nm (orange dashed line).
Reproduced with permission from [27]. © Wiley-VCH.

temperature was kept constant using a rectal thermometer and a feedback-controlled heating pad (PhysioSuite, Kent Scientific, Torrington, USA). A custom-designed stereotactic mouse head holder (Narishige International Limited, London, UK) was used to avoid animal motion. The scan head was immersed in a water-filled Petri dish for acoustic coupling and both ear and brain were imaged through a hole in the Petri dish sealed with polyvinylidene chloride foil and using US gel as acoustic coupling medium between the animal and the foil. The mouse ear was fixed to a custom-made mount to ensure a flat topology of the imaged surface. The animal fully recovered within a few minutes after the imaging. The mouse brain was imaged in both OA and US mode with the scalp removed but with the skull intact. The mouse was sacrificed following the brain imaging experiment.

4.3. Results and Discussion

4.3.1. Resolution Characterization

The result of the resolution characterization is shown in Figure 4.2. The small diameter and the long focal distance of the GRIN lens cause a very low NA of 0.025. This NA results in a diffraction-limited lateral resolution in the 11-20 µm range across an extended depth of focus of more than 2 mm. Owing to low NA, the lateral resolution deteriorates by only a factor of $\sqrt{2}$ over a depth range of 2 mm, thus eliminating the need for depth scanning. The axial direction the system's performance is determined by the available US detector bandwidth, effectively translating into an axial resolution of about 44 µm.[2]

4.3.2. Ink Phantom Imaging

OA images of the ink phantom acquired at 532 nm and 578 nm wavelengths are presented in Figure 4.3 along with the US pulse-echo US image and a color photograph of the phantom. Both the red and blue inks have near identical optical absorption at 532 nm, resulting in an equal OA amplitude, as shown in Figure 4.3a for all the four tubes. In contrast, the absorption of the blue ink is much higher at 578 nm, resulting in an increased OA signal with the increasing blue ink concentrations, as shown in Figure 4.3b. Using spectral unmixing,

we were able to accurately measure the ink concentrations, as displayed in Figure 4.3e.
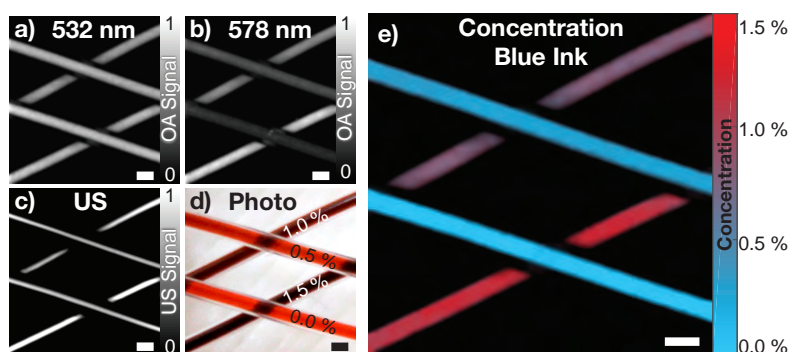

Figure 4.3.: Dual wavelength optoacoustic imaging of ink-filled tubes, validating the spectral unmixing capabilities of the system. (a) & (b) Optoacoustic images recorded at 532 nm and 578 nm, respectively. (c) Corresponding ultrasound pulse-echo MIP image. (d) Photo of the ink-filled tubes, indicating concentration of blue ink in the red-blue ink solution. (f) Mapping the blue ink concentration using the dual-wavelength linear unmixing method. Scale bars - 500 µm.
Reproduced with permission from [27]. © Wiley-VCH.

4.3.3. *In Vivo* Imaging

The large-scale imaging capabilities of the system are demonstrated in both Figure 4.4 and 4.5, showing vascular networks in the murine ear and brain, respectively. Figure 4.4a displays the vessel-rich network in the ear imaged over a FOV of 3x4 mm^2 with per pulse laser energy of 1 µJ.[24] Using the dual-wavelength tuning capabilities, the oxygen saturation in the vasculature was further visualized, as shown in Figure 4.4b. The oxygen saturation map shows typical artery-vein pairs present in the murine ear, with smaller arteries and capillaries providing oxygenated blood to the cells and larger veins removing the deoxygenated blood. The dual-wavelength 3D data acquisition took less than 30 s with a step size of 10 µm and the fast stage moving at an average velocity of 50 mm/s.

Figure 4.5a shows a depth-encoded MIP of the intricate network formed by vessels both in the skull and the cortex imaged over a large 6x8 mm^2 area and with the skull intact. Large veins draining into the superior sagittal sinus (SSS) as well as fine pial arteries supplying the cortex with oxygen are clearly resolvable in the image. Figure 4.5b further displays the corresponding oxygen saturation maps revealing the complex morphology of the highly hypoxic sinusoidal veins located in the skull.[28] The dual-wavelength OA data was recorded
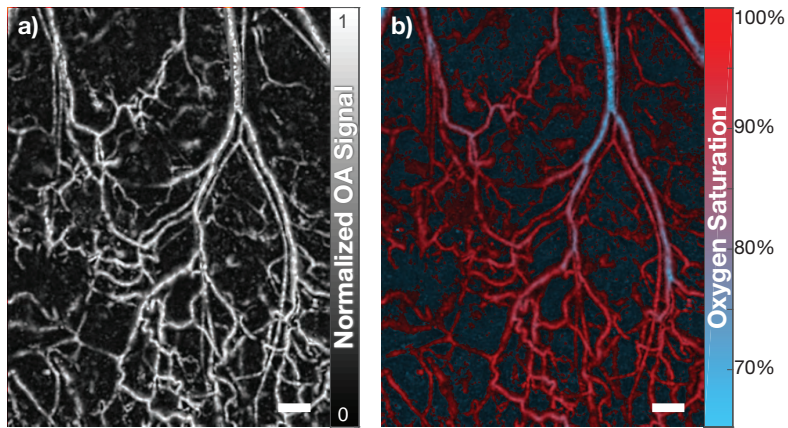
Figure 4.4.: Morphological and functional *in vivo* imaging of a nude mouse ear. (a) Both large arteries and veins as well as fine capillaries can be resolved within the acquired 3x4 mm^2 field-of-view. (b) Oxygen saturation is further extracted using the dual-wavelength linear unmixing method. Scale bar 300 μm.
Reproduced with permission from [27]. © Wiley-VCH.

within less than 100 s and a with step size of 10 μm whereas the corresponding US scan over the same FOV with a step size of 20 μm was recorded within 30 s. The naturally co-registered US pulse-echo scan (Figure 4.5c), recorded prior to the OA dataset, shows precise morphology of the skull, with landmarks such as the separate bone plates and sutures labelled. Note that both volumetric OA and pulse-echo US data were each obtained by a single scan in the lateral plane without the need for additional scanning along the depth dimension, tilling or averaging. Important anatomical landmarks including the crossing of the sagittal and lambdoid sutures (the so-called lambda), as well as the bregma, represented by the crossing between the sagittal and coronal sutures, are easily identified in the US image. The US data may be used to accurately map location of the optoacoustically-recorded vasculature with respect to the skull, which can be subsequently used to correct for skull-induced signal aberrations, thus improving image resolution and contrast and facilitating correct interpretation of the OA data.[29] Finally, the precise skull geometry revealed by the pulse-echo US images may potentially aid in guiding intracranial injections of extrinsic labels and drugs, further minimizing collateral vascular damage.[30]
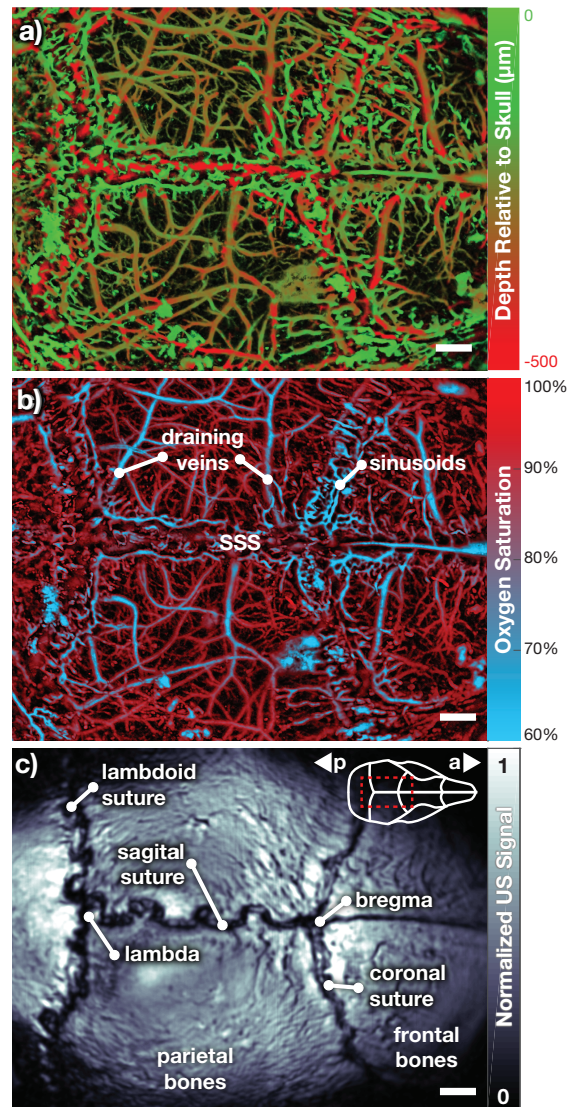
Figure 4.5.: Morphological (a) and functional (b) OA images recorded from cerebral murine vasculature through an intact skull. (c) The co-registered volumetric pulse-echo US image showing the fine skull morphology. Insert in c) displays the approximate location of the field-of-view. Scale bar - 600 µm. SSS - superior sagittal sinus, a - anterior, p - posterior.
Reproduced with permission from [27]. © Wiley-VCH.

4.4. Conclusion and Outlook

A novel hybrid OA and US biomicroscopy approach capable of large-scale morphological and functional brain imaging was realized using dual-wavelength illumination. Rapid wavelength switching in combination with fast mechanical scanning and a flexible, highly sensitive scan head design have enabled the high-speed visualization of both morphology and oxygenation status of large-scale vascular networks with lateral resolution of 12 μm across FOVs covering the entire murine cortex. The flexible scan-head design allows for concurrent high-resolution pulse-echo US scans, providing additional anatomical information.

The large FOV comes as a trade-off for volumetric imaging speed, which could be inferior to other fast scanning solutions providing smaller FOVs.[21, 23, 25] Nevertheless, the imaging speed is presently limited by the 10 KHz PRF of the laser source. While faster pulsed sources are readily available at 532 nm wavelength, availability of pulsed lasers in the 540-600nm range is limited. Recently, lasers based on stimulated Raman scattering (SRS) in optical fibers have been shown to generate sufficient per-pulse energies in this spectral band,[31, 32] thus can potentially be exploited for accelerating image acquisition with the proposed design.

In conclusion, the presented biomicroscope can bridge the gap between localized microscopic observations and lower-resolution (macroscopic) imaging in whole mouse brains, thus offering a new scalable multimodal tool for investigating healthy and pathological neurovasculature.

Acknowledgements

References

[1] **Johannes Rebling**[†] et al. „Dual-wavelength hybrid optoacoustic-ultrasound biomicroscopy for functional imaging of large-scale cerebral vascular networks". In: *Journal of biophotonics* (May 2018), e201800057.

DOI: 10.1002/jbio.201800057.

[2] H. Estrada et al. „Real-time optoacoustic brain microscopy with hybrid optical and acoustic resolution". In: *Laser Physics Letters* 11.4 (2014), p. 45601.

DOI: Artn04560110.1088/1612-2011/11/4/045601.

[3] **Johannes Rebling** et al. „Hybrid ultrasound and dual-wavelength optoacoustic biomicroscopy for functional neuroimaging". (Conference Poster and Proceedings Paper). In: *Photons Plus Ultrasound: Imaging and Sensing 2017*. Ed. by Alexander A. Oraevsky and Lihong V. Wang. Vol. 10064. International Society for Optics and Photonics. SPIE, Mar. 2017, 100644T.

DOI: 10.1117/12.2250635.

[4] Journal of Biophotonics, ed. *Front Cover: Dual-wavelength hybrid optoacoustic-ultrasound biomicroscopy for functional imaging of large-scale cerebral vascular networks*. 2018. URL: https://onlinelibrary.wiley.com/doi/10.1002/jbio.201870156 (visited on 11/13/2018).

[5] Alessandra Canazza et al. „Experimental models of brain ischemia: a review of techniques, magnetic resonance imaging, and investigational cell-based therapies". In: *Frontiers in neurology* 5 (2014), p. 19.

DOI: 10.3389/fneur.2014.00019.

[6] Naoyo Nishida et al. „Angiogenesis in cancer". In: *Vascular health and risk management* 2.3 (2006), p. 213.

DOI: 10.2147/vhrm.2006.2.3.213.

[7] Berislav V. Zlokovic. „Neurovascular pathways to neurodegeneration in Alzheimer's disease and other disorders". In: *Nature Reviews Neuroscience* 12.12 (2011), pp. 723–

738.

DOI: 10.1038/nrn3114.

[8]   Alexei A. Bogdanov Jr et al. „Protected graft copolymer (PGC) in imaging and therapy: a platform for the delivery of covalently and non-covalently bound drugs". In: *Theranostics* 2.6 (2012), p. 553.

DOI: 10.7150/thno.4070.

[9]   Gary D. Hutchins et al. „Small animal PET imaging". In: *ILAR journal* 49.1 (2008), pp. 54–65.

DOI: 10.1093/ilar.49.1.54.

[10]   Steven R. Meikle et al. „Small animal SPECT and its place in the matrix of molecular imaging technologies". In: *Physics in medicine and biology* 50.22 (2005), R45.

DOI: 10.1088/0031-9155/50/22/r01.

[11]   Nikos K. Logothetis. „What we can do and what we cannot do with fMRI". In: *Nature* 453.7197 (2008), pp. 869–878.

DOI: 10.1038/nature06976.

[12]   Rakesh K. Jain, Lance L. Munn, and Dai Fukumura. „Dissecting tumour pathophysiology using intravital microscopy". In: *Nature Reviews Cancer* 2.4 (2002), pp. 266–276.

DOI: 10.1038/nrc778.

[13]   U. Baran and R. K. Wang. „Review of optical coherence tomography based angiography in neuroscience". In: *Neurophotonics* 3.1 (2016), p. 010902.

DOI: 10.1117/1.NPh.3.1.010902.

[14]   Emilie Macé et al. „Functional ultrasound imaging of the brain". In: *Nature methods* 8.8 (2011), pp. 662–664.

DOI: 10.1038/nmeth.1641.

[15]   Paul Beard. „Biomedical photoacoustic imaging". In: *Interface focus* (2011).

DOI: 10.1098/rsfs.2011.0028.

[16] Adrian Taruttis and Vasilis Ntziachristos. „Advances in real-time multispectral optoa-coustic imaging and its applications". In: *Nature Photonics* 9.4 (2015), pp. 219–227.
DOI: `10.1038/nphoton.2015.29`.

[17] X. Luís Deán-Ben et al. „Functional optoacoustic neuro-tomography for scalable whole-brain monitoring of calcium indicators". In: *Light: Science & Applications* 5.12 (2016), e16201.
DOI: `10.1038/lsa.2016.201`.

[18] Xosé Luís Deán-Ben and Daniel Razansky. „Adding fifth dimension to optoacoustic imaging: volumetric time-resolved spectrally enriched tomography". In: *Light: Science & Applications* 3.1 (2014).
DOI: `10.1038/lsa.2014.18`.

[19] Depeng Wang, Yun Wu, and Jun Xia. „Review on photoacoustic imaging of the brain using nanoprobes". In: *Neurophotonics* 3.1 (2016), pp. 010901–010901.
DOI: `10.1117/1.nph.3.1.010901`.

[20] H. F. Zhang et al. „Imaging of hemoglobin oxygen saturation variations in single vessels in vivo using photoacoustic microscopy". In: *Applied Physics Letters* 90.5 (2007), p. 53901.
DOI: `Artn05390110.1063/1.2435697`.

[21] Bo Ning et al. „Simultaneous photoacoustic microscopy of microvascular anatomy, oxygen saturation, and blood flow". In: *Optics letters* 40.6 (2015), pp. 910–913.
DOI: `10.1364/ol.40.000910`.

[22] L. Wang et al. „Fast voice-coil scanning optical-resolution photoacoustic microscopy". In: *Optics Letters* 36.2 (2011), pp. 139–41.
DOI: `10.1364/OL.36.000139`.

[23] J. Yao et al. „High-speed label-free functional photoacoustic microscopy of mouse brain in action". In: *Nature Methods* 12.5 (2015), pp. 407–10.
DOI: `10.1038/nmeth.3336`.

[24] Laser Institute of America. *ANSI Z136.1 - Safe Use of Lasers*. Report. 2014.

[25] Jin Young Kim et al. „High-speed and high-SNR photoacoustic microscopy based on a galvanometer mirror in non-conducting liquid". In: *Scientific reports* 6 (2016), p. 34803.

DOI: 10.1038/srep34803.

[26] Sven Gottschalk et al. „Noninvasive real-time visualization of multiple cerebral hemo-dynamic parameters in whole mouse brains using five-dimensional optoacoustic to-mography". In: *Journal of Cerebral Blood Flow & Metabolism* 35.4 (2015), pp. 531–535.

DOI: 10.1038/jcbfm.2014.249.

[27] **Johannes Rebling** et al. „A new catheter design for combined radiofrequency ablation and optoacoustic treatment monitoring using copper-coated light-guides". In: *Optical Fibers and Sensors for Medical Diagnostics and Treatment Applications XVIII*. Ed. by Israel Gannot. Vol. 10488. International Society for Optics and Photonics. SPIE, Feb. 2018, p. 1048805.

DOI: 10.1117/12.2287390.

[28] Sava Sakadzic et al. „Two-photon high-resolution measurement of partial pressure of oxygen in cerebral vasculature and tissue". In: *Nature methods* 7.9 (2010), p. 755.

DOI: 10.1038/nmeth.1490.

[29] Héctor Estrada et al. „Virtual craniotomy for high-resolution optoacoustic brain microscopy". In: *Scientific reports* 8.1 (Jan. 2018), p. 1459.

DOI: 10.1038/s41598-017-18857-y.

[30] Rebecca L. Lowery and Ania K. Majewska. „Intracranial injection of adeno-associated viral vectors". In: *Journal of visualized experiments: JoVE* 45 (2010).

DOI: 10.3791/2140.

[31] Yizhi Liang et al. „2 MHz multi-wavelength pulsed laser for functional photoacoustic microscopy". In: *Optics letters* 42.7 (2017), pp. 1452–1455.

DOI: 10.1364/ol.42.001452.

[32] Parsin Hajireza, Alexander Forbrich, and Roger Zemp. „In-vivo functional optical-resolution photoacoustic microscopy with stimulated Raman scattering fiber-laser source". In: *Biomedical optics express* 5.2 (2014), pp. 539–546. DOI: 10.1364/boe.5.000539.

A.

A.1. Publisher Letters of Approval

The following pages contain letters of approval from the publishers for the manuscripts reprinted and used throughout this thesis, as required for a publication-based dissertation by the "Regulations for the Award of Doctoral Degrees at the Technische Universität München". The approvals are reprints of the original electronic correspondance as recieved from the publishers.

Nicole Harris to me   Jul 5

Dear Mr. Rebling,

Thank you for seeking permission from SPIE to reprint material from our publications. As author, SPIE shares the copyright with you, so you retain the right to reproduce your paper in part or in whole.

    Publisher's permission is hereby granted under the following conditions:

      (1) the material to be used has appeared in our publication without credit or acknowledgment to another source; and

      (2) you credit the original SPIE publication. Include the authors' names, title of paper, volume title, SPIE volume number, and year of publication in your credit statement.

Sincerely,

Nicole Harris
Administrative Editor, SPIE Publications
1000 20th St.
Bellingham, WA 98225
+1 360 685 5586 (office)
nicoleh@spie.org

SPIE is the international society for optics and photonics. http://SPIE.org

SPIE.

From: Johannes Rebling <johannesrebling@gmail.com>
Sent: Wednesday, July 4, 2018 7:22 AM
To: reprint_permission <reprint_permission@spie.org>
Subject: Use of article in PhD Thesis

…

Rights DE to me   Jul 12

Dear Johannes Rebling,

We hereby grant permission for the requested use expected that due credit is given to the original source.

If material appears within our work with credit to another source, authorisation from that source must be obtained.

Credit must include the following components:

- Journals: Author(s) Name(s): Title of the Article. Name of the Journal. Publication year. Volume. Page(s). Copyright Wiley-VCH Verlag GmbH & Co. KGaA. Reproduced with permission.

If you also wish to publish your thesis in electronic format, you may use the article according to the Copyright transfer agreement:

<u>3. Final Published Version</u>.
Wiley-VCH hereby licenses back to the Contributor the following rights with respect to the final published version of the Contribution:
a. […]
b. Re-use in other publications. The right to re-use the final Contribution or parts thereof for any publication authored or edited by the Contributor (excluding journal articles) where such re-used material constitutes less
than half of the total material in such publication. In such case, any modifications should be accurately noted.

Kind regards

Bettina Loycke
Senior Rights Manager
Rights & Licenses

Wiley-VCH Verlag GmbH & Co. KGaA
Boschstraße 12
69469 Weinheim
Germany
www.wiley-vch.de

T   +(49) 6201 606-280
F   +(49) 6201 606-332
rightsDE@wiley.com

WILEY

Von: Wiley Global Permissions
Gesendet: Donnerstag, 12. Juli 2018 4:37
An: Rights DE <RIGHTS-and-LICENCES@wiley-vch.de>
Betreff: FW: NON RIGHTSLINK - Use of article in PhD Thesis

From: Johannes Rebling [mailto:johannesrebling@gmail.com]
Sent: 04 July 2018 16:44
To: Wiley Global Permissions <permissions@wiley.com>
Subject: NON RIGHTSLINK - Use of article in PhD Thesis
…

Use of article in PhD Thesis

Dear Johannes Rebling,

Thank you for contacting The Optical Society.

For the use of material from Johannes Rebling, Francisco Javier Oyaga Landa, Xosé Luís Deán-Ben, Alexandre Douplik, and Daniel Razansky, "Integrated catheter for simultaneous radio frequency ablation and optoacoustic monitoring of lesion progression," Opt. Lett. 43, 1886-1889 (2018):

As long as the copyrighted material is included within the body, section or chapter, of the thesis, and is not posted separate from the thesis, OSA considers your requested use of its copyrighted materials to be permissible within the author rights granted in the Copyright Transfer Agreement submitted by the requester on acceptance for publication of his/her manuscript. If the entire article is being included, it is requested that the **Author Accepted Manuscript** (or preprint) version be the version included within the thesis and that a complete citation of the original material be included in any publication. This permission assumes that the material was not reproduced from another source when published in the original publication.

The **Author Accepted Manuscript** version is the preprint version of the article that was accepted for publication but not yet prepared and/or formatted by The Optical Society or its vendors.

While your publisher should be able to provide additional guidance, OSA prefers the below citation formats:

      For citations in figure captions:

      [Reprinted/Adapted] with permission from ref [x], [Publisher]. (with full citation in reference list)

      For images without captions:

      Journal Vol. #, first page (year published) An example: Opt. Lett. 43, 1886 (2018)

Please let me know if you have any questions.

Kind Regards,

Rebecca Robinson

Rebecca Robinson
July 13, 2018
Authorized Agent, The Optical Society

From: Johannes Rebling <johannesrebling@gmail.com>
Sent: Thursday, July 5, 2018 9:28 AM
To: pubscopyright <copyright@osa.org>
Subject: Use of article in PhD Thesis
…